

**FROM PROXIMAL TO REMOTE  
SENSING: ANALYSING THE  
PYROPHYLLITE-MUSCOVITE  
ASSOCIATION IN THE BUCKSKIN  
RANGE, YERINGTON DISTRICT,  
NEVADA.**

BRUNO VIRGILIO PORTELA

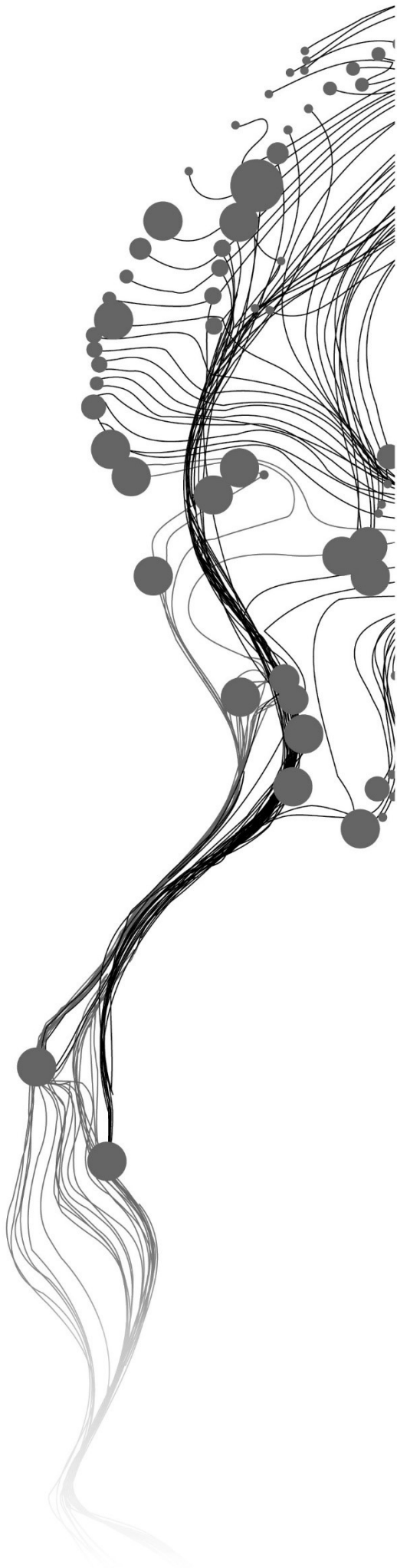
June 2020

SUPERVISORS:

Dr. F.J.A. van Ruitenbeek

Dr. C.A. Hecker





# **FROM PROXIMAL TO REMOTE SENSING: ANALYSING THE PYROPHYLLITE-MUSCOVITE ASSOCIATION IN THE BUCKSKIN RANGE, YERINGTON DISTRICT, NEVADA.**

BRUNO VIRGILIO PORTELA

Enschede, The Netherlands, June 2020

Thesis submitted to the Faculty of Geo-Information Science and Earth Observation of the University of Twente in partial fulfilment of the requirements for the degree of Master of Science in Geo-information Science and Earth Observation.

Specialization: Applied Remote Sensing for Earth Sciences

## **SUPERVISORS:**

Dr. F.J.A. van Ruitenbeek

Dr. C.A. Hecker

## **THESIS ASSESSMENT BOARD:**

Prof. dr. M. van der Meijde (Chair)

Dr. M.W.N. Buxton (External Examiner, Technical University of Delft)

#### DISCLAIMER

This document describes work undertaken as part of a programme of study at the Faculty of Geo-Information Science and Earth Observation of the University of Twente. All views and opinions expressed therein remain the sole responsibility of the author, and do not necessarily represent those of the Faculty.

# ABSTRACT

Hydrothermal mineral deposits such as skarns, porphyry, epithermal and SEDEX systems, are the primary source of mineral commodities of global importance, such as copper, gold, and silver. Due to their importance, these types of mineral deposits have been subject to numerous studies over the years, using different approaches, including hyperspectral proximal (laboratory-based) and remote (airborne) sensing. Since hydrothermal alteration minerals are active in, amongst others, the visible and infrared range, the analysis of spectral absorption features can be used to identify the mineralogy associated with different alteration events. Some events are responsible for the occurrence of mineral commodities, while other events create mineral alteration without any economic concentrations of precious elements. Therefore, it is important to develop a mineral exploration strategy to rapidly identify and map the indicator minerals linked to a mineralising event.

This research combined short-wave infrared proximal (laboratory) and remote (airborne) sensing imagery to study how to discriminate intimate intergrowths of pyrophyllite and muscovite that are linked to different alteration events in epithermal gold systems. The main objective of this study was to characterise the occurrence of overprinting patterns for pyrophyllite and muscovite by combining wavelength maps and spectral indices to highlight these alteration patterns at the laboratory (SisuCHEMA hyperspectral imager) as well as at the airborne (ProSpecTIR-VS sensor) scale. For this study, the test area selected was the Buckskin range at the Yerington district, Nevada (USA), a high-sulfidation epithermal system.

Wavelength maps in different ranges were used to map the hydrothermal alteration mineralogy at both scales. The results of the airborne data showed outward zoning alteration patterns from an inner zone of alunite  $\pm$  pyrophyllite towards the surrounding area dominated by muscovite of varied wavelength position of its Al-OH absorption feature. The laboratory data improved the characterisation of the hydrothermal alteration mineralogy, which included alunite, pyrophyllite, muscovite, dickite, kaolinite, chlorite, topaz and zunyite. The spatial distribution of the pyrophyllite-muscovite association and, consequently, the textural relationship of the two minerals was addressed through the development of a novel spectral index. Pervasive and veinlet-controlled textures were characterised and a subtle shift in the wavelength position of the Al-OH absorption feature of muscovite from 2189 to 2195 nm was detected. Although the shift was not a direct indication of overprinting, an intergrowth of pyrophyllite and muscovite sheets was suggested. The temporal relationship of the two minerals was then addressed: first through the interpretation of the alteration texture; second, through the backscattered electron images (BSE) and microprobe analysis data (EMPA), confirming the overprint of muscovite over pyrophyllite.

The association of the spatial distribution with the textural relationship of the pyrophyllite-muscovite association allowed the reconstruction of the fluid chemistry and fluid pathway linked to this scenario. An early-stage low pH high-temperature magmatic-hydrothermally derived fluid characterised by the presence of alunite  $\pm$  pyrophyllite, responsible for an intense acid leaching and, consequently, the generation of permeable zones in the lithocap. These permeable zones worked as channels (feeders) for the emplacement of a late-stage fluid of near-neutral pH and lower salinity, characterised by the occurrence of muscovite  $\pm$  zunyite. Thus, the characterisation of the pyrophyllite-muscovite association suggested a high sulfidation epithermal context for the Buckskin range, following the current understanding of this system.

While no economic Au deposits are known from this part of the Buckskin range, this research clearly demonstrates the importance of characterising and mapping overprinting patterns at different scales to assist the reconstruction of fluid composition and fluid emplacement. Therefore, contributing to an improved understanding of a high sulfidation epithermal system and a better definition of target areas for follow-up mineral exploration studies.

# ACKNOWLEDGEMENTS

I want to thank my family! My father, Paulo, my mother, Rosana and, my sister, Ananda. I would not be able to be here today without your love, support, and friendship. Thank you very much for always been there for me through all the ups and downs that were part of this past 30 years. No matter when, where or how. There are not enough words, either in English or Portuguese, to express my gratitude to you.

I want to thank my girlfriend, Camila! More than my girlfriend, thank you for being my best friend, my partner, my companion! I cannot thank you enough for how patient, comprehensive, lovely, caring, and thoughtful you were during these past 2 years! Life has been a fantastic journey by your side so far, and it is only the beginning. Thank you so much!

I want to thank my aunt, Dade, for always been there for me with a comforting and incisive word. You had and still have an amazing role in all that is happening to me! I want to thank the rest of my family for being very supportive and thoughtful, even when I was so far from home.

A special thanks to my supervisors, Dr Frank van Ruitenbeek and Dr Chris Hecker, for all the support and attention during this period. It was an amazing opportunity to be supervised by you, and I am incredibly grateful for all the conversations and teaching moments that I had in this past year. Thank you very much!

I want to thank ITC and the staff of the ESA department. Dr Harald van der Werff, Bart Krol, Dr Rob Hewson, Wim Bakker, Dr Islam Fadel and Prof. dr. Mark van der Meijde, thank you very much for your insights and support during the period.

I want to thank Michael Sepp and Prof. John Dilles from Oregon State University who collaborated with this research. A special thanks to Michael for all his help throughout this period with his analysis and insights. Thank you for all the conversations we had in this past year. They were crucial for me to accomplish this master's degree.

I also want to thank Dr. Dean Riley, Dr. Conrad Wright, and Dr. William Peppin from The Aerospace Corporation and SpecTIR LLC for providing the airborne ProSpecTIR data set used in this research.

I want to thank all my friends that were also part of this journey. From the new friends that I had the pleasure to make here in The Netherlands to my old friends back in Brazil and Chile! Thank you very much, Camila, Carol, Lucas, Rachael, Laura, Martjin, Kirsten, Philip, Lorraine, Cassiano and all the colleagues from ITC for all the laughs and good times that we had this past 2 years. Also, thank you very much to all my friends back home Alexis, Adam, Gabriel (Mussum), Vitão, Daniel, Lu, Dine, Victor (2/hora), Pablo, Raphael (Catatau) and the Santandrea family!

*“...e sonhos não envelhecem...”  
(and dreams do not age)*

# TABLE OF CONTENTS

Abstract.....	i
Acknowledgements .....	ii
Table of contents .....	iii
List of figures .....	iv
List of tables .....	vi
1. INTRODUCTION.....	7
1.1. Background.....	7
1.2. Problem statement .....	10
1.3. Research objectives .....	11
1.4. Research questions .....	11
1.5. Thesis structure.....	12
2. GEOLOGIC SETTING OF THE STUDY AREA .....	13
3. DATA SETS .....	15
3.1. ProSpecTIR data (Hyperspectral airborne data).....	15
3.2. Specim data (Hyperspectral laboratory data).....	15
3.3. Petrographic, chemical and mineralogical data .....	15
4. METHODOLOGY.....	16
4.1. Introduction .....	16
4.2. Data pre-processing .....	17
4.3. Minimum Wavelength Mapper .....	18
4.4. Spectral index .....	21
5. RESULTS AND DISCUSSIONS .....	24
5.1. ProSpecTIR wavelength maps .....	24
5.2. Specim wavelength maps .....	27
5.3. Spectral index .....	35
6. BUCKSKIN RANGE, AN EPITHERMAL SYSTEM.....	43
6.1. Introduction .....	43
6.2. Hydrothermal alteration mineralogy (alteration zones).....	44
6.3. Pyrophyllite-Muscovite distribution.....	45
6.4. Overprinting at the laboratory scale.....	46
6.5. Overprinting at the airborne scale.....	51
7. CONCLUSIONS AND RECOMMENDATIONS.....	54
7.1. Conclusions .....	54
7.2. Recommendations.....	55
List of references .....	57
Appendix.....	61

# LIST OF FIGURES

## Chapter 1

*Figure 1.1:* Hydrothermal system explained through fluid flow regime. (modified after Pirajno (2009)). ..... 7

*Figure 1.2:* Example of mineral deposits related to hydrothermal alteration (Sillitoe (2010))..... 8

## Chapter 2

*Figure 2.1:* Middle: Location of the study area (red box) at the northwest area of Nevada, USA (Adapted from Hecker et al. (2019b); Proffett & Dilles (1984) and Base map from Esri (2019)) ..... 14

*Figure 2.2:* Geological (a) and alteration map (b) of the central study area (both simplified after Lipske (2002)). ..... 14

## Chapter 4

*Figure 4.1:* Spectral profile of mineral groups which are active in the 2100-2400 nm range. Convex hull removal applied on spectra from the USGS Spectral Library (Pontual et al., 1997; Kokaly et al., 2017) ..... 16

*Figure 4.2:* Representation of a sample mosaicking process with the display of the strips of a sample..... 18

*Figure 4.3:* Determination of the interpolated wavelength position of the deepest absorption feature through parabolic interpolation (van Ruitenbeek et al., 2014)..... 19

*Figure 4.4:* Example of the legend of a wavelength map from a wide (A) and a narrow (B) interval showing the distinction achieved with the narrow range..... 20

*Figure 4.5:* Spectral curve with the parameters used for the airborne ProSpecTIR index..... 21

*Figure 4.6:* Spectral curve with the parameters used for the laboratory Specim spectral index..... 22

*Figure 4.7:* Spectral profile of the linear mixtures developed for both data sets..... 23

*Figure 4.8:* Spectral index defined to illustrate the shift in the wavelength position of the Al-OH absorption feature of muscovite in the laboratory Specim data ..... 23

## Chapter 5

*Figure 5.1:* Wavelength maps of the airborne ProSpecTIR data of the study area (red polygon)..... 24

*Figure 5.2:* Spectral curve (b) observed in the central region of the study area..... 25

*Figure 5.3:* Indication of the areas in the central region of the study area that did and did not present an absorption feature at 1760 nm ..... 26

*Figure 5.4:* Identification of three different types of contact zones observed in the central region of the study area between muscovite-rich and alunite  $\pm$  pyrophyllite-rich areas..... 27

*Figure 5.5:* Comparison of wavelength maps produced by using the automatic depth stretch (a) and customised depth stretch (b) in the Minimum Wavelength Mapper tool..... 27

*Figure 5.6:* Wavelength maps of the sample R875389 with a predominance of muscovite ..... 28

*Figure 5.7:* Wavelength maps of the sample R875431 with pyrophyllite..... 28

*Figure 5.8:* Wavelength maps of the sample R875382 with pyrophyllite..... 29

*Figure 5.9:* Wavelength maps of the sample 664b with alunite..... 29

*Figure 5.10:* Spectral profile with the spectra of the mineralogy overview ..... 30

*Figure 5.11:* Spectral profile of different regions of the sample R875327 to illustrate the variations in the Al-OH absorption feature..... 31

*Figure 5.12:* Spectral profile of different regions of the sample R875367 to illustrate the variations in the Al-OH absorption feature..... 32

*Figure 5.13:* Spectral profile of different regions of the sample R875478 to illustrate the variations in the Al-OH absorption feature..... 33

<i>Figure 5.14:</i> Spectral profile of different regions of the sample R875524 to illustrate the variations in the Al-OH absorption feature.....	33
<i>Figure 5.15:</i> Hydrothermal alteration mineralogy distribution over the 2150-2250 nm wavelength map of the study area.....	35
<i>Figure 5.16:</i> Spectral index image (a) and the classified image (b) of the central region of the study area obtained with the decision tree method.....	36
<i>Figure 5.17:</i> Classified image of the spectral index focused on the central region of the study area .....	36
<i>Figure 5.18:</i> Identification of the contact zones defined with the 2150-2250 nm wavelength map (a) in the classified image of the spectral index (b). .....	37
<i>Figure 5.19:</i> Classified images of the spectral indices to characterise the mineralogy overview and how it was represented in this method.....	39
<i>Figure 5.20:</i> Comparison of the results obtained through both spectral indices for the sample R875327 ...	40
<i>Figure 5.21:</i> Comparison of the results obtained through both spectral indices for the sample R875367 ...	40
<i>Figure 5.22:</i> Comparison of the results obtained through both spectral indices for the sample R875478 ...	41
<i>Figure 5.23:</i> Comparison of the results obtained through both spectral indices for the sample R875524. ..	41
<i>Figure 5.24:</i> Example of the overestimation of muscovite-rich zones in a classified image of the spectral index (1) in a sample with a shallow absorption feature at 2066-2078 nm. ....	42

## Chapter 6

<i>Figure 6.1:</i> Comparison of the hydrothermal alteration assemblage identified from the laboratory Specim data set with the simplified alteration map developed by Lipske (2002).....	44
<i>Figure 6.2:</i> Comparison of the alteration zoning pattern identified by this research with alteration assemblage map developed by Fagbohun (2015).....	45
<i>Figure 6.3:</i> Representation of an unaltered rock (a), pervasively altered rock (b) and, a vein-type altered rock (Meller & Kohl, 2014).....	46
<i>Figure 6.4:</i> 2150-2250 nm wavelength maps (0-50% depth stretch) and classified images of the spectral index (2) of four samples with pyrophyllite and muscovite co-occurrence. ....	47
<i>Figure 6.5:</i> 2150-2250 nm wavelength map (a), classified image of the spectral index (2) (b) and a schematic representation of veinlet-controlled and pervasive alteration of this sample .....	47
<i>Figure 6.6:</i> Representation of the shift of the wavelength position of the Al-OH absorption feature of muscovite in boundaries between pyrophyllite-rich and muscovite-rich zones.....	48
<i>Figure 6.7:</i> Spectral profile to indicate the shift of the wavelength position of the Al-OH absorption feature of muscovite through different zones of a sample. ....	49
<i>Figure 6.8:</i> Backscattered electron images indicating the intergrowth of pyrophyllite and muscovite sheets in samples with the shift of the wavelength position of the Al-OH absorption feature of muscovite.....	50
<i>Figure 6.9:</i> Microprobe analysis graphic corroborating the intergrowth of muscovite and pyrophyllite not visible in the backscattered image scale .....	51
<i>Figure 6.10:</i> Combination of the 2150-2250 nm wavelength map, the contact zones defined in section 5.1 and the samples with overprinting patterns .....	52

# LIST OF TABLES

*Table 4.1:* Primary wavelength ranges indicate the wavelength maps created for both data sets. Additional wavelength ranges indicate the narrower wavelength ranges used only for the Specim data .....20

# 1. INTRODUCTION

## 1.1. Background

Hydrothermal systems can be defined as a complex arrangement between a heat source and a fluid phase. These two components are related to a plumbing structure which will lead the resulting solutions to a depositional environment (Pirajno, 2009). To this equation, it is crucial to define and characterise the geological context where this process occurs, because it will give an indication of the interaction of the fluid phase and the wall rock. As discussed by Pirajno (2009), a hydrothermal system could also be explained through an analogy with a fluid flow regime, where a large-volume reservoir is the source of fluids that will be transported through high permeability pathways until it reaches an impermeable barrier, also defined as the depositional site (Fig. 1.1). This last stage of the process is essential because it is when and where mineral deposits associated with the hydrothermal process are formed.

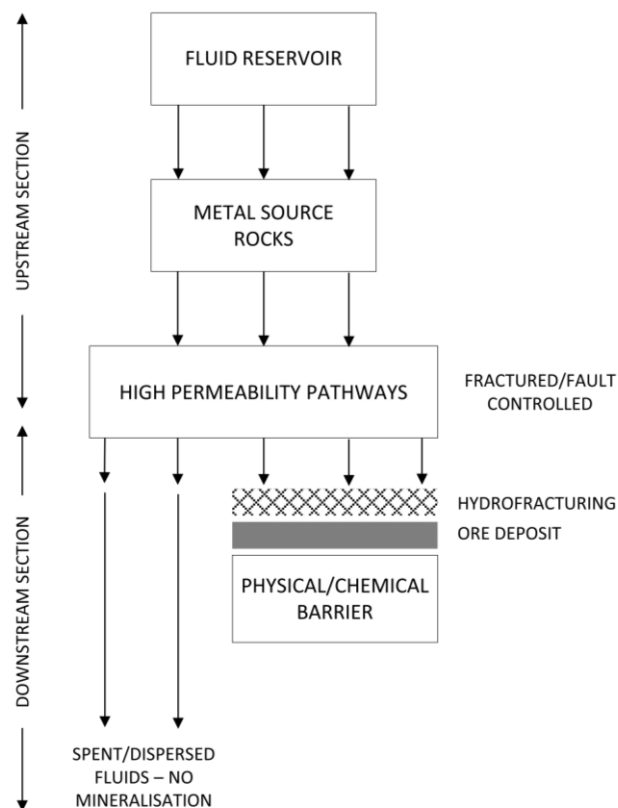


Figure 1.1: Hydrothermal system explained through fluid flow regime (modified after Pirajno (2009)).

In other words, hydrothermal mineral deposits are the result of the circulation of hot fluids which will interact with wall rock depending on physicochemical conditions of the environment. This interaction, also named hydrothermal alteration, is a process which leads to mineralogical, chemical, and textural changes of the wall rock. Thus, the parameters which control the alteration process are based on the characteristics of the wall rock and the composition of the fluids (e.g. concentration of  $H^+$ ) (Pirajno, 2009). According to these criteria, hydrothermal alteration can be classified in alkali metasomatism and potassium silicate alteration, propylitic, phyllic or sericitic, intermediate argillic and advanced argillic alteration.

Thus, the type of hydrothermal alteration, the characteristics of the wall rock and geologic context (tectonic setting), all play a crucial role on the types of different hydrothermal mineral deposits, such as

porphyry systems, epithermal systems (High and Low-sulfidation), skarns, SEDEX (sedimentary-exhalative deposits) systems, to name a few examples (McQueen, 2005; Pirajno, 2009) (Fig. 1.2). These types of mineral deposits are critical because most of them are related to commodities used worldwide, such as copper, gold, and silver. Due to its importance, these types of mineral deposits have been subject to different studies throughout the years, using several approaches, including hyperspectral proximal (laboratory-based) and remote (airborne) sensing.

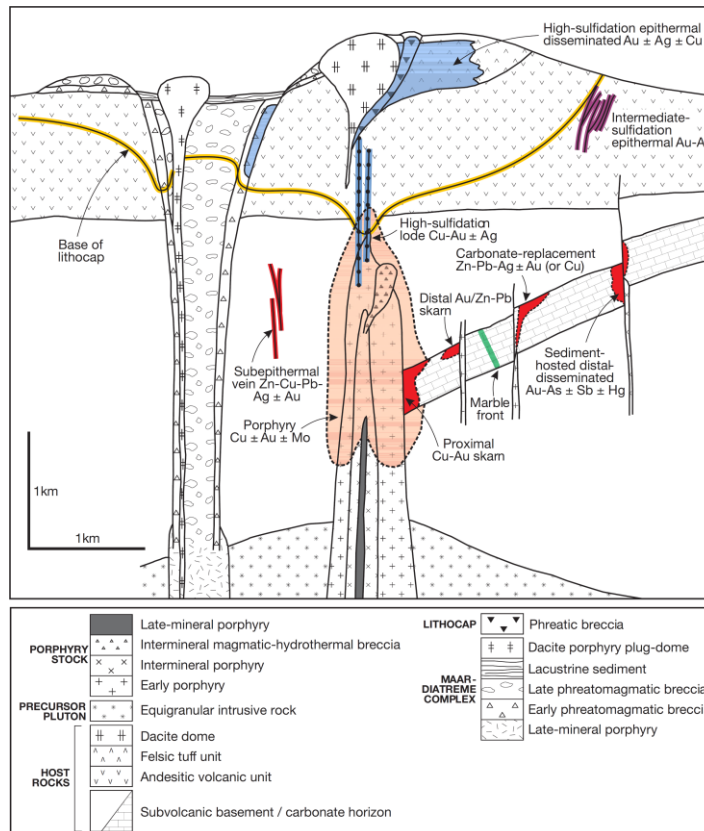


Figure 1.2: Example of mineral deposits related to hydrothermal alteration (Sillitoe (2010)).

As discussed by van der Meer et al. (2012), the primary purpose of hyperspectral remote sensing in geologic studies is to characterise and map the Earth surface composition for mineral exploration. This is done through the analysis of spectral absorption features in many narrow and contiguous bands. The study of hydrothermal systems supported by hyperspectral airborne data is well established and consolidated, owing to abundant mineral groups present in this system which are active in the visible and near-infrared range, such as hydroxyl-bearing minerals, ammonium-bearing minerals, phyllosilicates, iron oxides, and carbonates (van der Meer et al., 2012).

At the Yerington district, Nevada (USA), Cudahy et al. (2001) mapped the porphyry-skarn alteration by identifying the occurrence of alteration minerals (porphyry: epidote, plagioclase feldspar, and white mica; skarn: dolomite, garnet, and pyroxene) using HyMap and SEBASS data. Also, at Yerington, Fagbohun (2015) combined dominant spectral features in ProSpecTIR and SEBASS data for mineralogical mapping. Bedini, van der Meer, & van Ruitenbeek (2009) using HyMap data, were able to map the spatial distribution of clays and alunite associated with an epithermal deposit in the Rodalquilar caldera, Spain. The authors discussed that with the information added through the spectral study in the area, maps of hydrothermal alteration zones could be refined to better represent its distribution. At the well-known location for remote sensing studies of Cuprite, Nevada (USA), Swayze et al. (2014) used mineral maps obtained through AVIRIS data to study the advanced argillic alteration occurrence and improve the current knowledge of the area by integrating this technique with traditional exploration methods. In this

work, the authors were able to identify chemical variations (e.g. white mica and alunite) and spatial distribution of minerals. This led to a deeper understanding of the condition of the fluids during the alteration process, and the correct emplacement and mapping of the advanced argillic alteration in the geologic context of the area. One clear example that is discussed is the lack of pyrophyllite in the area which is, along with other aspects, a clear indicator of a low-sulfidation epithermal system. Even though the previous examples have shown that airborne data are an important tool to address surface mineralogy mapping, one relevant aspect that must be taken into account is the scale issue associated with it, such as the mixture of minerals per pixel (van der Meer, 2018).

To address the scale limitations of hyperspectral airborne data, the use of laboratory-based (proximal) hyperspectral images has recently become more common and necessary. As discussed by van der Meer (2018), the possibility of studying rock samples, thin sections and drill cores at different spatial resolutions, increases the chance of analysing pixels containing only one mineral, and not a mixture. Using a hyperspectral camera (HySpex) with a spatial resolution of 1 mm square pixel, Baissa et al. (2011) mapped minerals in hand specimens of carbonate rocks from Morocco, confirming and improving the level of detail of results obtained with airborne hyperspectral data. By combining index calculation (to the study of main absorption bands of carbonates) and spectral angle mapper classification method (overall shape of reflectance spectra and map accessory mineralogy), Baissa et al. (2011) were able to add information regarding degrees of diagenesis to the mineralogical maps.

Applying proximal sensing to carbonate rocks hand specimens, Zaini et al. (2014) used SisuCHEMA hyperspectral setup to identify and estimate the mineral abundance by comparing different methods of spectral classification such as wavelength position analysis, spectral angle mapper (SAM) and linear spectral unmixing (LSU). Regarding drill cores, in Saskatchewan, Canada, Mathieu et al. (2017), concluded that laboratory-based hyperspectral images address the problem of mixed pixels as compared to field spectrometers. Along the same line, one of the outcomes in Dalm et al. (2017) was that, when comparing short-wave infrared hyperspectral imaging versus point spectrometry, the former has the advantage of providing information on the sample's texture. van Ruitenbeek et al. (2019) used the SisuCHEMA hyperspectral setup to identify and measure microstructures and microstructural elements in mineral maps. As discussed by the authors, linking mineralogical composition and microstructure information obtained through laboratory-based hyperspectral images could lead to a better understanding of rock-forming processes.

Infrared spectrometry can detect alteration minerals of different mineralogy and mineral chemistry as a proxy for fluid chemistry. Brown et al. (2006) combined HyMap and portable infrared mineral analyser (PIMA) data to identify and map hydrothermal alterations minerals in the Panorama Formation, Western Australia. By mapping the occurrence of white micas, its chemical variations (Muscovite: Al-rich or Al-poor) and the occurrence of pyrophyllite, the authors were able to infer the pH conditions of the hydrothermal system. According to the study, a more alkaline state would lead to a predominance of muscovite over pyrophyllite. Meanwhile, a lower pH would favour the predominance of pyrophyllite over muscovite. In their study, the authors concluded that there is a pattern of muscovite being replaced by pyrophyllite.

The concept mentioned in the previous paragraphs was essential for the development of this study. This research investigates the occurrence and textural relation of the pyrophyllite and muscovite (white mica) association in the Buckskin range, Yerington District, Nevada, USA. But, the existence of the replacement or overprint texture of muscovite and pyrophyllite has been documented in several mineral districts throughout the world.

At the El Salvador deposit, Chile, Gustafson & Hunt (1975), mentioned that the replacement of muscovite by pyrophyllite was not conclusive as a recurrent pattern in the deposit, but the substitution of

these minerals was noted at depth. In a different study at the El Salvador deposit, based on petrography, X-ray diffraction (XRD) and back-scattered electron images (BSE-SEM), Watanabe & Hedenquist (2001) concluded that pyrophyllite frequently substitutes muscovite along cleavages and in independent crystals. Pyrophyllite overprints muscovite-dominant assemblages as part of a very late-stage advanced argillic assemblage with alunite dominance. According to the authors, the pyrophyllite occurrence is largely controlled by topography, with pyrophyllite occurring at higher elevations.

At the Oyu Tolgoi district, Mongolia, Khashgerel et al. (2009), using electron microprobe analysis (EMPA) and SWIR spectrometry on thin section, described that early muscovite-bearing assemblages are replaced by pyrophyllite-dominant advanced argillic alteration both in the host rock and in the intrusion. Besides, small zones of muscovite following the pyrophyllite-dominant alteration were found as isolated occurrences. The authors also mentioned that there is an increment of pyrophyllite near to shallow regions of the advanced argillic alteration zones, similarly to what Watanabe & Hedenquist (2001) proposed for the El Salvador deposit.

Most of the districts mentioned are characterised by the replacement of muscovite by pyrophyllite except for the Buckskin range in the Yerington district. In the Buckskin range, Yerington District, Nevada (USA), Lipske & Dilles (2000) combined multispectral remote sensing (with a GEOSCAN instrument) and portable infrared mineral analyser (with a PIMA instrument) to study the advanced argillic and sericitic alteration. Lipske (2002) suggested that the advanced argillic alteration is prior to the sericitic alteration due to the replacement of pyrophyllite by sericite (muscovite) noticed in rims and cleavage planes in the area. This interpretation was verified in microprobe analysis and petrographic relations. Due to a similar grain-size and crystal habit in both minerals in rocks with advanced argillic alteration, Lipske (2002) interpreted it as the result of the replacement of pyrophyllite by muscovite.

Sepp et al. (2019) also documented the replacement of pyrophyllite by muscovite in the Buckskin range. By using optical petrography, scanning electron microscope (SEM), X-ray diffraction (XRD), quantitative evaluation of materials by scanning electron microscopy (QEMSCAN) and electron microprobe analysis (EMPA), the authors were able to identify the intergrowth of pyrophyllite and muscovite, especially at the margins of quartz-dominant feeder structures.

In these situations where one mineral replaces another at a later stage, it is essential to refer to them as a mineral association rather than a mineral assemblage. *Mineral assemblage* refers to a set of minerals which have a syngenetic formation, and its geochemical composition might be indicative of the physicochemical conditions during their formation. *Mineral association* refers to a group of minerals that occurs together but with a different temporal relation (Seedorff et al., 2005). Thus, by analysing this definition and the context regarding the mineral display in the Buckskin range, this research adopted the term *mineral association*.

## 1.2. Problem statement

Defining an epithermal system and potentially mineralised zones can be achieved by tracing different hydrothermal alteration events. These events are characterised by the fluid composition, fluid pathway and temporal relationship between them. As discussed above, previous researches addressed hydrothermal alteration events by focusing on entire mineral assemblages, instead of diagnostic minerals that are associated with different hydrothermal alteration events. Thus, to the knowledge of this research, a clear understanding on the occurrence of the pyrophyllite and muscovite (white mica) association is crucial to improve the definition of alteration zones and the current understanding of an epithermal system.

Therefore, this study has for the first time investigated, not only the surface mineralogy of the alteration zones in an epithermal system but also how these two hydrothermal alteration minerals (pyrophyllite and muscovite) are texturally related. By combining novel proximal and remote sensing data, a deeper understanding of the fluid composition (more acidic or more alkaline) was presented for the area,

indicating different timing and stages of hydrothermal events. Tracing back these different events, analysing distinct aspects, is an important tool for characterising mineralised zones in this epithermal system, but also to be replicated in other epithermal systems worldwide.

This study aimed to identify, map, and analyse the occurrence of the pyrophyllite-muscovite association (white mica) within the Buckskin range. To achieve this, hyperspectral proximal and remote sensing data were combined to address different aspects of the characterisation of this mineral occurrence. Hyperspectral airborne data (ProSpecTIR-VS sensor system) was used to map the hydrothermal alteration mineralogy of the area and understand the spatial distribution of this mineral association at an airborne scale. In order to increase the detail of information and add an essential aspect to the analysis, laboratory-based hyperspectral data (SisuCHEMA SWIR setup) was used on thin sections slabs obtained from rock specimen of the area to quantify the mineralogic association, and, most importantly, to understand the textural relationship of the mineral association. As a final step, the comparison of the spectral analysis, both in terms of mineralogical and chemical findings, was done by using scanning electron microscope (SEM) and electron microprobe analysis (EMPA) data obtained from the same rock specimens used for the laboratory-based hyperspectral images.

### **1.3. Research objectives**

#### **1.3.1. Main objective**

To characterise the occurrence of the pyrophyllite-muscovite association and its implications to the epithermal system in the Buckskin range, Yerington district by using hyperspectral proximal and remote sensing data.

#### **1.3.2. Specific objectives**

1. To identify the surface mineralogy, focusing on hydrothermal alteration minerals.
2. To determine the spatial distribution of the occurrence of the pyrophyllite-muscovite association.
3. To verify whether there is a textural relationship between pyrophyllite and muscovite.
4. To associate the textural relationship and spatial distribution to the fluid composition and pathways.
5. To link the characterisation of the pyrophyllite-muscovite association and its emplacement in the geologic context of a conceptual epithermal system.

### **1.4. Research questions**

1. To what extent is it possible to compare the surface mineralogy mapping through hyperspectral airborne data and laboratory-based hyperspectral data? Is it possible to identify the pyrophyllite-muscovite association in both scales?
2. To what extent is it possible to identify overprinting or replacement textures using laboratory-based hyperspectral data? Is there any indication of these textures on hyperspectral airborne data?
3. Does the surface mineralogy indicate the alteration zones which are already described in the literature? How does the spatial distribution of the pyrophyllite-muscovite association assist in this characterisation?
4. Is it possible to reconstruct fluid composition and fluid pathways by combining the textural and mineralogical information obtained through this hyperspectral study? Can this reconstruction indicate hydrothermal processes which occurred in this context?
5. To what extent does the characterisation of the pyrophyllite-muscovite association, compare to the current understanding of the Buckskin range as being an epithermal system?

## **1.5. Thesis structure**

### **Chapter 1: Introduction**

Discussion on the background, the problem statement, research objectives and questions.

### **Chapter 2: Geologic setting of the study area**

Detailing of the location of the study area and the current geological context.

### **Chapter 3: Data sets**

Explanation of the data sets used for this research.

### **Chapter 4: Methodology**

Discussion on the methodology applied in the different data sets.

### **Chapter 5: Results and Discussion**

Display and analysis of the results of this research.

### **Chapter 6: Buckskin range, an epithermal system**

Understanding of the findings of this research and the epithermal system context.

### **Chapter 7: Conclusions and Recommendations**

## 2. GEOLOGIC SETTING OF THE STUDY AREA

The Yerington area, located in the northwest of Nevada (USA) (Fig. 2.1), is a mining district defined by a variety of deposits such as porphyry Cu (Mo), Cu skarn, iron oxide, copper sulphide ores in metasedimentary rocks and shallow Cu-Au-Fe oxides lodes (Dilles et al., 2000). The district is composed of crystalline rocks of Mesozoic age, Cenozoic volcanic rocks (Oligocene and Miocene) and alluvial deposits (Quaternary). The Mesozoic rocks consist of late Triassic volcanic and sedimentary sequences and Middle Jurassic volcanic and plutonic rocks (Dilles & Einaudi, 1992).

This Middle Jurassic magmatism is fundamental to understand the emplacement and generation of the several mineral deposits in the district as well as the occurrence of the overprinting textures. The Artesia Lake Volcanics, a volcanic sequence, is considered the first large magmatic event which occurred during this period (Dilles et al., 2000). This sequence became the base for the emplacement of a younger intrusion, the Yerington Batholith, which, according to Dilles & Einaudi (1992) is directly responsible for all the copper deposits found in the district. In addition, as discussed by Lipske & Dilles (2000), the Artesia Lake Volcanics would be the extrusive part of the Yerington Batholith in view of the chemical, isotopic, and hydrothermal alteration evidence. The second volcanic sequence present in the district, which postdate the event of the Yerington Batholith, is the Fulstone Spring Volcanics (Dilles et al., 2000). This volcanic sequence was, subsequently, intruded by granitic dikes of a younger igneous pluton, the Shamrock Batholith.

During the Oligocene and early Miocene, volcanic rocks lay over the Mesozoic rocks present in the district, and these were topped by andesitic lavas of Miocene age. During this andesitic magmatism, east-dipping normal faults occurred in the district, becoming the precursor of a series of structural events that culminated in an active fault system of basins and ranges. This context led to a tilting process of all the pre-Miocene rocks with a tilt of 60° to 90° towards W (Dilles & Einaudi, 1992; Dilles et al., 2000; Proffett, 1977). Consequently, the rock exposure in the area represents a cross-section of this Middle Jurassic magmatism, from paleodepths of 7 km to shallow sections defined by the volcanic environments (Dilles et al., 2000) in the Buckskin range, the target area of this research (fig 2.1).

The Buckskin range, located on the west area of the Yerington District, is defined by two volcanic sequences that capped the Yerington Batholith, the previously mentioned Artesia Lake and Fulstone Spring (Lipske & Dilles, 2000; Proffett & Dilles, 1984). As discussed by Lipske & Dilles, 2000, the Buckskin range would represent an epithermal setting that also played the role of a discharge area for hydrothermal fluids.

The study area is in the Artesia Lake Volcanics, characterised by sub areal andesitic lava flows, breccias, sandstones and, ignimbrites (Fig. 2.2a). Due to an intense hydrothermal alteration process, primary textures were obliterated by advanced argillic and sericitic alteration. According to Lipske & Dilles (2000), the advanced argillic alteration is defined by three different assemblages: quartz-alunite-pyrophyllite, quartz-pyrophyllite-sericite and quartz-alunite-sericite. This last assemblage is the most common advanced argillic alteration assemblage in the Buckskin range. The sericitic alteration envelops the advanced argillic alteration and is characterised by texture-destructive sericite (muscovite)-quartz-pyrite assemblage widely distributed in the central part the Buckskin range (Lipske & Dilles, 2000) (Fig. 2.2b). The halo of the sericitic alteration surrounding the advanced argillic alteration was also identified by Fagbohun (2015) when combining airborne shortwave infrared (ProSpecTIR, 4 m spatial resolution) and longwave infrared (SEBASS) data, especially in the central part of the study area. The author characterised the advanced argillic alteration (quartz-alunite-pyrophyllite) and sericitic alteration (quartz-sericite-plagioclase) as the main hydrothermal alteration mineralogy in the area.

FROM PROXIMAL TO REMOTE SENSING: ANALYSING THE PYROPHYLLITE-MUSCOVITE ASSOCIATION IN THE BUCKSKIN RANGE, YERINGTON DISTRICT, NEVADA.

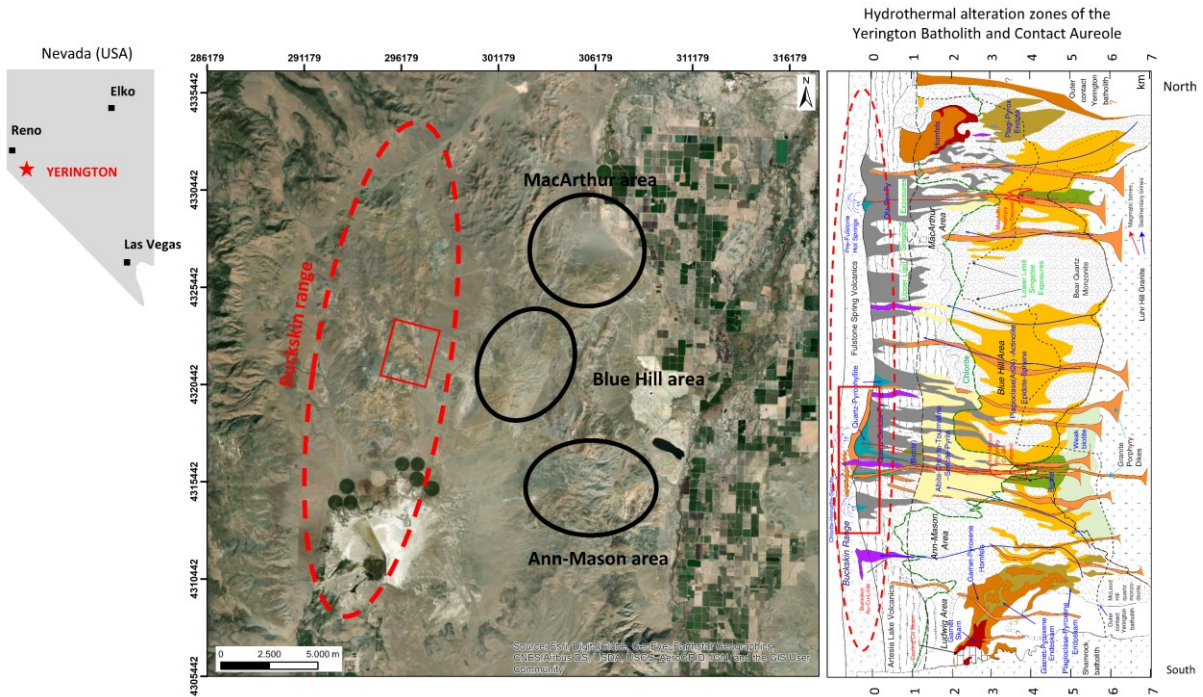


Figure 2.1: Middle: Location of the study area (red box) at the northwest area of Nevada, USA (Adapted from Hecker et al. (2019b); Proffett & Dilles (1984) and Base map from Esri (2019)). Right: The cross-section of the hydrothermal alteration zones of the Yerington batholith was rotated to align with how these zones are outcropping in the area after the tilting process (Dilles et al., 2000). Dashed red oval indicating the Buckskin range and the red box is highlighting the study area.

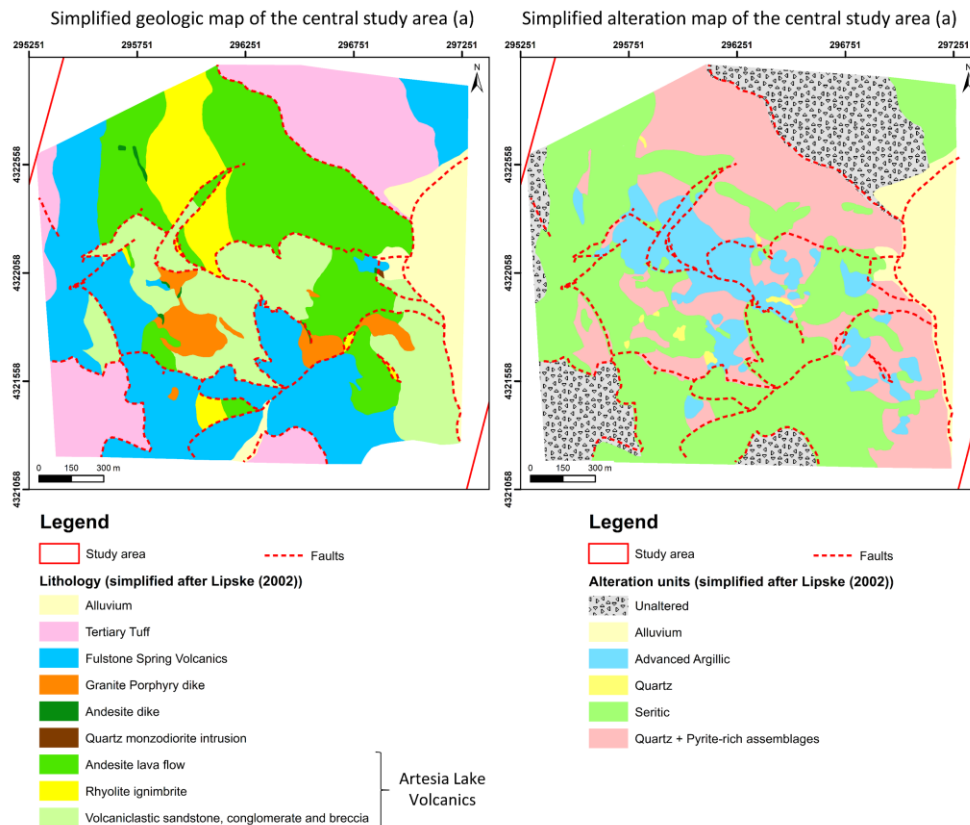


Figure 2.2: Geological (a) and alteration map (b) of the central study area (both simplified after Lipske (2002)).

### 3. DATA SETS

This study was based on the analysis of hyperspectral laboratory-based and airborne data, combined with petrographic, chemical, and mineralogical information for comparison purposes.

#### 3.1. ProSpecTIR data (Hyperspectral airborne data)

The airborne data were acquired over the Yerington district, Nevada (USA) during the Joint Airborne Collection using Hyperspectral Systems (JACHS) with the Aerospace Corporation's SEBASS instrument and SpecTIR LLC's ProSpecTIR sensor system (Hecker et al., 2019b). The ProSpecTIR sensor operates in a spectral range of 400 to 2500 nm, with a spectral resolution of 5 nm, a sampling interval of 10 nm, and 357 bands.

This data set consisted of 5 flight lines (out of the 12 flight lines covering the Buckskin range) of 1 m spatial resolution obtained with ProSpecTIR-VS sensor system. These flight lines were selected based on the area where the ground samples were collected (Appendix I) and to exclude overlapping flight lines. The data set covered an area of, approximately, 10 km<sup>2</sup>, and, on average, each line has dimensions of 420 m x 6000 m.

#### 3.2. Specim data (Hyperspectral laboratory data)

This data set consisted of high-resolution hyperspectral images of 62 samples of thin sections rock slabs acquired with the SisuCHEMA hyperspectral imager, a high-speed push-broom system developed by Spectral Imaging Ltd., Finland (Specim, 2015). The SWIR setup consisted of a Specim SWIR-LVDS-100-N25E camera and OLESMacro lens acquiring images with 384 pixels per line and a spatial resolution of 26 µm. It operates in a spectral range of 930 to 2540 nm, with a spectral resolution (FWHM) of 10 nm, a spectral sampling of 6.3 nm, and 288 bands.

The thin sections rock slabs were derived from rock hand specimens collected in the Buckskin range area as part of the research of Michael Sepp, a PhD candidate, and his supervisor Prof. John Dilles, from Oregon State University who collaborated with this research.

#### 3.3. Petrographic, chemical and mineralogical data

This data set consisted of petrographic, chemical, and mineralogical data of the 62 samples used for the hyperspectral laboratory study. The analytical tools used were electron microprobe analysis (EMPA) and scanning electron microscope-backscattered electron (SEM-BSE) results. Most of the samples were analysed by, at least, one of these techniques. To assist on the interpretation of the results, this study used geological, alteration and outcrop maps of the area where the samples were collected. Also, a digital elevation model (DEM) with a spatial resolution of 20 cm/pixel and an orthophoto with a 5 cm pixel spacing were used to improve the analysis of the results. The data was also acquired and developed by Michael Sepp (Sepp, 2020).

## 4. METHODOLOGY

### 4.1. Introduction

This methodology was developed so it could be applied to both the airborne ProSpecTIR data as well as the laboratory-based Specim data. The aim was to create outputs which could be analysed and compared.

To identify the surface mineralogy and determine the spatial distribution of the occurrence of the pyrophyllite-muscovite association, the first stage for processing both data was mapping the wavelength position and depth of absorption features using the Wavelength Mapper (described in detail on the following section) (van Ruitenbeek et al., 2014) in the 2100-2400 nm range. This initial approach was defined to give an overview of the mineral association present in the study area which has the main absorption features in the range of 2100-2400 nm such as phyllosilicates (e.g. muscovite, pyrophyllite, kaolinite), sorosilicates (e.g. epidote, zoisite, zunyite), sulphates (e.g. alunite, jarosite) and carbonates (e.g. calcite, dolomite) (Clark et al., 1990) (Fig. 4.1). To guarantee that features in other wavelength ranges were also included in this analysis, both data sets were mapped in the following wavelength ranges: 1300-1600 nm, 1650-1850 nm, and 1850-2100 nm. To improve the level of detail of the overview of the mineral association and enhance the difference between the mineralogy present, an additional range was chosen between 2150-2250 nm and applied to both data sets.

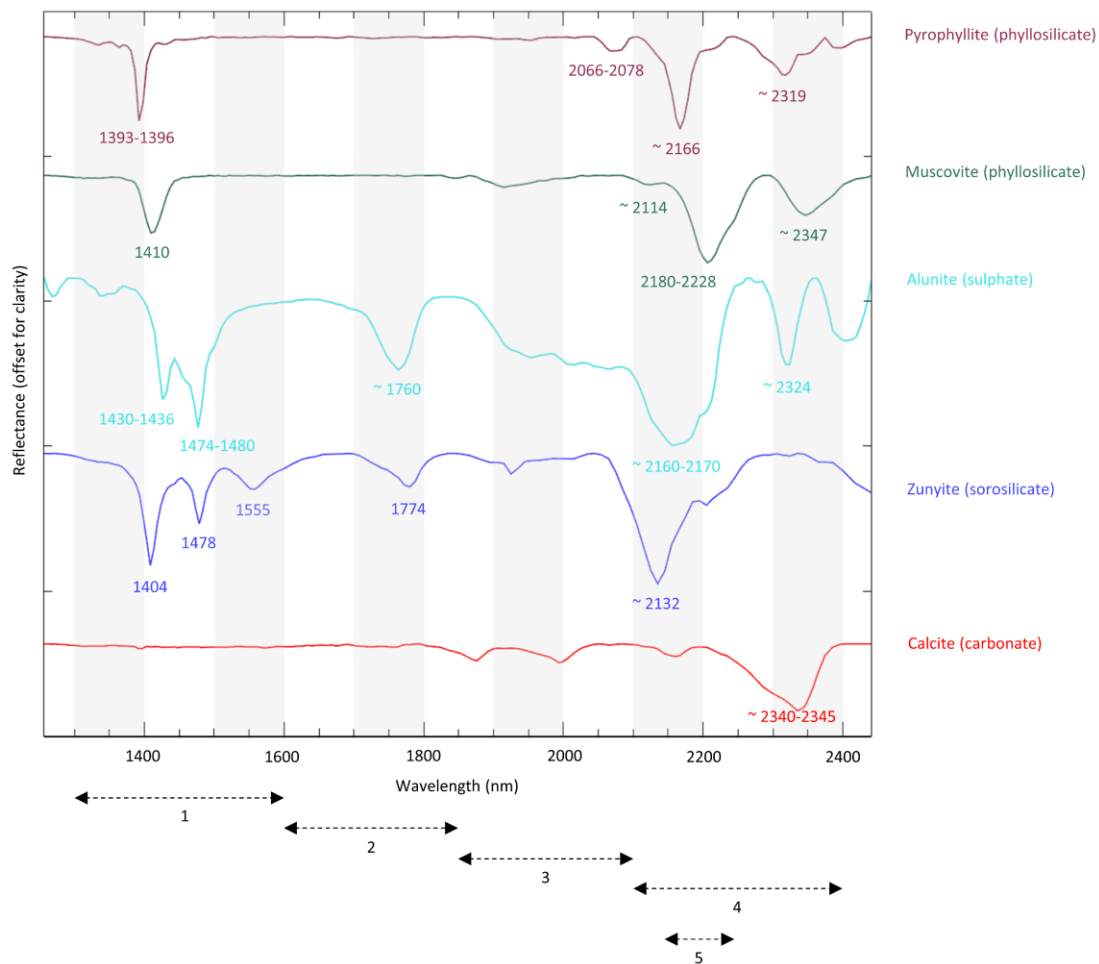


Figure 4.1: Spectral profile of mineral groups which are active in the 2100-2400 nm range. Convex hull removal applied on spectra from the USGS Spectral Library (Pontual et al., 1997; Kokaly et al., 2017). Numbers 1-5 represent the wavelength intervals used for producing the wavelength maps. 1: 1300-1600 nm; 2: 1650-1850; 3: 1850-2100 nm; 4: 2100-2400 nm; 5: 2150-2250 nm.

As observed in fig. 4.1, each wavelength interval presented an important absorption feature that could be used to identify hydrothermal alteration minerals such as pyrophyllite, alunite and muscovite, especially on the Specim data, due to its high spatial and spectral resolution.

To address the textural relationship of pyrophyllite and muscovite, spectral indices were developed for both data sets to highlight the relative proportion of the two minerals. For the Specim data, an additional spectral index based on the shift of the wavelength position of the Al-OH absorption feature for muscovite was defined to enhance the contact zones between both minerals.

To compare the spectral information obtained through the analysis of the wavelength maps and the spectral indices on the Specim data and to improve the analysis of the textural relationship of pyrophyllite and muscovite, this research used the scanning electron microscope (SEM-BSE) images. For the ProSpecTIR data, the results from the wavelength maps and spectral index were combined with digital elevation model (DEM), geological and alteration maps of the study area to improve the analysis of the spatial distribution of pyrophyllite and muscovite.

The following sections contain a detailed description of the different stages of the methodology.

## **4.2. Data pre-processing**

### **4.2.1. ProSpecTIR data (Hyperspectral airborne data)**

The flight scenes provided by SpecTIR, LLC were already pre-processed for radiometric and spectral calibration, radiance processing, and reflectance processing (ATCOR4/MODTRAN4) with an additional step of refined atmospheric correction for CO<sub>2</sub> and water features, using a proprietary program of SpecTIR, LLC. According to SpecTIR (2008), for the water absorption regions at 1400 and 1900 nm, a non-linear interpolation was used by adjusting the curves with a hull of template vegetation or soil spectrum.

Next, internal geometry map (IGM) files were used for georeferencing the scenes. Although the study area was smaller than the area covered by the flight lines, this research opted not to generate a spatial subset of the data at this initial stage. Hence, additional information on the surrounding area could be used to assist in the interpretation of the results.

The following step was the generation of a spectral subset of the flight scenes from 1100 to 2400 nm to reduce the size of the data and facilitate the manipulation of it. Also, this subset produced airborne data which considered the main absorption features in the SWIR range and were comparable to the laboratory data regarding the wavelength range.

### **4.2.2. Specim data (Hyperspectral laboratory data)**

To obtain the images, each sample was individually placed in a sandbox and, taken to the SisuCHEMA SWIR setup (Appendix II). The use of the sandbox during the acquisition was to have a background with known composition and compensate for the variable thickness to guarantee focused images.

The procedure began with the measurement of the sample, the white reference target, and the dark current signal. These two additional measurements were used for the calibration process to reflectance data. Following, the image was spectrally subset to remove noisy bands (bands 1-16 and 288), at the beginning and end of the wavelength range. Lastly, a de-stripping and a spectral mean filter were applied on the data to remove artefacts originated by calibration errors and to smooth the spectra, respectively (Bakker & van Ruitenbeek, 2019; Hecker et al., 2019a).

As the samples were wider than the field of view of the imager, each sample was divided into three or four strips, depending on the width of the sample. Using ENVI version 5.5 (Exelis Visual Information Solutions, Boulder, Colorado), a mosaic of each sample was created by first, defining a raw mosaic with the overlapping areas from all strips still visible. The second step determined the tie points used for the removal of the overlap (Fig. 4.2). Next, the mosaicked image of each sample was spatially subset to maintain only the area of the sample and exclude the sandbox where the sample was placed. Also, a second spectral subset was applied to produce an image with the same wavelength range of the airborne data, from 1100 to 2400 nm.

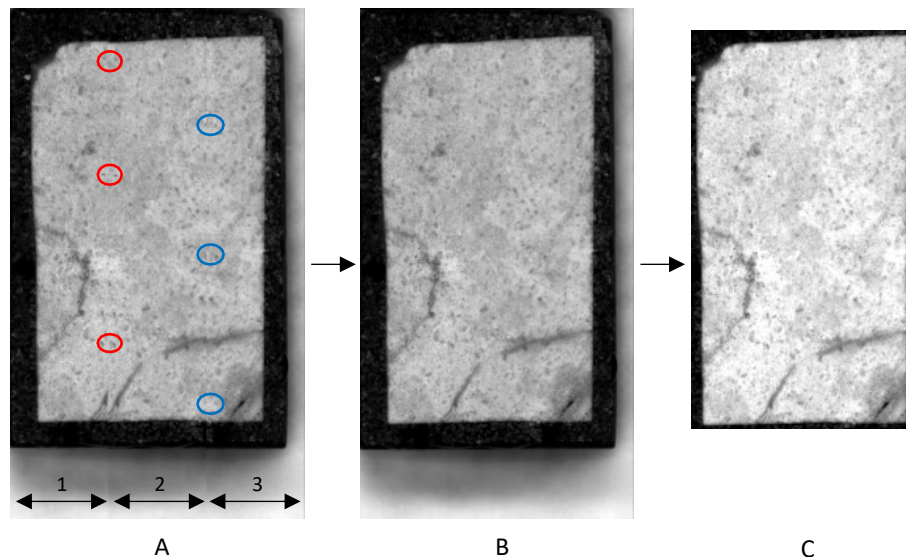


Figure 4.2: Representation of a sample mosaicking process with the display of the strips of a sample (1-3) and definition of the pixels (red and blue circles) used for the mosaicking (A), the mosaicked image of a sample (B) and the final image generated after the spatial subset to consider only the sample (C).

### 4.3. Minimum Wavelength Mapper

This is a method based on the characterisation of the spectral absorption features such as the position and depth. Thus, it generates a proxy for mineralogy, mineral abundance, and spatial relations in a single image as a colour-coded map in which hue represents different absorption wavelengths and brightness express the variations in depth (Bakker et al., 2011; Hecker et al., 2019c). The Minimum Wavelength Mapper is a tool of the Hyperspectral Python (HypPy) software developed by Wim Bakker of the Faculty ITC-University of Twente, Enschede, The Netherlands.

The procedure starts with a continuum removal (hull quotient technique) over the wavelength range of interest. Then, through a parabolic interpolation over three consecutive bands in which the centre band has the lowest reflectance value, the wavelength position of the deepest absorption feature is calculated (Fig. 4.3). The product of this step is a two-band image which comprises the interpolated wavelength position and the interpolated depth of the deepest absorption feature. The second step combines these two bands in a single image, as mentioned in the previous paragraph. The method allows the user to define spectral subsets for both steps, focusing on specific absorption features in a certain range. Another important aspect when applying this method, aside from the spectral subset adjustment, is the possibility of modifying the depth stretch (brightness) to improve the intensity contrast. This helps to suppress noise from indistinct features in the resulting images (Hecker et al., 2019c).

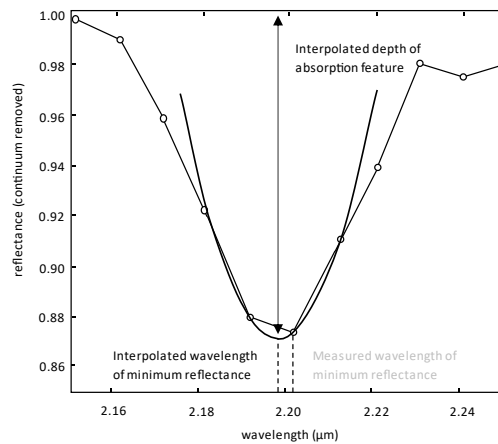


Figure 4.3: Determination of the interpolated wavelength position of the deepest absorption feature through parabolic interpolation (van Ruitenbeek et al., 2014).

The Minimum Wavelength Mapper method has the advantage of delivering to the user an initial idea of the mineral distribution, composition, and the microstructure present in the study area or rock specimen. It does not require previous knowledge of the area or a reference library to obtain the mineralogic information. A crucial aspect of the method, critical for the development of this research, is that it can detect small shifts in wavelength positions which can be related to variations in the mineral chemistry (Hecker et al., 2019c). The limitation of the method is associated with the fact that minerals with overlapping deepest features are not possible to be differentiated. Thus, one of the alternatives to overcome this is the use of the second deepest absorption features and the use of different spectral subsets, both previously discussed.

Proxy mineralogy overview and small shifts detection in wavelength position, were essential aspects for the selection of this method. These are the criteria which lead this research to opt for the Minimum Wavelength Mapper tool, instead of hard classifiers methods such as spectral angle mapper (SAM) and linear spectral unmixing (LSU). As discussed by van Ruitenbeek et al. (2006), classification methods based on reference library and mineral endmembers have several disadvantages related to different stages of the processing procedure. However, the most critical disadvantage for implementing spectral angle mapper (SAM) or linear spectral unmixing (LSU) on this research was the fact that subtle changes in the wavelength position of absorptions features cannot be detected or represented by different endmembers.

#### 4.3.1. ProSpecTIR wavelength maps

On the Minimum Wavelength Mapper, step 1 (spectral range where the deepest feature is searched in) was defined, and a two-band image was created. Step 2 was the spectral subset and depth stretch definition. All the airborne ProSpecTIR wavelength maps were produced with the automatic depth stretch of the tool, which is 30-95% percentile stretch. As discussed by Hecker et al. (2019c), the use of the default values creates a higher consistency between flight lines and reduces the display of indistinct features. The spectral subset of step 2 was the same range as the spectral range in step 1 with exception to the 2150-2250 nm map. For this case, step 1 was 2100-2400 nm, and the spectral subset on step 2 was 2150-2250 nm.

The wavelength maps for 1300-1600 nm, 1650-1850 nm and, 1850-2100 nm intervals were generated with the same procedure as the 2100-2400 nm, automatic depth stretch and no spectral subset on step 2. The flight lines were processed separately and in its full extension. Following that, the outputs were mosaicked, and a spatial subset was defined based on the limits of the study area. The mosaic was created at the end of the procedure to compensate for small flight line image differences and to get a more consistent mosaic across the flight lines.

### 4.3.2. Specim wavelength maps

To generate comparable outputs, initially, the procedure performed for the laboratory Specim data was the same as for the airborne ProSpecTIR data. All the setups have identical step 1 and step 2 wavelength ranges, with exception to the 2150-2250 nm range. For this setup, the step 1 range was 2100-2400 nm, and the step 2 subset was 2150-2250 nm (Table 4.1). Therefore, a set of 5 wavelength maps were created to facilitate an overview of the mineralogy present in each sample.

Differently from the airborne procedure, for the laboratory Specim data set, additional and narrower wavelength intervals were used to better characterise the mineralogy present (Table 4.1).

	Primary wavelength ranges (nm)					Additional wavelength ranges (nm)		
Step 1	1300-1600	1650-1850	1850-2100	2100-2400	2100-2400	2100-2400	2100-2400	2100-2400
Step 2	1300-1600	1650-1850	1850-2100	2100-2400	2150-2250	2160-2215	2160-2180	2180-2215
Wavelength map	1300-1600	1650-1850	1850-2100	2100-2400	2150-2250	2160-2215	2160-2180	2180-2215
ProSpecTIR	✓	✓	✓	✓	✓			
Specim	✓	✓	✓	✓	✓	✓	✓	✓

Table 4.1: Primary wavelength ranges indicate the wavelength maps created for both data sets. Additional wavelength ranges indicate the narrower wavelength ranges used only for the Specim data set to improve mineralogical characterisation. Step 1: spectral range where the deepest feature is searched in; Step 2: spectral subset; Wavelength map row indicates the final output.

These additional ranges were defined based on the results obtained from the wavelength maps created on the previous step (2100-2400 nm and 2150-2250 nm, mainly) and, consequently, the mineralogy present in each sample. Below, there is a brief explanation of the criteria selected for the additional wavelength maps.

1. 2160-2215 nm: to highlight samples with features varying from pyrophyllite to muscovite.
2. 2160-2180 nm: to highlight samples with a predominance of alunite/pyrophyllite features.
3. 2180-2215 nm: to highlight samples with a predominance of muscovite features.

In fig. 4.4, an example of the legend from a wide (A) and a narrow (B) wavelength interval maps illustrates the enhancement on the mineralogy present and how the muscovite range is better separated from the pyrophyllite range.

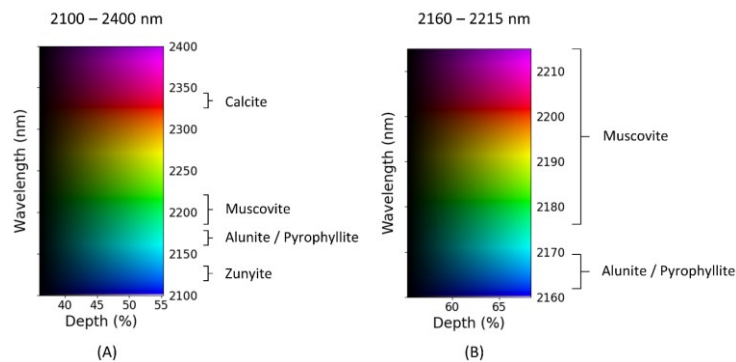


Figure 4.4: Example of the legend of a wavelength map from a wide (A) and a narrow (B) interval showing the distinction achieved with the narrow range.

Lastly, the wavelength map procedure was repeated with an adjustment of the depth stretch from 0 to 50% depth. The automatic depth stretch might exclude pixels with a shallow absorption feature (dark pixels) (Hecker et al., 2019c). Thus, the adjustment of this parameter to consider features from 0 to 50% depth can facilitate the display of all the mineralogy in the sample, especially at the border of each crystal.

#### 4.4. Spectral index

A spectral index can be understood as a tool to indicate the relative abundance of certain features by combining spectral parameters extracted from reflectance spectra (Oniemayin et al., 2016; van Ruitenbeek et al., 2005). Based on a similar approach which van Ruitenbeek et al. (2005) used for defining the white mica alteration index, this research developed spectral indices by analysing the position of absorption features which were diagnostic for identifying pyrophyllite and muscovite.

Before the development of the indices, a continuum removal (hull quotient technique) was applied to both data sets, following the same procedure as the Minimum Wavelength Mapper method. Since the spectral resolution of the data set was crucial when selecting the bands for the index, the explanation is divided by data set.

##### 4.4.1. ProSpecTIR spectral index

The spectral index of the ProSpecTIR data was based on the analysis of the wavelength position of the Al-OH absorption feature of pyrophyllite and muscovite. Due to the spectral resolution of this data set and no diagnostic features in other wavelength ranges due to atmospheric absorption, this research opted to develop an index related to one range only.

The wavelength position of the Al-OH absorption feature in pyrophyllite at 2166 nm can be used to differentiate it from muscovite at 2180-2228nm. Thus, the spectral index was defined as a simple ratio of the reflectance of the wavelength position of the Al-OH deepest absorption feature of pyrophyllite over the reflectance of the wavelength position of the same feature for muscovite (Fig. 4.5). For the muscovite Al-OH absorption feature, the deepest feature was derived from the results of the wavelength maps. For example, if the wavelength map indicated that the wavelength position of the Al-OH deepest absorption feature was at 2200 nm, the reflectance value of this position would be used for the index.

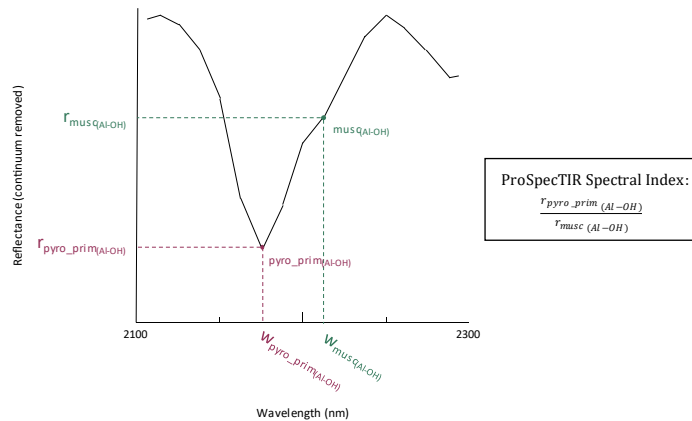


Figure 4.5: Spectral curve with the parameters used for the airborne ProSpecTIR index.  $r_{pyro\_prim(Al-OH)}$  is the reflectance value of the wavelength position of the deepest Al-OH feature for pyrophyllite.  $r_{musc(Al-OH)}$  is the reflectance value of the wavelength position of the deepest Al-OH feature for muscovite.

As observed in fig. 4.1, alunite, a mineral which is also part of the mineral association, presents an absorption feature at 2160-2170 nm and could influence the index. To overcome this obstacle, when displaying the resulting image of the spectral index, the wavelength map from 1650-1850 nm was used to visualize the diagnostic absorption feature for alunite at 1760 nm. Thus, this visual comparison would address the separation of alunite dominant areas from the pyrophyllite-muscovite association and prevent wrong interpretation of the index map.

#### 4.4.2. Specim spectral index

The spectral indices of the Specim data were based on two intervals which are diagnostic for the differentiation of pyrophyllite from muscovite. The wavelength range of the Al-OH absorption feature (pyrophyllite: 2166 nm; muscovite: 2180-2228 nm) and a secondary feature which is diagnostic for pyrophyllite, 2066-2078 nm, also associated with the Al-OH functional group (Clark et al., 1990). For the pyrophyllite absorption feature at 2066-2078 nm, the deepest feature was manually selected at 2077 nm since it was slightly deeper at this position according to preliminary results of the wavelength maps. For the muscovite Al-OH absorption feature, the deepest feature was derived from the results of the wavelength maps. For example, if the wavelength map of a sample indicated that the wavelength position of the Al-OH deepest absorption feature was at 2195 nm, the reflectance value of this position would be used for the index.

From these absorption features, two spectral indices were used with the purpose of highlighting the relative proportion of pyrophyllite and muscovite. The first index was created based on the interference with zunyite and alunite. These interferences are going to be explained along with the description of the indices. The second index was the same index used for the airborne ProSpecTIR data adapted to the wavelength position of the bands of laboratory Specim data.

The first spectral index (referred in the results section as the spectral index (1)) is the ratio between the deepest position of the 2066-2078 nm feature and its shoulder (manually selected at 2105 nm) and multiplied by the ratio of the reflectance value of the wavelength position of the Al-OH absorption feature of pyrophyllite over the reflectance value of the wavelength position of the same feature for muscovite (Fig. 4.6).

The issue of this index was that zunyite has a deep feature at 2065-2185 nm (Fig. 4.1), in the same range as the shoulder of the 2066-2078 nm absorption feature (Fig. 4.1). Thus, zunyite lowered the shoulder and overestimated the occurrence of muscovite in the sample since the value of the depth of the 2066-2078 nm feature was always greater than 1. Therefore, the index developed for the ProSpecTIR data was used to overcome this situation.

The second spectral index (referred in the results section as the spectral index (2)) is the same index developed for the airborne ProSpecTIR data set. Thus, in addition to overcome the zunyite interference, this ratio could allow a clear identification of the limits of areas which were pyrophyllite or muscovite dominant, since, at first, there would not be any overestimation of both minerals.

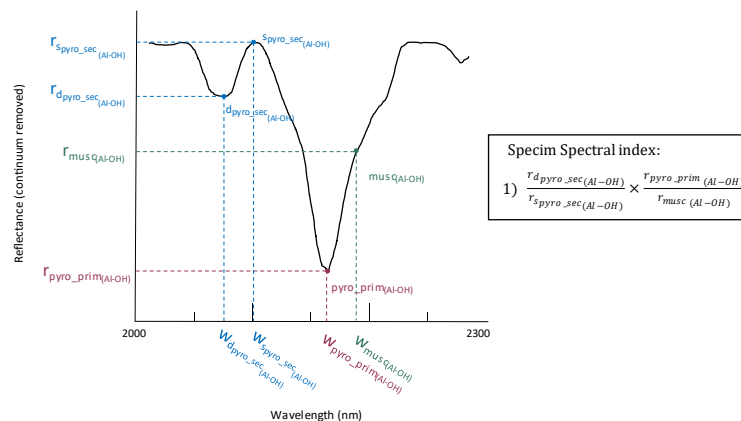


Figure 4.6: Spectral curve with the parameters used for the laboratory Specim spectral index.  $r_{dpyro\_sec(Al-OH)}$  is the reflectance value of the deepest position of the Al-OH secondary feature of pyrophyllite.  $r_{spyro\_sec(Al-OH)}$  is the reflectance value of the shoulder position of the Al-OH secondary feature of pyrophyllite. The ratio between these parameters is multiplied by the ratio of  $r_{pyro\_prim(Al-OH)}$  which is the reflectance value of the wavelength position of the primary deepest Al-OH feature for pyrophyllite and  $r_{musq(Al-OH)}$ , the reflectance value of the wavelength position of the deepest Al-OH feature for muscovite.

In samples where alunite was present, an interference could occur in both indices, similarly to the situation on the ProSpecTIR data previously described. To address this issue, a similar approach was adopted, and the wavelength map from 1650-1850 nm was used to identify the occurrence of the diagnostic absorption feature for alunite at 1760 nm.

#### 4.4.3. Decision tree classification

To facilitate the visualisation of this ratio and to create a colour scheme comparable between the entire data set, a decision tree classification method was developed for both data sets. To define the values which were going to be used on this decision tree, a synthetic linear mixture of the purest pyrophyllite and muscovite spectra was created. The 5 flight lines were analysed with the use of the wavelength maps to select the pixels which were most representative for a pure pyrophyllite and muscovite spectrum, based on the high intensity (deep) features. The same procedure was applied in all the 62 Specim samples. These pure spectra were characterised as the endmembers of the linear mixture, and then, they were mathematically mixed on a 10% interval basis, as observed on fig. 4.7. The next step was to apply the ratio on this synthetic data to define the values which were related to each interval.

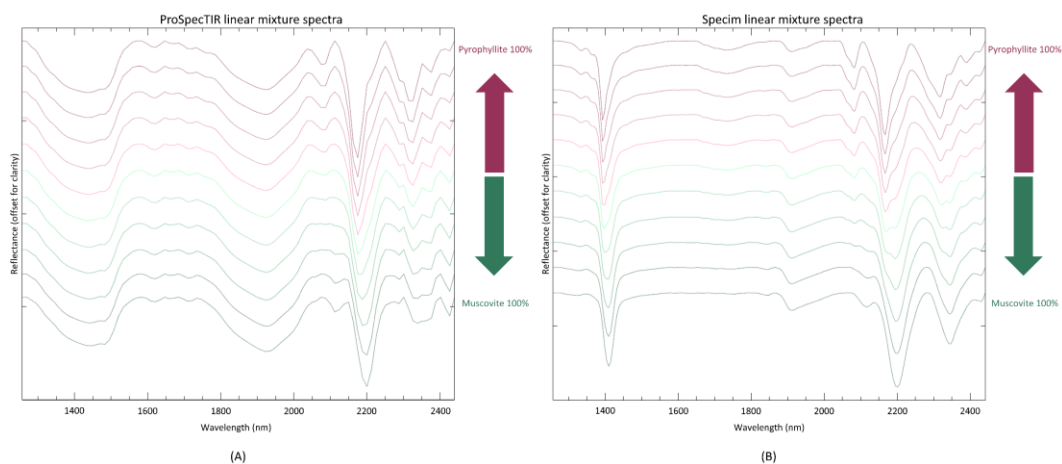


Figure 4.7: Spectral profile of the linear mixtures developed for both data sets. (A) represents the spectral curve of each class defined for the airborne ProSpecTIR data. (B) represents the spectral curve of each class defined for the laboratory Specim data. The top and bottom curves represent the endmembers of pyrophyllite and muscovite, respectively. In between are the curves with a 10% interval mixture.

#### 4.4.4. Spectral index of the Al-OH absorption feature of muscovite

Early results showed a shift in the wavelength position of the Al-OH deepest absorption feature of muscovite at contact zones between pyrophyllite and muscovite. Pixels mixed at around 50% pyrophyllite and 50% muscovite indicated the wavelength position of the Al-OH absorption feature of muscovite varying from 2189 nm to 2195 nm. To illustrate this shift, a spectral index was developed for the laboratory Specim data (Fig. 4.8). Since the shift was identified at contact zones between both minerals, only the areas classified as pyrophyllite 50-60% and muscovite 50-60% from the decision tree classification above were considered for this new classified image. Like the previous spectral indices, this index was derived from a continuum removal data set.

$$\frac{r_{b2189}}{r_{b2195}} \begin{cases} \text{Index} > 1: \text{ the wavelength position of the Al-OH} \\ \text{absorption feature for muscovite at 2195 nm.} \\ \text{Index} < 1: \text{ the wavelength position of the Al-OH} \\ \text{absorption feature for muscovite at 2189 nm.} \end{cases}$$

Figure 4.8: Spectral index defined to illustrate the shift in the wavelength position of the Al-OH absorption feature of muscovite in the laboratory Specim data. The index was derived from a continuum removal data set, hence the results as displayed.  $r_{b2189}$  is the reflectance value at 2189 nm, and  $r_{b2195}$  is the reflectance value at 2195 nm.

## 5. RESULTS AND DISCUSSIONS

### 5.1. ProSpecTIR wavelength maps

This section presents the results of the wavelength maps obtained from the airborne ProSpecTIR data. For this dataset, five wavelength maps were produced to characterise the surface mineralogy of the study area focusing on hydrothermal alteration minerals. Also, to observe the spatial distribution of the pyrophyllite-association. Several patterns were observed in these maps and are described in the following paragraphs. Differences in the wavelength position of the absorption features are influenced by the spectral resolution and the central wavelength position of the bands in the airborne ProSpecTIR data.

The wavelength maps of the study area are presented in fig. 5.1 (wavelength maps for the full extent of the flight lines can be found in Appendix IV).

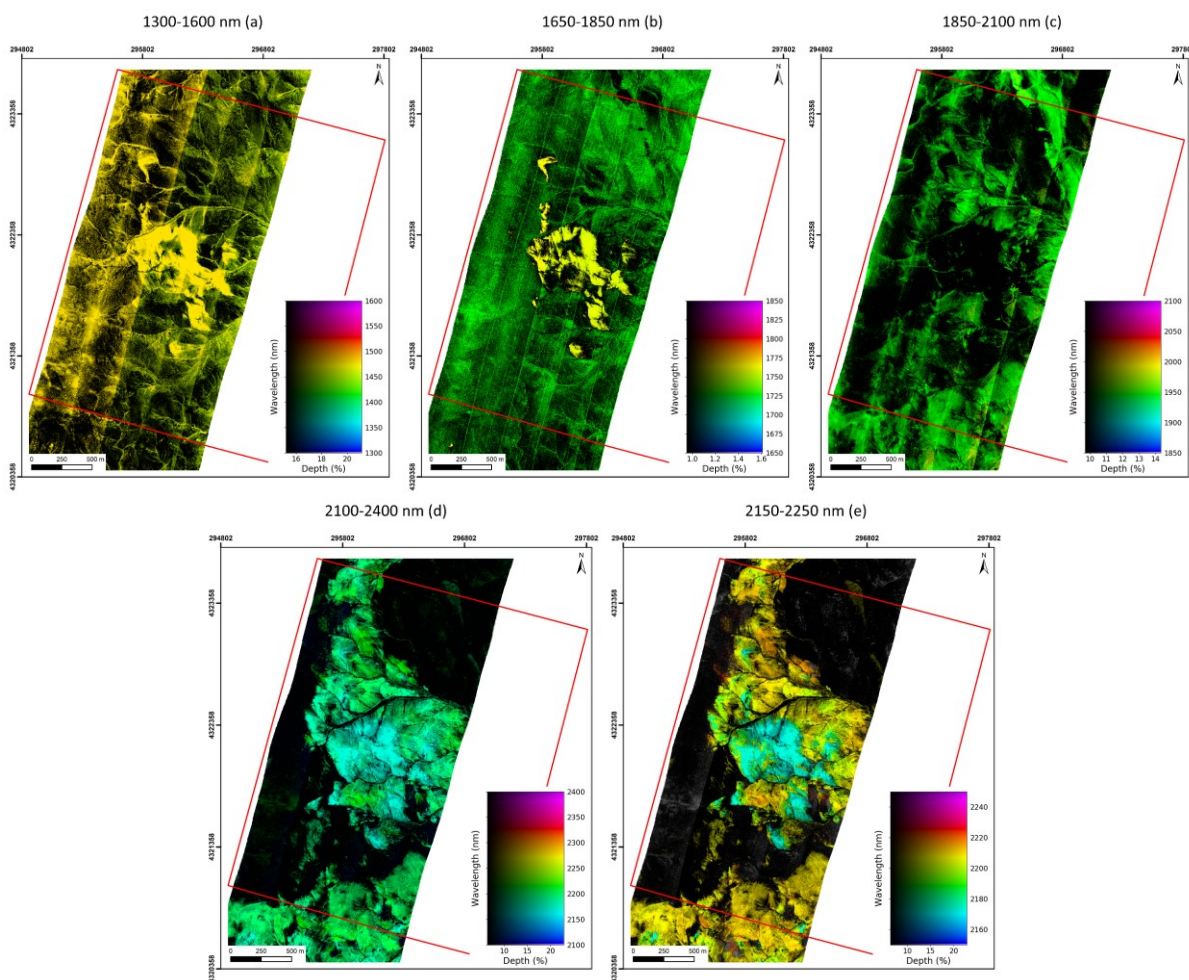


Figure 5.1: Wavelength maps of the airborne ProSpecTIR data of the study area (red polygon). Maps produced with automatic depth stretch and no secondary spectral subset, with exception to the interval of 2150-2250 nm (subfigure e).

The map created for the 2100-2400 nm range (Fig. 5.1d) gave a preliminary indication of the mineralogy of the study area with absorption features varying from 2150-2250 nm. Nevertheless, with the use of a narrow wavelength range map, the 2150-2250 nm (Fig. 5.1.e), it was possible to refine the variation of the wavelength position of the absorption features to an interval of 2165-2220 nm, approximately. As discussed in the methodology chapter, the absorption features related to shorter wavelength ranges (2165-2175 nm) could correspond to alunite  $\pm$  pyrophyllite (light cyan, fig. 5.1.d and 5.1.e). Features associated

with a longer wavelength range (2180-2228 nm) could correspond to muscovite (green to orange, fig. 5.1.e). Most of the dark areas indicated pixels with a very shallow absorption feature, although, in some parts of the 2100-2400 nm map (Fig. 5.1d), dark red pixels (absorption feature at around 2330 nm) were verified. This absorption feature could correspond to Mg-OH features, for example, Mg-rich chlorites.

Therefore, with a closer look at the central region of the study area (Fig. 5.2), it was possible to characterise a central region with a predominance of alunite ± pyrophyllite surrounded by a muscovite varying from short to long-wavelength range. In fig. 5.2, the 2150-2250 nm map (a) was used to present the mineralogy overview combined with the spectral profile (b) of each region. The spectral curves were extracted from different regions of the study area as indicated by the numbers in the wavelength map (Fig. 5.2.a) and the correspondent curves in the spectral profile (Fig. 5.2.b).

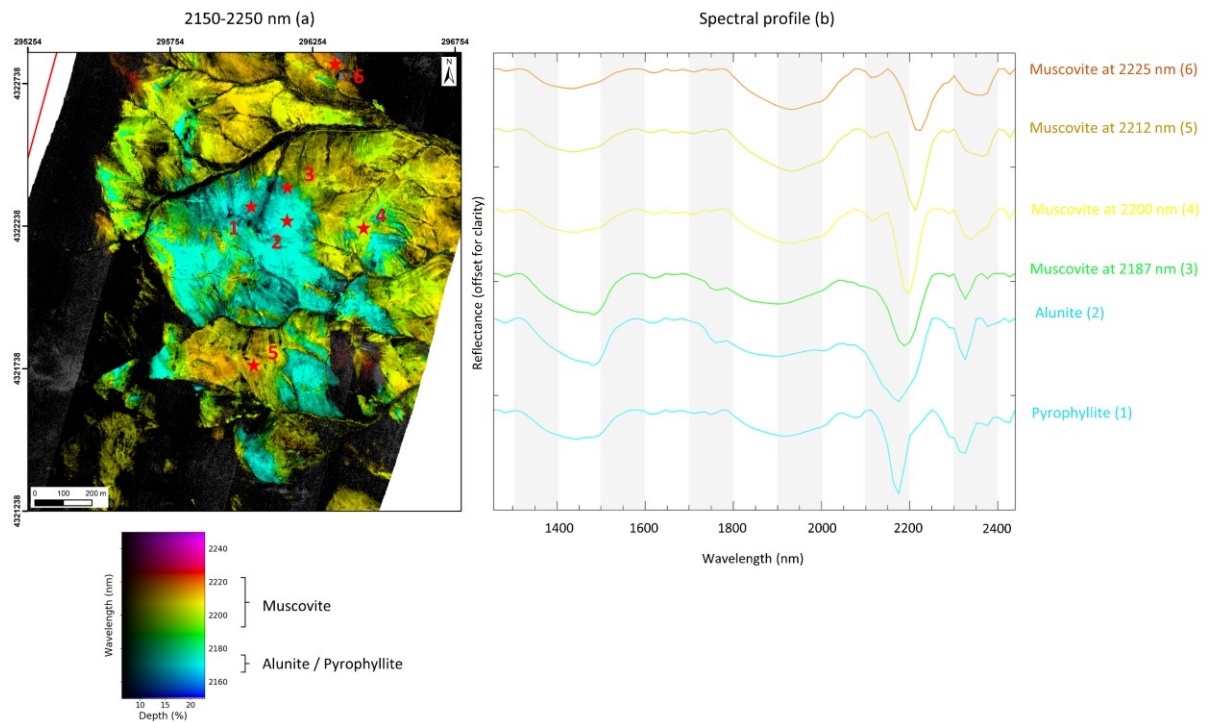


Figure 5.2: Spectral curve (b) observed in the central region of the study area. The colours of the spectral curves are in accordance with the colours illustrated in the 2150-2250 nm wavelength map (a).

The alunite ± pyrophyllite region in the centre of the study area, (light cyan, fig. 5.1.d and 5.1.e), is also highlighted in the 1650-1850 nm map (fig. 5.1.b and 5.3.a). The absorption features associated with this pattern in this map occurred at 1760 nm (bright yellow area, fig. 5.3.a). By knowing that alunite and pyrophyllite have an overlap feature at 2175 nm, but only alunite has a feature at 1760 nm, the 1650-1850 nm and 2150-2250 nm maps (Fig. 5.3a-b) were used to indicate areas of pyrophyllite predominance. This difference was also indicated in the spectra of the area (Fig. 5.3c).

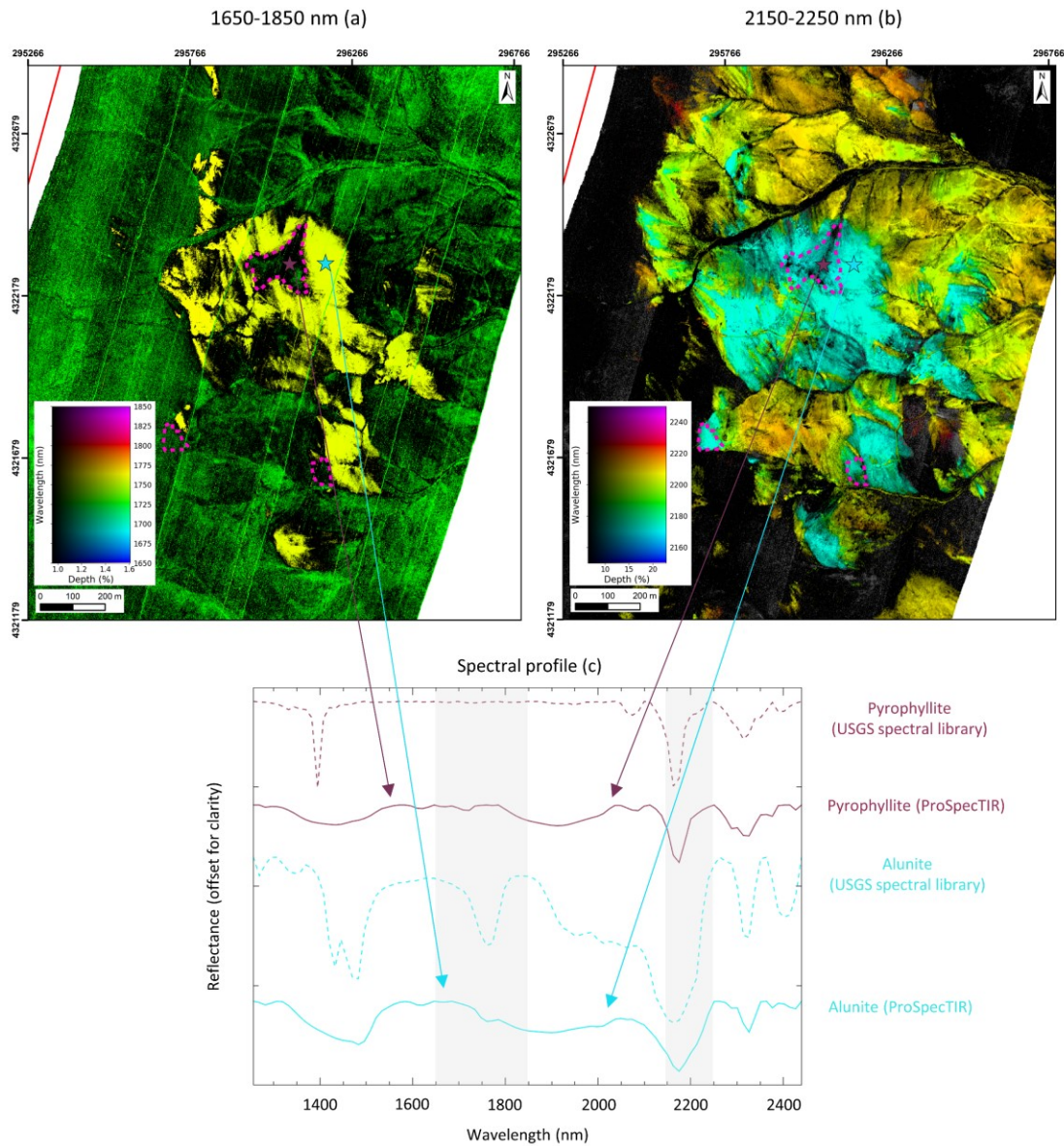


Figure 5.3: Indication of the areas in the central region of the study area that did and did not present an absorption feature at 1760 nm and a comparison with USGS Spectral Library spectra of alunite and pyrophyllite (Kokaly et al., 2017). Indication of pyrophyllite-rich zones (magenta dashed polygons in (a) and (b)). In (c), grey bands in the background indicate the range of the wavelength maps (left band: 1650-1850 nm; right band: 2150-2250 nm).

The shift in the wavelength position of the Al-OH absorption feature of muscovite is observed in the study area, and three types of contact zones were defined between muscovite and alunite ± pyrophyllite occurrences. The gradual contact zone is observed in fig. 5.4 (blue polygons) with the colour variation going from green (~ 2187 nm, here referred to as short-wavelength muscovite) to yellow (~2200 nm, here referred to as middle-wavelength muscovite) and orange (~2211 nm, here referred to as long-wavelength muscovite). The second type of contact was identified as abrupt (orange polygon, fig 5.4). It is represented by areas where there is an immediate change from alunite ± pyrophyllite zone to a middle to long-wavelength muscovite zone. In this case, there are none or very narrow occurrences of the short-wavelength muscovite. The third type of contact zone was named intercalary (magenta polygon, fig 5.4). It could also be classified as abrupt; however, it presents a pattern of small patches dominated by alunite ± pyrophyllite intercalated with small patches of short to middle-wavelength muscovite. This was interpreted as a different type of contact zone.

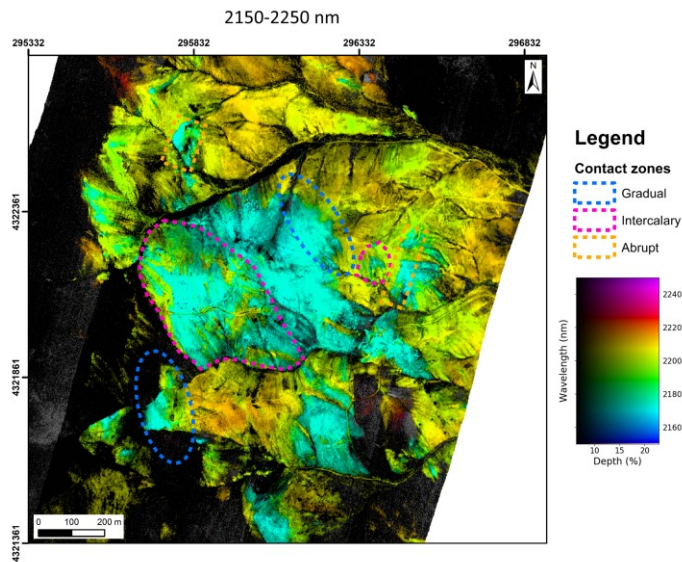


Figure 5.4: Identification of three different types of contact zones observed in the central region of the study area between muscovite-rich and alunite ± pyrophyllite-rich areas.

## 5.2. Specim wavelength maps

This section presents the results of the wavelength maps obtained from the Specim data. Due to the size of the data set and to maintain the analysis within the scope of the research, a few representative samples are presented here while the results of the remaining samples can be found in Appendix V. To facilitate the description and further analysis of the results, this section is going to be divided into two parts: samples with a predominance of either pyrophyllite, muscovite, or alunite (including a few accessory minerals like zunyite, topaz and dickite) and samples in which pyrophyllite and muscovite co-occurred, independently of their predominance.

Before presenting the mineralogy overview, a comparison of the wavelength maps is shown, obtained with automatic depth stretch (Fig. 5.5.a) and a 0-50% depth stretch (Fig. 5.5.b). As observed in fig. 5.5b, every pixel of the sample reveals the position of its main absorption feature with the 0-50% depth stretch (Fig. 5.5.b), but feature depth information is lost (i.e. saturated image). On the other hand, regions with shallow absorption features were not considered with the automatic depth stretch (Fig. 5.5.a). For the mineralogy overview, the wavelength maps were presented with the automatic depth stretch. In the case of samples with pyrophyllite and muscovite co-occurrence, the wavelength maps with the 0-50% depth stretch were presented to highlight the contact between the two minerals.

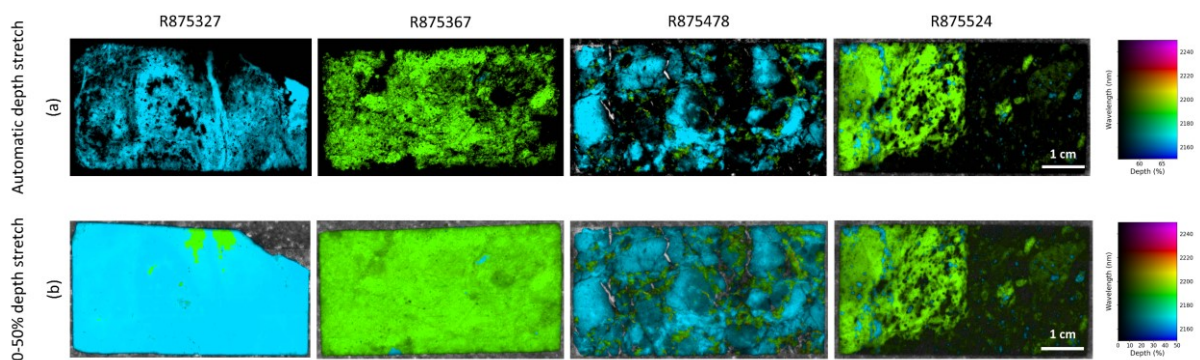


Figure 5.5: Comparison of wavelength maps produced by using the automatic depth stretch (a) and customised depth stretch (0-50%) (b) in the Minimum Wavelength Mapper tool. By only using the automatic depth stretch, was not possible to identify the occurrence of muscovite (light green, first sample, R875327 (b)) and pyrophyllite (light cyan, second sample R875367 (b)) would have been missed.

### 5.2.1. Mineralogy overview

In a sample with a predominance of muscovite (R875389, fig. 5.6.1a-8a), the hydroxyl (1410 nm) and water (1910 nm) absorption features were presented in the 1300-1600 nm (green, fig. 5.6.1a) and 1850-2100 nm (cyan, fig. 5.6.3a) maps, respectively. The Al-OH absorption feature was indicated by the green colour in the 2100-2400 nm map (Fig. 5.6.4a). The 2150-2250 nm map (Fig. 5.6.5a) showed that deepest absorption features were around 2200 nm and the narrower ranges (Fig. 5.6.6a-8a) confirmed the wavelength position of Al-OH absorption feature at around 2200 nm (red, fig. 5.6.6a; no colour, fig. 5.6.7a; yellow, fig. 5.6.8a).

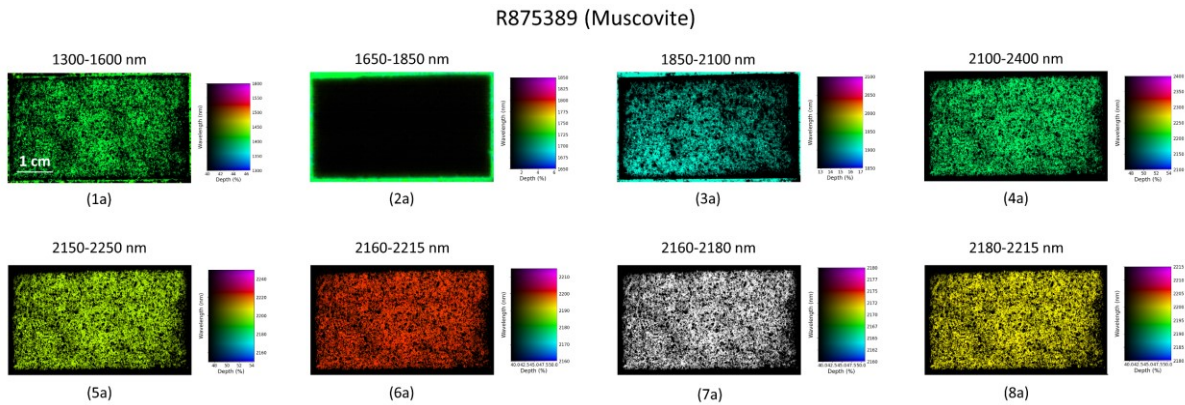


Figure 5.6: Wavelength maps of the sample R875389 with a predominance of muscovite confirmed by the green colour in the 2100-2400 nm map (4a) and the greenish, red, no colour and, yellow colours in the 2150-2250 nm (5a), 2160-2215 nm (6a), 2160-2180 nm (7a) and, 2180-2215 nm (8a) maps, respectively.

In a sample with a predominance of pyrophyllite (R875431, fig. 5.7.1a-8a), the hydroxyl absorption feature (1393 nm) was observed in light green in fig. 5.7.1a. The 1850-2100 nm map (Fig. 5.7.3a) showed a magenta colour indicating the presence of topaz and its absorption feature at around 2083 nm. Since the pyrophyllite secondary Al-OH absorption feature at this range (2066-2078 nm) is shallower and wider, the absorption feature captured in this map referred to topaz. The primary Al-OH absorption feature of pyrophyllite (2167 nm) was indicated by the light cyan in fig. 5.7.4a. The narrower ranges confirmed the wavelength position at around 2167 nm (light blue, fig. 5.7.5a; light green, fig. 5.7.6a; blue, fig. 5.7.7a; no colour, fig. 5.7.8a).

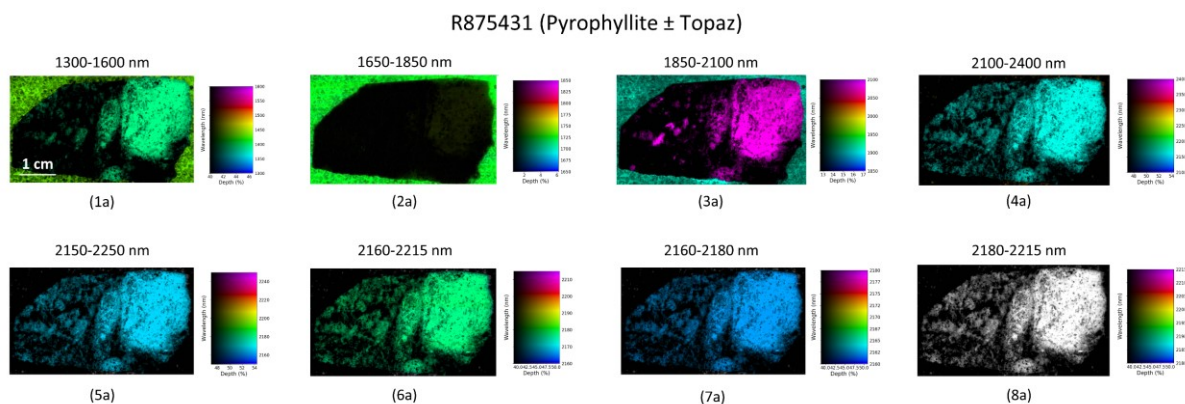
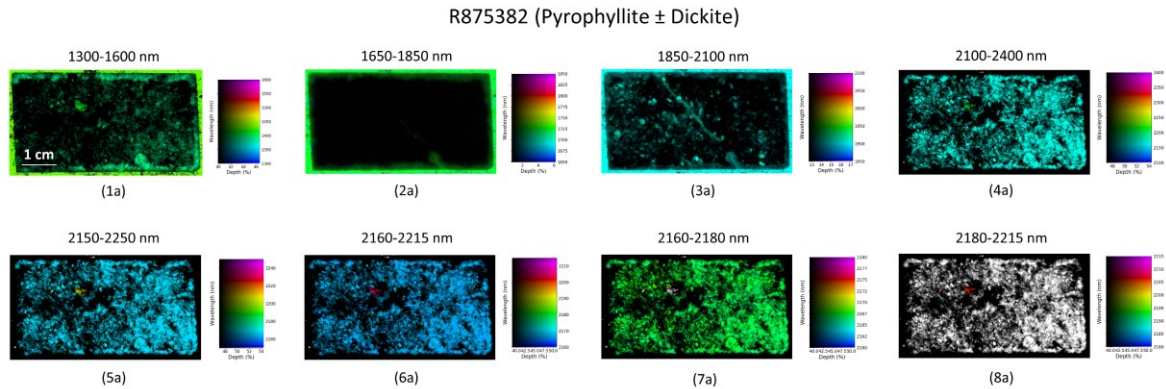


Figure 5.7: Wavelength maps of the sample R875431 with pyrophyllite confirmed by the light cyan colour in the 2100-2400 nm map (4a) and the light blue, light green, blue and, no colour in the 2150-2250 nm (5a), 2160-2215 nm (6a), 2160-2180 nm (7a) and, 2180-2215 nm (8a) maps, respectively. Topaz presence indicated by magenta in the 1850-2100 nm map (3a).

In another sample with pyrophyllite predominance (R875382, figure 5.8.1a-8a), the primary Al-OH absorption feature at around 2167 nm was observed by the light cyan colour in the 2100-2400 nm map

(Fig.5.8.4a) and confirmed in the narrower range maps (light blue, fig. 5.8.5a; blue, 5.8.6a; green, 5.8.7a; no colour, 5.8.8a). The presence of dickite was indicated by the green colour in the 2100-2400 nm map (Fig. 5.8.4a) and also highlighted in the narrower range maps (yellow, fig. 5.8.5a; magenta, fig. 5.8.6a; no colour, fig. 5.8.7a; red, fig. 5.8.8a).



*Figure 5.8:* Wavelength maps of the sample R875382 with pyrophyllite confirmed by the light cyan colour in the 2100-2400 nm map (4a) and light blue, blue, green and, no colour in the 2150-2250 nm (5a), 2160-2215 nm (6a), 2160-2180 nm (7a) and, 2180-2215 nm (8a) maps, respectively. Dickite presence indicated by green colour in the 2100-2400 nm map (4a) and yellow, magenta, no colour and, red in the 2150-2250 nm (5a), 2160-2215 nm (6a), 2160-2180 nm (7a) and, 2180-2215 nm (8a) maps, respectively.

In a sample with a predominance of alunite (664b, fig. 5.9.1a-8a), the hydroxyl double feature (1437-1488 nm) was observed in fig. 5.9.1a with darker yellow tones. The sulphate feature at around 1763 nm was indicated in yellow in the 1650-1850 nm map (Fig. 5.9.2a). The Al-OH absorption feature of alunite at around 2167-2172 nm was indicated in light cyan in the 2100-2400 nm map (fig. 5.9.4a) and confirmed by in the narrower range maps (light blue, fig. 5.9.5a-6a; green to yellow, fig. 5.9.7a; no colour, fig. 5.9.8a). The presence of zunyite was observed in green in the 1300-1600 nm map (due to double absorption features at 1409-1478 nm) and in blue in the 2100-2400 nm map (absorption feature at 2133 nm, fig. 5.9.4a). Zunyite did not present colour in the narrower range maps (Fig. 5.9.5a-8a) because its main absorption feature at around 2133 nm was out of range. Minor presence of muscovite indicated by a yellow area in the 2150-2250 nm map (Fig. 5.9.5a), also observed in the other narrower range maps (red, fig. 5.9.6a; no colour, fig. 5.9.7a; red, fig. 5.9.8a).

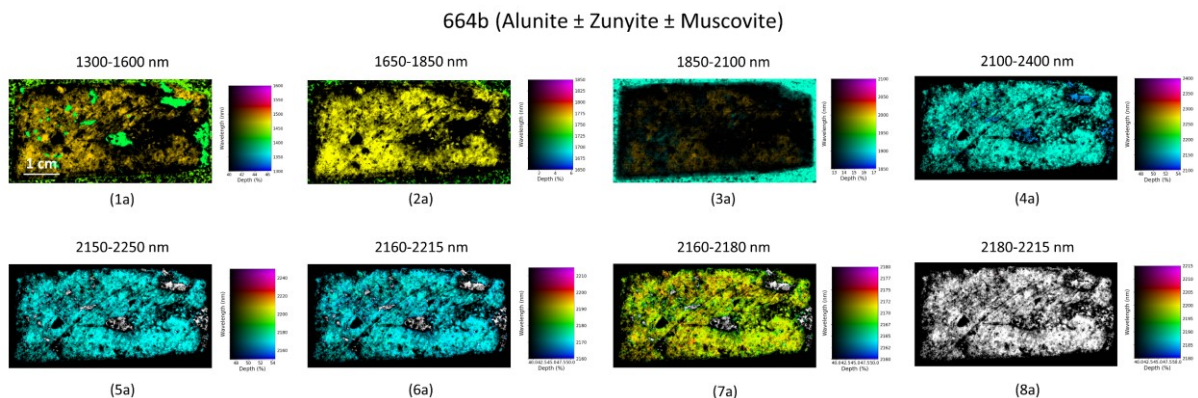


*Figure 5.9:* Wavelength maps of the sample 664b with alunite confirmed by the light cyan colour in the 2100-2400 nm map (4a) and light blue, light blue, green to yellow and, no colour in the 2150-2250 nm (5a), 2160-2215 nm (6a), 2160-2180 nm (7a) and, 2180-2215 nm (8a) maps, respectively. Zunyite presence indicated by the blue colour in the 2100-2400 nm map (4a) and no colour in the 2150-2250 nm (5a), 2160-2215 nm (6a), 2160-2180 nm (7a) and, 2180-2215 nm (8a) maps. Muscovite discrete presence indicated by the yellow colour in the 2150-2250 nm map (5a) and red, no colour and, red in the 2160-2215 nm (6a), 2160-2180 nm (7a) and, 2180-2215 nm (8a) maps, respectively.

The primary wavelength maps (1300-1600 nm, 1650-1850 nm, 1850-2100 nm, 2100-2400 nm and, 2150-2250 nm) could be used to identify most of the mineralogy present in this data set. In the case of the 1650-1850 nm map, spectral information was mainly presented on the outside resin because the absorption features at this range had less than 2-3% depth (an exception to the alunite sulphate feature, fig. 5.9.2a and fig. 5.10). A different depth stretch could be applied to present information on the inside of the sample, but very shallow absorption features might not be diagnostic. The additional and narrower wavelength maps (2160-2215 nm, 2160-2180 nm and, 2180-2215 nm) could be used to indicate the wavelength position of the Al-OH absorption feature of alunite and muscovite, mainly. These two minerals present variations in the position of their Al-OH absorption feature.

Alunite and pyrophyllite were indicated by light cyan colours in the 2100-2400 nm and 2150-2250 nm maps. This could lead to a wrong interpretation when the two minerals co-occur. In the case of pyrophyllite and alunite occurring as discrete and separate zones, the 1650-1850 nm map could be used to indicate the areas with an absorption feature at around 1760 nm, typical of alunite and not present in pure pyrophyllite. In the case of pyrophyllite and alunite occurring intimately mixed, the 1650-1850 map would not assist in the differentiation because the pyrophyllite spectra would present an absorption feature at 1760 nm as well. Thus, a distinction in the image of both minerals would not be feasible. The visual inspection of the representative spectrum would be necessary to analyse the shape of the overlapping feature at 2167 nm (alunite: shallow and wider; pyrophyllite: deeper and sharper) (Fig. 5.10).

Muscovite was indicated by green colour in the 2100-2400 nm map and, depending on the wavelength position of the Al-OH absorption feature, the colour could vary from green to red in the 2150-2250 nm map. Dickite could be indicated by similar colours if muscovite has its Al-OH absorption feature at around 2206 nm. In this case, the 1300-1600 nm map could be used to differentiate both minerals since dickite has a double feature at around 1380-1414 nm and muscovite at around 1410 nm (Fig. 5.10). Also, dickite could be differentiated from a mixture of pyrophyllite and muscovite by the shape of the Al-OH doublet absorption feature (wider than expected for a mixture of pyrophyllite and muscovite) and a longer wavelength position at 2172/2178-2206 nm (Fig. 5.10).

Topaz was indicated by magenta in the 1850-2100 map as a response to the absorption feature at around 2083 nm (Fig. 5.10). For zunyite, the identification was verified through the blue colour in the 2100-2400 nm map. The other wavelength maps did not indicate the presence of these minerals since its main absorption features were outside the range of the wavelength maps.

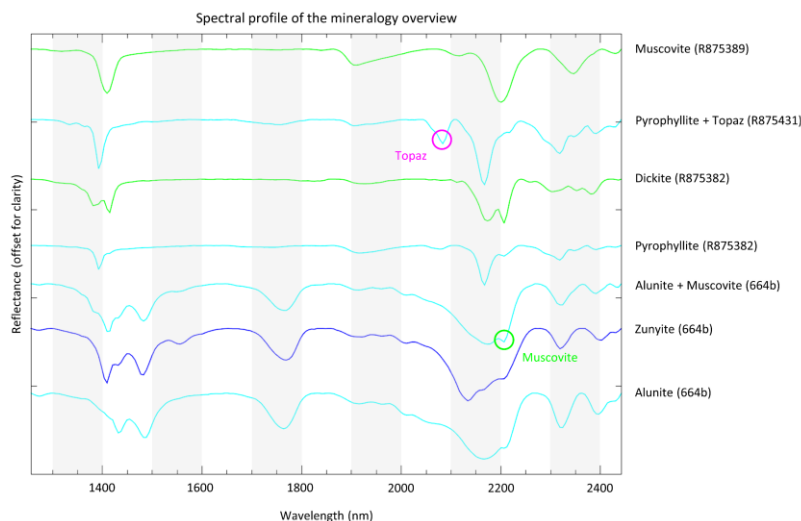
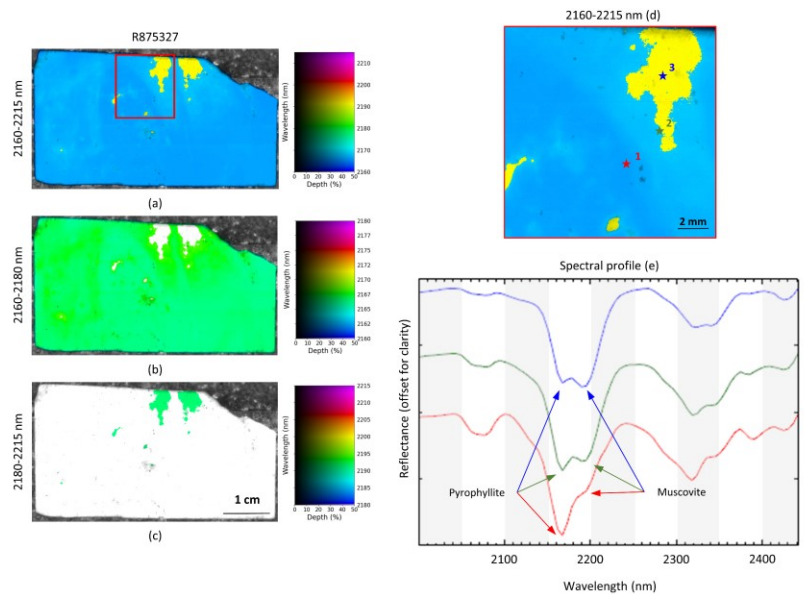


Figure 5.10: Spectral profile with the spectra of the mineralogy overview. Each mineral spectrum was obtained from the samples presented and analysed in the previous paragraphs. Magenta circle indicating the position of the diagnostic feature for topaz at 2083 nm. The green circle indicates the Al-OH absorption feature of muscovite at 2206 nm in the mixed spectra with alunite.

### 5.2.2. Pyrophyllite and muscovite co-occurrence

This sub-section presents the wavelength maps of four samples in which pyrophyllite and muscovite co-occurred. In most of the samples, accessory minerals were observed such as zunyite, alunite and dickite. Since it was previously discussed how this accessory mineralogy was represented in the five primary wavelength maps, here the results focused on the additional and narrower wavelength maps. From the eleven samples in which pyrophyllite and muscovite co-occurred, four samples were defined to present the clearest indication of this co-occurrence (for the remaining seven samples, Appendix VI).

In sample R875327, there was a predominance of pyrophyllite over muscovite (blue over yellow, fig. 5.11a). The 2160-2180 nm map indicated the Al-OH of pyrophyllite at around 2167 nm (green colour, fig. 5.12b). The 2180-2215 nm map indicated the Al-OH of muscovite at around 2189-2195 nm (green colour, fig. 5.12c). In regions with a predominance of pyrophyllite, a small inflection was observed at 2189 nm (spectral curve 1, fig. 5.11.e) indicating a mixture with muscovite. The same situation was verified for muscovite; however, in this case, pyrophyllite presence was more intense with a distinct absorption feature at 2167 nm, rather than an inflection (spectral curve 3, fig. 5.11.e). As observed in maps a and b (Fig. 5.11), as the pyrophyllite occurrence approximated the muscovite occurrence, the Al-OH feature related to pyrophyllite became shallower but within the same wavelength position (same colour, tone variation). Regarding the muscovite occurrence, the absorption feature was slightly deeper at 2189 nm than 2195 nm, displaying an almost flat absorption feature.



*Figure 5.11:* Spectral profile of different regions of the sample R875327 to illustrate the variations in the Al-OH absorption feature where pyrophyllite was dominant (1, panels d and e), at the border of pyrophyllite and muscovite zones (2, panels d and e) and, with a predominance of muscovite (3, panels d and e). Pyrophyllite zones indicated in blue, green and no colour in the 2160-2215 nm (a), 2160-2180 nm (b) and, 2180-2215 nm (c) maps, respectively. Muscovite zones indicated in yellow, no colour and green in the 2160-2215 nm (a), 2160-2180 nm (b) and, 2180-2215 nm (c) maps, respectively. Arrows indicate the position of the Al-OH absorption feature for pyrophyllite and muscovite.

In sample R875367, there was a predominance of muscovite over pyrophyllite (yellow over blue, fig. 5.12a). The 2160-2180 nm map indicated the Al-OH of pyrophyllite at around 2167 nm (green colour, fig. 5.12b). The 2180-2215 nm map indicated the Al-OH of muscovite at around 2189-2195 nm (green colour, fig. 5.12c). In regions with a predominance of muscovite (spectral curve 3, fig. 5.12.e), a small inflection was observed at 2167 nm. In regions with a predominance of pyrophyllite (spectral curve 1, fig. 5.12.e), the muscovite presence was more intense with a distinct feature at 2189-2195 nm. In this sample, a similar situation to the previous sample was observed with a flattening of the deepest part of the Al-OH

absorption feature of muscovite. It was observed that in pyrophyllite regions with the muscovite absorption feature at 2189-2195 nm, the feature was slightly deeper at 2189 nm. However, as closely as it got to the boundary with muscovite regions (spectral curve 2, fig. 5.12.e), the feature tended to be almost flat at 2189-2195 nm. Towards muscovite dominant regions, the feature was slightly deeper at 2195 nm.

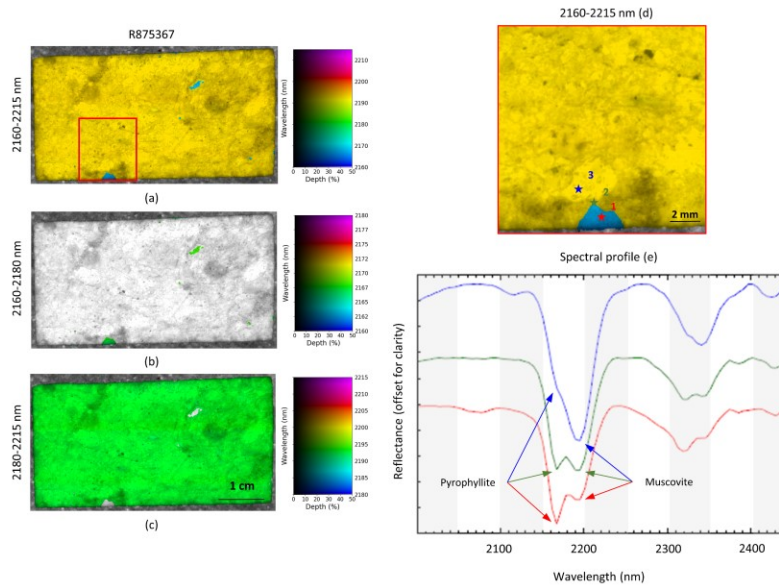


*Figure 5.12:* Spectral profile of different regions of the sample R875367 to illustrate the variations in the Al-OH absorption feature where pyrophyllite was dominant (1, panels d and e), at the border of pyrophyllite and muscovite zones (2, panels d and e) and, with a predominance of muscovite (3, panels d and e). Muscovite zones indicated in yellow, no colour and green in the 2160-2215 nm (a), 2160-2180 nm (b) and, 2180-2215 nm (c) maps, respectively. Pyrophyllite zones indicated in blue, green and no colour in the 2160-2215 nm (a), 2160-2180 nm (b) and, 2180-2215 nm (c) maps, respectively. Arrows indicate the position of the Al-OH absorption feature for pyrophyllite and muscovite.

In sample R875478, there was a predominance of pyrophyllite over muscovite (blue over beige, fig. 5.13.a). The 2160-2180 nm map indicated the Al-OH of pyrophyllite at around 2167 nm (green colour, fig. 5.13b). The 2180-2215 nm map indicated the Al-OH of muscovite at around 2189-2195 nm (green colour, fig. 5.13c). Dickite was observed in association with muscovite (maroon, fig. 5.13a; red, fig. 5.13c) and minor occurrences of topaz (sharp absorption feature at 2083 nm, out of the range of the wavelength maps presented here). In this sample, muscovite was disseminated and occurred along the boundaries or in between pyrophyllite dominant regions. The variation in the wavelength position of the Al-OH absorption feature of muscovite from 2189 to 2195 nm when approximating the boundaries of pyrophyllite-muscovite zones was also verified in this sample (spectral curve 1 to 3, fig. 5.13.e). Also, a similar shift was verified where muscovite was occurring with dickite. In this case, there was a shift of Al-OH absorption feature from 2195 nm to 2200 nm as closer as it got to the dickite dominant region. Iron oxides were also present in this sample (Sepp et al., 2019) and identified as white zones on the inside of the sample.

Lastly, in sample R875524, there was a predominance of muscovite over pyrophyllite (yellow over blue, Fig. 5.14a). The 2160-2180 nm map indicated the Al-OH of pyrophyllite at around 2167 nm (green colour, fig. 5.14b). The 2180-2215 nm map indicated the Al-OH of muscovite at around 2189-2195 nm (green colour, fig. 5.14c). In muscovite predominant zones, there was a small inflection at 2167 nm, likewise sample R875327. In zones with a predominance of pyrophyllite, the muscovite presence was more intense with a distinct absorption feature at 2189-2195 nm. The absorption feature for muscovite was almost flat at 2189-2195 nm in pyrophyllite dominant zones (spectral curve 1, fig. 5.14.e) and more prominent at

2195 nm in muscovite dominant zones (spectral curve 3, fig. 5.14.e). Lower reflectance (dark) observed on the right side of this sample could be related to quartz matrix with a few clasts altered to muscovite.

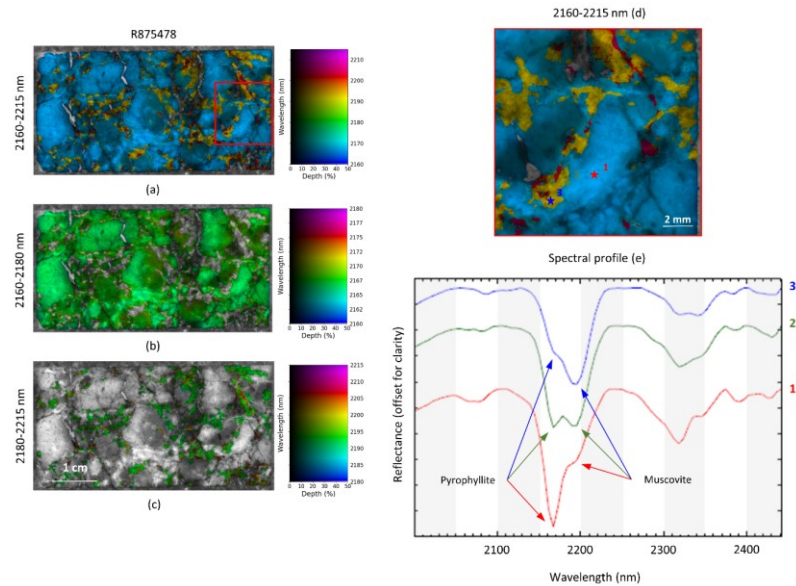


Figure 5.13: Spectral profile of different regions of the sample R875478 to illustrate the variations in the Al-OH absorption feature where pyrophyllite was dominant (1, panels d and e), at the border of pyrophyllite and muscovite zone (2, panels d and e) and, with a predominance of muscovite ( $\pm$  dickite) (3, panels d and e). Pyrophyllite zones indicated in blue, green and no colour in the 2160-2215 nm (a), 2160-2180 nm (b) and, 2180-2215 nm (c) maps, respectively. Muscovite zones indicated in beige, no colour and green in the 2160-2215 nm (a), 2160-2180 nm (b) and, 2180-2215 nm (c) maps, respectively. Dickite zones indicated in maroon, no colour and red in the 2160-2215 nm (a), 2160-2180 nm (b) and, 2180-2215 nm (c) maps, respectively. Arrows indicate the position of the Al-OH absorption feature for pyrophyllite and muscovite. White pixels on the inside area of the sample (a) indicate iron oxide occurrence (Sepp et al., 2019).

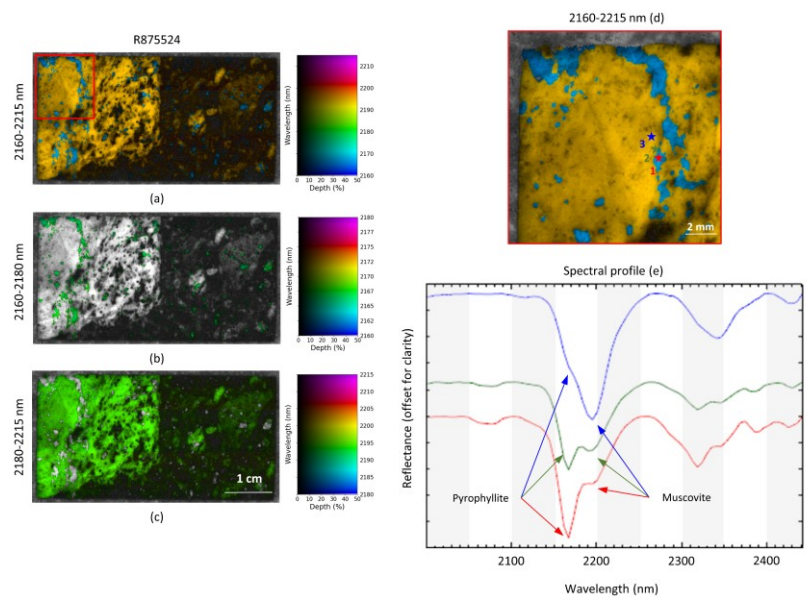


Figure 5.14: Spectral profile of different regions of the sample R875524 to illustrate the variations in the Al-OH absorption feature where pyrophyllite was dominant (1, panels d and e), at the border of pyrophyllite and muscovite zone (2, panels d and e) and, with a predominance of muscovite (3, panels d and e). Pyrophyllite zones indicated in blue, green and no colour in the 2160-2215 nm (a), 2160-2180 nm (b) and, 2180-2215 nm (c) maps, respectively. Muscovite zones indicated in yellow, no colour and green in the 2160-2215 nm (a), 2160-2180 nm (b) and, 2180-2215 nm (c) maps, respectively. Lower reflectance (dark) of the right side could be related to quartz matrix with a few clasts altered to muscovite. Arrows indicate the position of the Al-OH absorption feature for pyrophyllite and muscovite.

The samples presented in this section indicated that at the laboratory Specim resolution (26  $\mu\text{m}$ ), pyrophyllite and muscovite were intimately mixed. Independently of the depth of the absorption features, an inflection at 2167 nm (pyrophyllite) was observed in muscovite dominant zones as well as an inflection at 2189-2195 nm (muscovite) was observed in pyrophyllite dominant zones. However, these inflections were better observed in zones with deeper features. Closer to the contact zones between both minerals, these inflections became more prominent and were displayed as a distinct absorption feature. Also, the wavelength position of the Al-OH absorption feature of muscovite shifted from 2189 to 2195 nm when moving from pyrophyllite dominant zones to muscovite dominant zones. Near the boundary between these zones, there was a flattening of the absorption feature of muscovite.

The additional and narrower wavelength maps also highlighted the textural relationship between pyrophyllite and muscovite. In the four samples presented above, pyrophyllite occurrence varied from disseminated (samples R875327 (Fig. 5.11); R875478 (Fig. 5.13)) to discrete and restricted (samples R875367 (Fig. 5.12); R875524 (Fig. 5.14)). The muscovite occurrence varied from disseminated (samples R875367 (Fig. 5.12); R875524 (Fig. 5.14)) to a preferred path (sample R875478 (Fig. 5.13)) and a discrete occurrence (sample R875327 (Fig. 5.11)).

### 5.2.3. Hydrothermal alteration mineralogy distribution in the study area

The wavelength maps created for all the laboratory Specim data set allowed the definition of mineral associations that could be related to the patterns observed in the airborne ProSpecTIR data. As discussed in section 5.1, the study area was characterised by a central region with a predominance of alunite  $\pm$  pyrophyllite surrounded by a muscovite varying from short (2187 nm) to long-wavelength (> 2211 nm) range. Thus, the mineral association defined for the laboratory Specim data set was divided into two main groups: alunite  $\pm$  pyrophyllite-rich and muscovite-rich.

In fig. 5.15, the mineral association defined for the laboratory Specim data set followed a similar pattern verified in the airborne ProSpecTIR data. Muscovite-rich association of middle (yellow circles, fig. 5.15) to long-wavelength (orange circles, fig. 5.15) range formed a halo around alunite  $\pm$  pyrophyllite-rich associations (blue icons, fig. 5.15). In addition, short-wavelength range muscovite-rich associations (green circles, fig. 5.15) were verified in regions with contact between alunite  $\pm$  pyrophyllite (light cyan, fig. 5.15) and short-wavelength muscovite (green, fig. 5.15) illustrated by the airborne 2150-2250 nm wavelength map (Fig. 5.15).

Lastly, samples with pyrophyllite and muscovite co-occurrence (red star, fig. 5.15), were in the central region of the study area and, always related to contact between alunite  $\pm$  pyrophyllite and a muscovite zone. Most of the samples with pyrophyllite and muscovite co-occurrence were verified in samples with pyrophyllite and muscovite only (blue pentagons, fig. 5.15), aside from accessory minerals like dickite. However, there were samples with pyrophyllite and muscovite co-occurrence which also included alunite (blue triangles, fig. 5.15) and accessory minerals like dickite, zunyite and topaz.

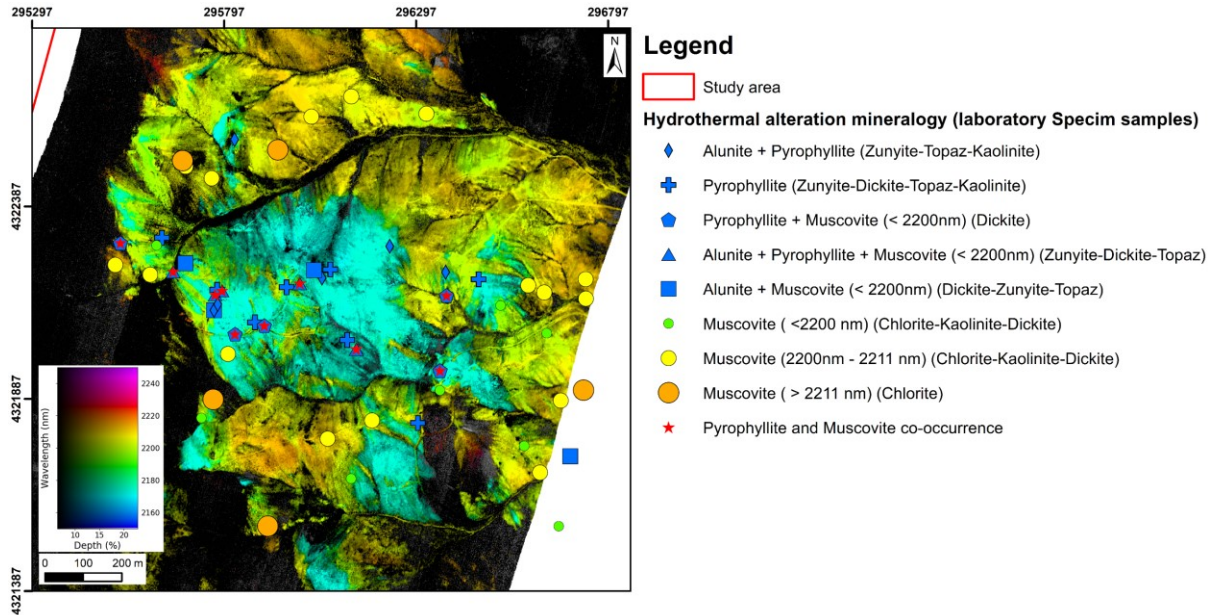


Figure 5.15: Hydrothermal alteration mineralogy distribution over the 2150-2250 nm wavelength map of the study area. Mineral association based on the wavelength maps of the laboratory Specim data set and divided into two main groups: alunite  $\pm$  pyrophyllite-rich (blue icons) and muscovite-rich (green, yellow and orange circles, depending on the wavelength position of Al-OH absorption feature). Red stars indicated samples with pyrophyllite and muscovite co-occurrence.

### 5.3. Spectral index

This section presents the results of the spectral indices developed for the ProSpecTIR and Specim data. To facilitate the display of the data, this section is divided by data set, following the separation previously established. As explained in the methodology chapter, the intervals and the colour scheme selected were the same for both data sets.

#### 5.3.1. ProSpecTIR spectral index

In fig. 5.16, the resulting image of the spectral index and its classified image after the application of the decision tree were displayed, both focusing on the central region study area (for full extent, Appendix VI). As observed, the central region of the study area constituted the region with pyrophyllite predominance, similarly to what was observed with pyrophyllite  $\pm$  alunite zone (light cyan, fig. 5.2 and 5.3). In this central region, there was a variation on the proportion of pyrophyllite as closer as it got to the muscovite dominant zones (from class 90-100% to class 50-60%). Areas with an intense predominance of muscovite (higher than 90%) were observed further away and surrounding this central zone of pyrophyllite  $\pm$  alunite. As observed, there was a clear occurrence of areas with pyrophyllite dominance (class 80-90%) transitioning to areas with muscovite dominance (class 90-100%).

The overlaying of the classified image on the hill shaded DEM of the area displayed an interesting feature regarding the occurrence of pyrophyllite dominant areas. In fig. 5.17, the pyrophyllite occurrence in its highest proportion was normally associated with high altitudes (NE-SW trend).

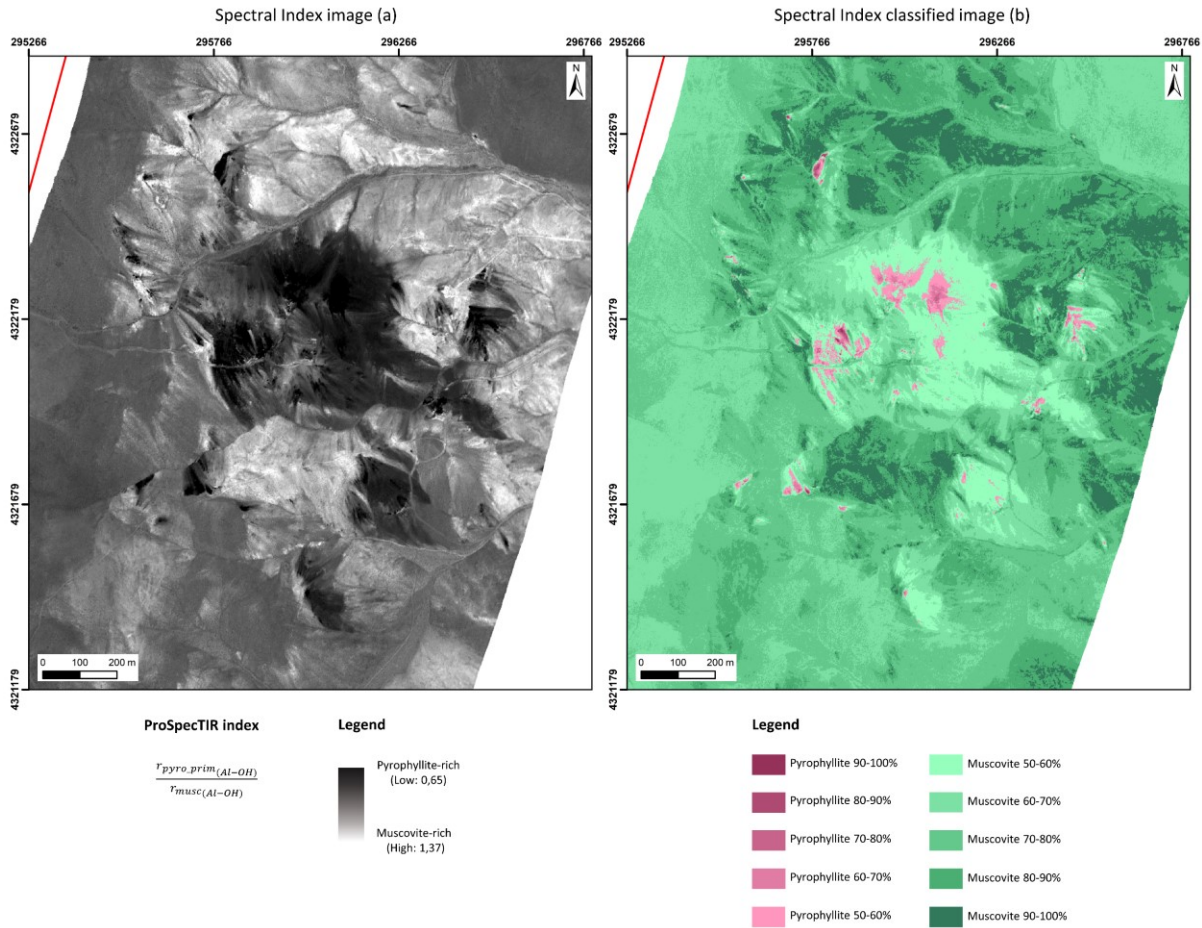


Figure 5.16: Spectral index image (a) and the classified image (b) of the central region of the study area obtained with the decision tree method. Pyrophyllite-rich zones located in the central region, as observed in the wavelength maps (Fig. 5.2-5.3).

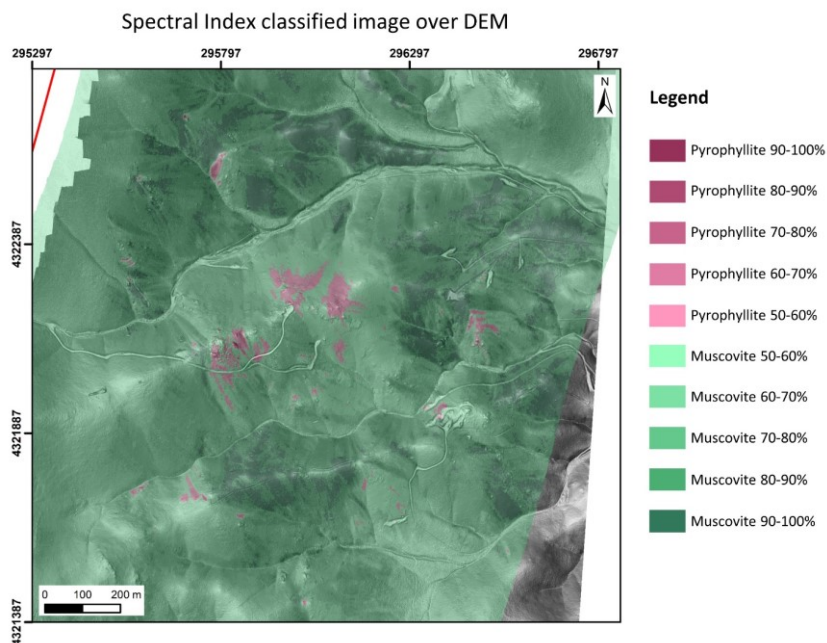


Figure 5.17: Classified image of the spectral index focused on the central region of the study area. By draping the DEM, it was highlighted that pyrophyllite-rich zones were restricted to high altitudes. The dashed pink polygons indicated pyrophyllite-rich zones defined in section 5.1, differentiating them from pyrophyllite ± alunite zones.

The classified image of the spectral index of the ProSpecTIR data allowed the enhancement of the spatial distribution of the pyrophyllite-muscovite association. It was verified through visual inspection of spectral profiles that the middle intervals of the classification (pyrophyllite 50-60% and muscovite 50-60%) did not form two separate absorption features, but a combined feature with distinct influences from both minerals. There are two explanations for this: 1) the spectral resolution of the data, thus not allowing an accurate classification of similar proportions for both minerals. For example, it is not possible to have two clear Al-OH absorption features for pyrophyllite and muscovite, as observed in a transition zone of a Specim sample (Fig. 5.24); 2) the creation of the synthetic mixture for the ProSpecTIR data. The pixels selected as the purest muscovite and the purest pyrophyllite might be a mixed pixel with the predominance of one these minerals. Therefore, the classified image would better indicate pyrophyllite-rich or muscovite-rich zones. Lastly, through the classified image of the spectral index was possible to interpret the same contact zones defined with the use of the 2150-2250 nm wavelength map (Fig. 5.4). Although the intercalary contact zone was less comparable due to the aspects explained above (classification of middle interval proportions), the gradual transition and the abrupt contact were verified in the spectral index image (Fig. 5.18.b).

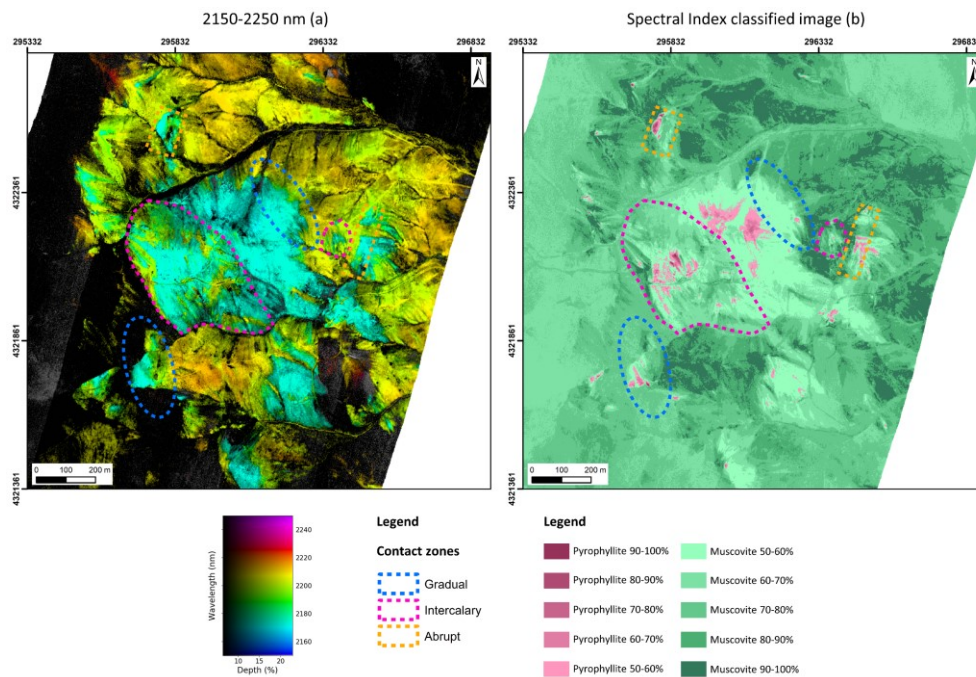


Figure 5.18: Identification of the contact zones defined with the 2150-2250 nm wavelength map (a) in the classified image of the spectral index (b).

The objective of creating a spectral index for airborne ProSpecTIR data was to highlight the relative proportion of pyrophyllite and muscovite, thus assisting in mapping the contact zones between both minerals. Although the spectral index allowed the classification of pyrophyllite and muscovite-rich zones, the transition zones between both minerals could be wrongly classified by the presence of alunite. To overcome this obstacle, the spectral index could include in its equation the calculation of the depth sulphate absorption feature at around 1760 nm, present in alunite but not in pyrophyllite or muscovite. Thus, it would be able to identify zones with a shallow feature at around 1760 nm and classify it properly as either a pyrophyllite or muscovite zone. However, this step was performed by comparing the 1650-1850 nm and the 2150-2250 nm maps (Fig. 5.3) to identify pyrophyllite-rich zones with minor alunite.

Therefore, although wavelength maps would not indicate the relative proportion of pyrophyllite and muscovite, more robust and detailed information could be obtained from these maps when compared to the outcome generated by the spectral index of the airborne ProSpecTIR data.

### 5.3.2. Specim spectral indices

This section presents the results of the spectral indices and classified images of the samples presented in section 5.2.2. Following the same procedure as for the section of the laboratory Specim wavelength maps, this sub-section was divided into samples with a mineralogy overview and samples with a pyrophyllite and muscovite co-occurrence. This research opted to present samples with additional mineralogy (alunite, zunyite, dickite) to display the patterns presented by these minerals when the indices were applied, facilitating the interpretation of the results.

As detailed in the methodology section, the spectral index (1) is the additional spectral index developed for the laboratory Specim data set and the spectral index (2) is the same index developed for the airborne ProSpecTIR data set.

#### 5.3.2.1. Mineralogy overview

In sample R875389, there were no substantial differences between the classified images of the spectral indices (1) (Fig. 5.19.1a) and (2) (Fig. 5.19.1b). As observed in fig. 5.19, the sample was muscovite-rich and had a predominance of muscovite varying from 80-100%, according to the values established in the synthetic mixture.

In sample R875431, the classified image of the spectral index (1) (Fig. 5.19.2a) indicated the presence of muscovite, even though it was a pyrophyllite-rich ( $\pm$  topaz) sample. In the spectral curve of this region, there was no indication of muscovite occurrence, and it presented pixels with very low reflectance values ( $< 20\%$ ). Due to the presence of topaz, the spectral index (1) was influenced by the absorption feature at 2083 nm (Fig. 5.19.2b).

In sample R875382, with a predominance of pyrophyllite and minor occurrences of dickite, it was observed that dickite was characterised as muscovite in both spectral indices (Fig. 5.19.1c-2c). The centre zone of dickite occurrence had different classes owing to the depth of the second absorption feature at 2206 nm. The spectral index (1) underestimated the proportion of pyrophyllite in comparison to the spectral index (2). It was the opposite situation of the previous sample since the feature at 2066-2078 nm was shallower due to a smaller occurrence of topaz.

In sample 664b, an influence of alunite and zunyite on the spectral indices was observed. For both minerals, its classification varied according to the spectral index. In the spectral index (1) (Fig. 5.19.1d), alunite was classified both as pyrophyllite and muscovite-rich. It was observed that when alunite had shallower absorption features at 2167-2172 nm, pixels were classified as muscovite-rich. Deeper absorption features led the classification towards pyrophyllite-rich zones. Zunyite was classified as muscovite-rich, because of the depth of the feature at 2066-2078 nm. Since zunyite presents a long and deep slope from 2065-2185 nm, this feature overestimated a pixel with no presence of pyrophyllite. Dickite, similarly to the previous sample, was classified as a muscovite-rich zone.

In the spectral index (2) (Fig. 5.19.2d), alunite was classified as a pyrophyllite-rich zone with the proportion varying according to the depth of the feature at 2167-2172 nm. Deeper absorption features were classified as been a pyrophyllite with a higher proportion in comparison to shallower absorption features. Zunyite was also classified as pyrophyllite-rich since it presents the second deepest absorption feature at 2161-2167 nm, and the feature at 2065-2185 nm was not considered in this index. Lastly, dickite was defined as a muscovite-rich zone.

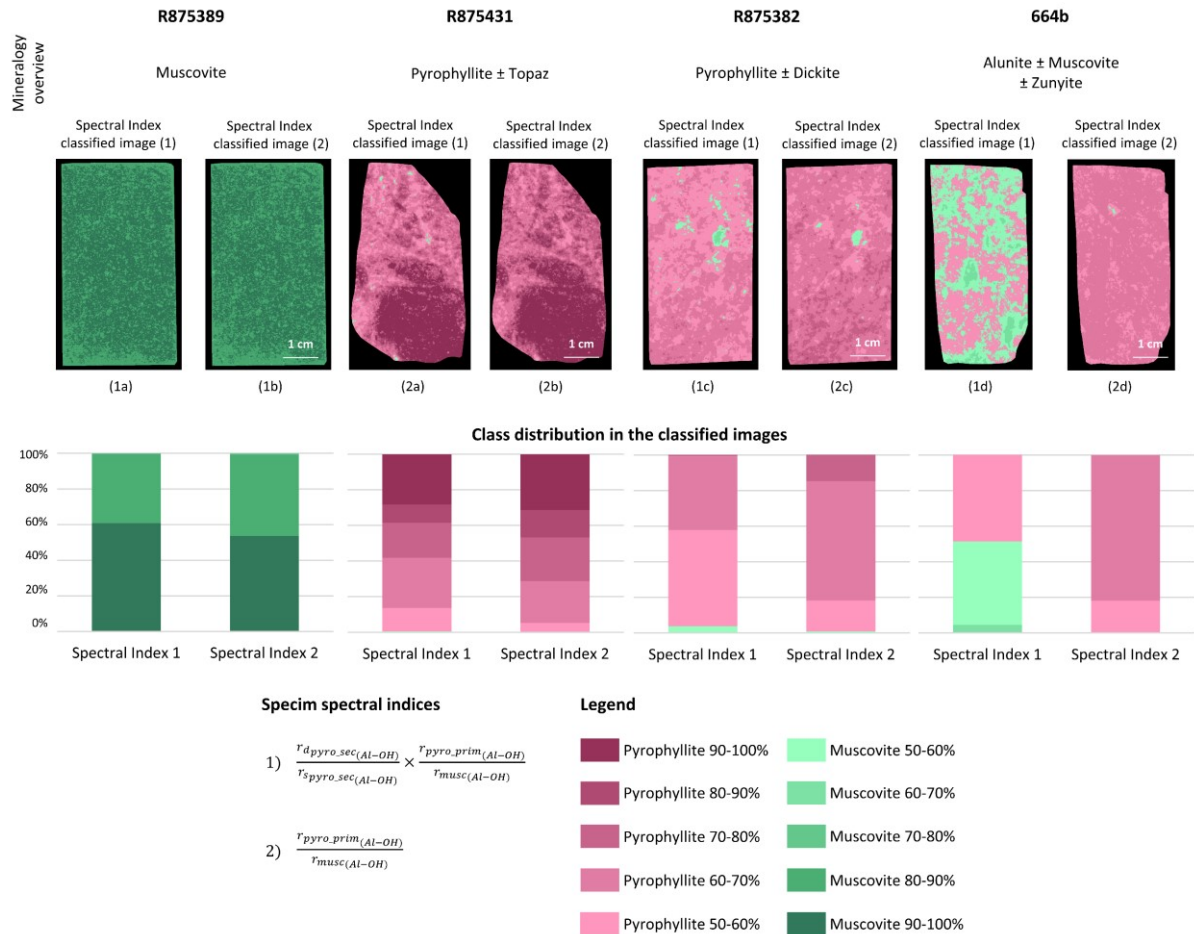


Figure 5.19: Classified images of the spectral indices to characterise the mineralogy overview and how it was represented in this method. Class distribution to indicate the variation of the relative proportion of the minerals present in each sample regarding the spectral index. In subfigure (2a), few pixels (< 1%) were classified as muscovite 50-60%. Although this class was not clearly observed in the class distribution graphic, it was included.

### 5.3.2.2. Pyrophyllite and muscovite co-occurrence

In sample R875327, the predominance of pyrophyllite over muscovite was observed in both indices (fig. 5.20). In the spectral index (1) (Fig. 5.20.1a) pyrophyllite areas of class 90-100% were relatively smaller when compared to the same class in the spectral index (2) (Fig. 5.20.1b). On the other hand, muscovite-rich zones were smaller in the spectral index (2) in both classes displayed in those images (class 50-60% and 60-70%) (Fig. 5.20.1c). Despite these variations, a transition from areas with pyrophyllite predominance (90-100% to 50-60%) to muscovite predominance was observed. This change was also verified in the wavelength maps presented previously with the tone variation (different proportions within the same mineral) and colour variation (different mineral predominance).

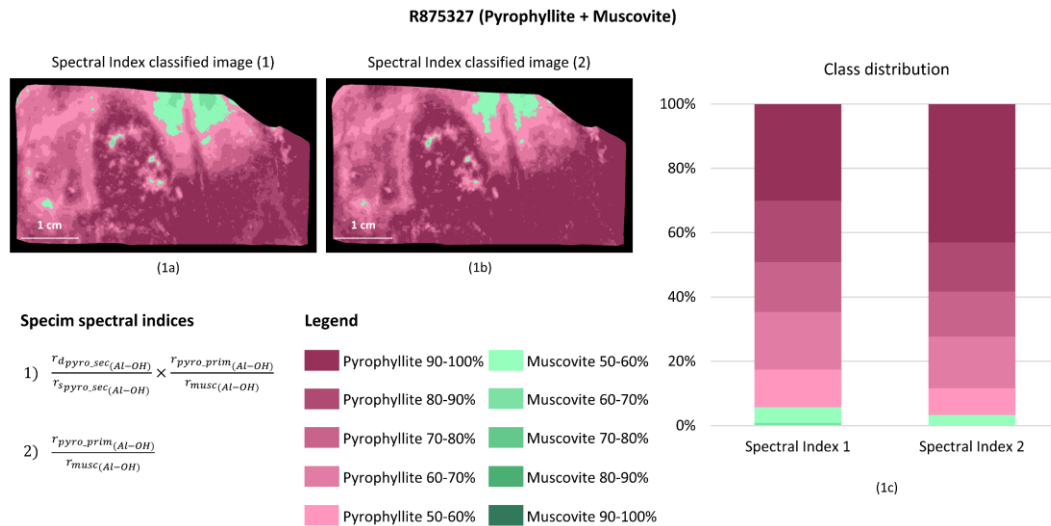


Figure 5.20: Comparison of the results obtained through both spectral indices for the sample R875327.

In sample R875367, the predominance of muscovite over pyrophyllite was verified in both indices (figure 5.21). The spectral index (1) (Fig. 5.21.1a) presented smaller occurrences of pyrophyllite-rich areas in comparison to the spectral index (2) (Fig. 5.21.1b). Through a visual comparison with the 2150–2250 nm wavelength map of the sample (Fig. 5.6.R875367b), both indices underestimated the occurrence of pyrophyllite. Also, in the spectral index (1), muscovite-rich areas of class 70–80% were overestimated in comparison to the spectral index (2).

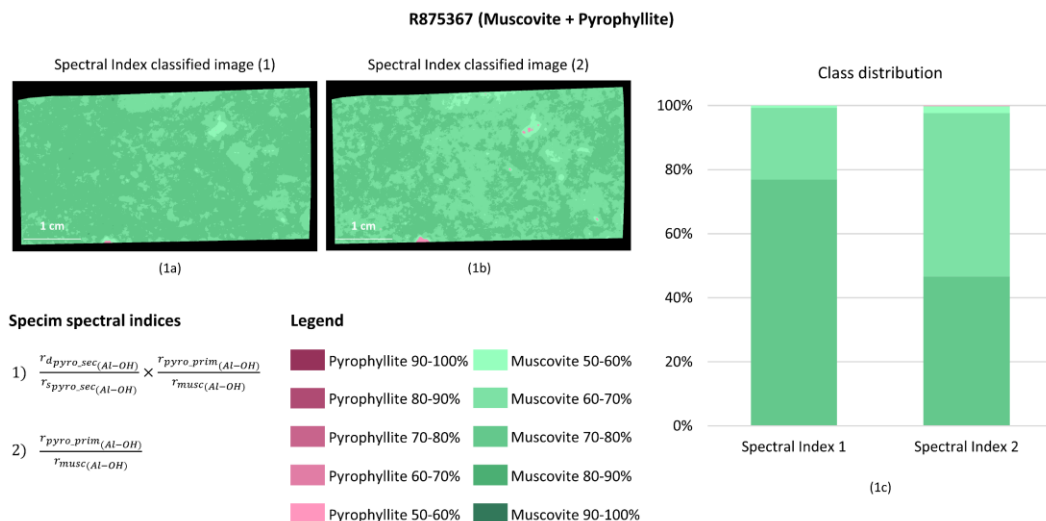


Figure 5.21: Comparison of the results obtained through both spectral indices for the sample R875367.

In sample R875478, the predominance of pyrophyllite over muscovite was better observed in the spectral index (2) (Fig. 5.22.1b); meanwhile the spectral index (1) (Fig. 5.22.2a) displayed more extensive muscovite-rich zones. Also, pyrophyllite-rich areas with a high proportion (class 80–90% and 90–100%) were more extensive in the spectral index (2) than in the spectral index (1). As observed in previous samples, dickite was classified as muscovite-rich of a lower proportion (class 50–60%). Regarding the occurrence of muscovite displayed in the wavelength maps (dispersed and between boundaries of pyrophyllite-rich zones), it was also observed in the spectral index (2). Since the spectral index (1) presented more extensive muscovite-rich zones, these patterns were not highlighted. Lastly, the black/unclassified pixels inside the sample were iron oxide occurrences mentioned in section 5.2.2. These pixels were masked to not interfere in the spectral index calculation.

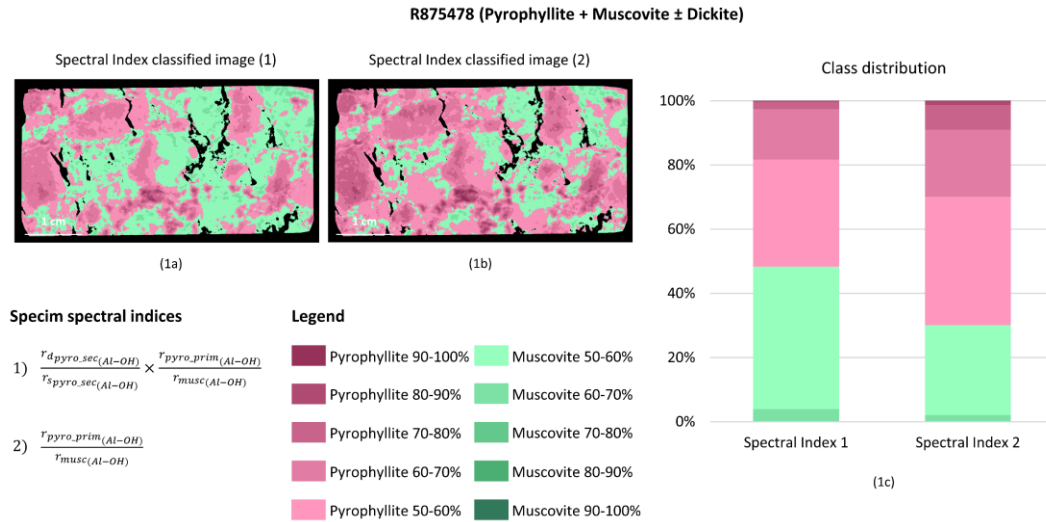


Figure 5.22: Comparison of the results obtained through both spectral indices for the sample R875478. The black pixels inside the sample were iron oxide occurrences. These pixels were masked to not interfere in the spectral index calculation.

Lastly, in sample R875524, the predominance of muscovite was observed in both indices, and there were minor differences between them (figure 5.23). For the spectral index (1) (Fig. 5.23.1a), the pyrophyllite-rich areas were smaller in comparison to the spectral index (2) (Fig. 5.23.1b). Consequently, pyrophyllite-rich areas of higher proportion (class 60-70% and 70-80%) were also reduced. In addition, the overall texture observed in the wavelength maps was preserved in both indices.

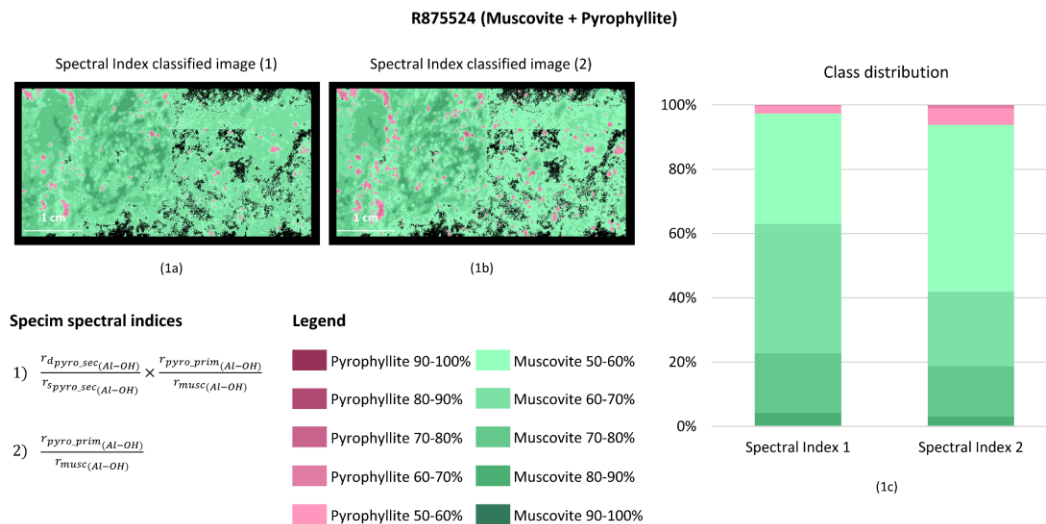


Figure 5.23: Comparison of the results obtained through both spectral indices for the sample R875524. The black pixels inside the sample represented noise in the spectral curve (flat spectra with descending reflectance values from 1100 nm to 2400 nm). Thus, these pixels were masked to not interfere in the spectral index calculation.

The purpose of creating an additional spectral index for the laboratory Specim data set (spectral index (1)) was to complement the spectral index developed for the airborne ProSpecTIR data set (spectral index (2)) and reduce the interference of other minerals like zunyite, topaz and alunite. However, the results of the spectral index (1) over- and under-represented the relative proportions depending on the shape of the spectral curve at the 2066-2078 nm range. The ratio of the primary diagnostic Al-OH absorption feature for pyrophyllite (2167 nm) and muscovite (2180-2228 nm) would already be an indication of the relative proportion of these two minerals. Instead of assisting in the distinction of both, multiplying it with the 2066-2078 nm ratio added uncertainty to the final image. As an example, a shallow feature at this

secondary Al-OH absorption feature enhanced areas of the sample which had a 50:50 proportion of pyrophyllite and muscovite, shifting this proportion to a muscovite predominance. In fig. 5.24, this scenario was illustrated with both classified images at the same position and the associated spectral profile. In pixels classified as muscovite-rich by the spectral index (1) (position 1, figure 5.24.2a), the spectral profile indicated a predominance of pyrophyllite with a slightly deeper absorption feature at 2167 nm. The spectral index (2) (Fig. 5.24.2b) classified the same pixels as a pyrophyllite-rich. In the spectral profile (Fig. 5.24.c), this zone of the sample presented a shallow absorption feature at the 2066-2078 nm range.

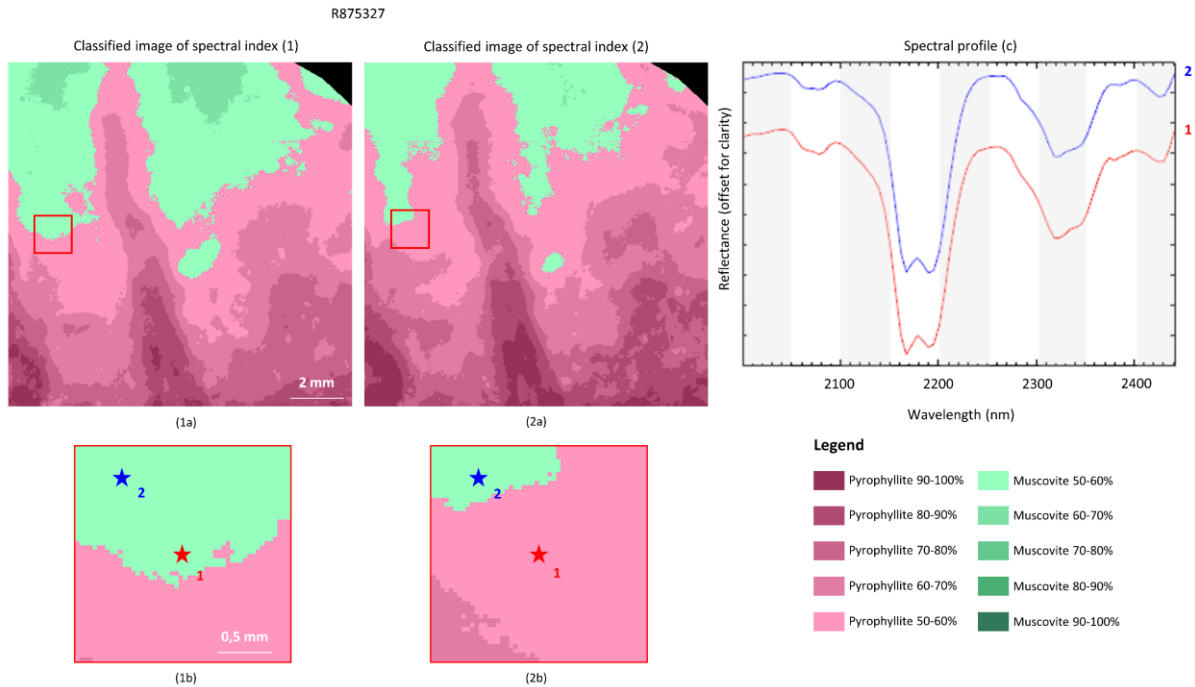


Figure 5.24: Example of the overestimation of muscovite-rich zones in a classified image of the spectral index (1) in a sample with a shallow absorption feature at 2066-2078 nm.

Thus, the textural relationship of pyrophyllite and muscovite was affected in the spectral index (1). By analysing only, the primary diagnostic Al-OH absorption feature (the spectral index (2)), there was no interference of either zunyite or topaz. Regarding alunite, if this mineral occurrence is discrete, then the 1650-1850 nm wavelength map could assist in its identification due to the diagnostic absorption feature at 1760 nm. A similar approach to the one developed for the airborne ProSpecTIR data and the identification of pyrophyllite dominant regions (figure 5.3, section 5.1). Still, if alunite occurrence is disseminated in the sample along with pyrophyllite and muscovite, neither indices should be used as an indicator of the relative proportion or textural relationship of pyrophyllite and muscovite.

## 6. BUCKSKIN RANGE, AN EPITHERMAL SYSTEM

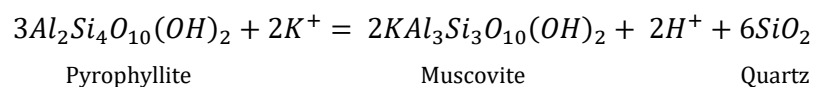
### 6.1. Introduction

Epithermal deposits are formed in shallow regions of a magmatic-hydrothermal system with a predominance of acid hydrothermal fluids, an intense flux of magmatic liquid and vapour containing H<sub>2</sub>O, CO<sub>2</sub>, HCl, H<sub>2</sub>S, and SO<sub>2</sub>, with an input of local meteoric water. The relatively short path that magmatic fluids follow from the intrusion to the epithermal environment generates a minimum water-rock interaction (in comparison to the epithermal environment formed in geothermal systems, Appendix VIII). Hydrothermal fluids and water-rock interaction are critical factors for the generation of epithermal deposits. Both factors control the pH, oxidation and sulfidation of the hydrothermal fluids (Simmons et al., 2005).

High sulfidation epithermal systems are characterised by the ascension of low pH high-temperature magmatic-hydrothermally derived fluids. The intense acid leaching caused by this fluid is responsible for the generation of lithocaps, large domains of silicic, advanced argillic and argillic alteration hosted above the subvolcanic intrusive environment (Cooke et al., 2017; Sillitoe, 1995; Sillitoe & Hedenquist, 2003; Simmons et al., 2005). Lithocaps may host high sulfidation epithermal Au-Ag ± base metal deposits which are defined by scattered quartz-alunite ± alumino-silicate clay (pyrophyllite, dickite, kaolinite and, diaspore) wall rock alteration (Sepp et al., 2019). This shows the importance of lithocaps in high sulfidation epithermal systems for the mineral exploration industry.

During the formation of the lithocaps, the generation of the advanced argillic alteration (acid leaching) is defined by minerals originated at temperatures higher than 200°C as pyrophyllite, dickite, diaspore, topaz, and alunite. The presence of alunite, which is normally formed at a pH of 2 or 3, corroborate the percolation of an acidic fluid (Sillitoe & Hedenquist, 2003). The acidic solution is then neutralised by hydrolytic alteration of alumino-silicates minerals which are responsible for a sharp outward zoning alteration pattern (Appendix IX). Besides, this intense acid leaching associated with vuggy quartz generation from the interaction with host rock is responsible for developing a permeable zone in the lithocaps. These zones work as channels for late-stage metal-bearing fluids of near-neutral pH and lower salinity, an indication of a lower sulfidation stage. This stage is characterised by a mineral assemblage of K-mica and K-feldspar that would increase the pH and, iron-bearing minerals which would change the oxidation stage (Simmons et al., 2005; Williams-Jones & Heinrich, 2005).

The changes in the fluid chemistry are, apparently, crucial for improving gold transport into the epithermal setting. This improvement is possible because the late-stage fluid contains chloride complex capable of transporting alkalis and trace metals. Besides, it may convert pyrophyllite and dickite into muscovite or topaz into zunyite. A reverse situation of pyrophyllite replacing muscovite like documented in El Salvador, Chile (Watanabe & Hedenquist, 2001) and Oyu Tolgoi, Mongolia (Khashgerel et al., 2009) could be related to the cyclic nature of magmatic-hydrothermal systems (Rottier et al., 2018; Sepp et al., 2019). The replacement of pyrophyllite by muscovite can be expressed by the following reaction, corroborating the suggestion that the late-stage fluids are near-neutral pH and able to transport alkalis and trace metals (Sepp et al., 2019):



The high sulfidation epithermal system described for the Buckskin range in the previous paragraphs (also documented by (Fagbohun, 2015; Lipske & Dilles, 2000; Sepp et al., 2019)) is characterised by aspects verified by this research and discussed below:

## 6.2. Hydrothermal alteration mineralogy (alteration zones)

The use of wavelength maps on the laboratory Specim data improved the hydrothermal alteration mineralogy characterisation. Mineral assemblages typical of an advanced argillic alteration (acid leaching) were identified such as alunite, pyrophyllite, dickite and topaz. Hydrothermal mineral assemblage linked to the sericitic alteration was characterised by minerals like muscovite and zunyite. The additional and narrower wavelength maps defined for the Specim samples facilitate the identification of samples with co-occurring pyrophyllite and muscovite. As observed in fig. 6.1, both mineral assemblages identified in this research were in accordance with the alteration zones mapped by Lipske (2002). Although muscovite is linked to a different hydrothermal alteration fluid than pyrophyllite, this research opted to merge both minerals in one assemblage (blue pentagon, fig. 6.1-2) to highlight the occurrence of both minerals along contact zones between advanced argillic and sericitic alteration. The co-occurrence and the overprinting pattern of both minerals are discussed in the last part of this section.

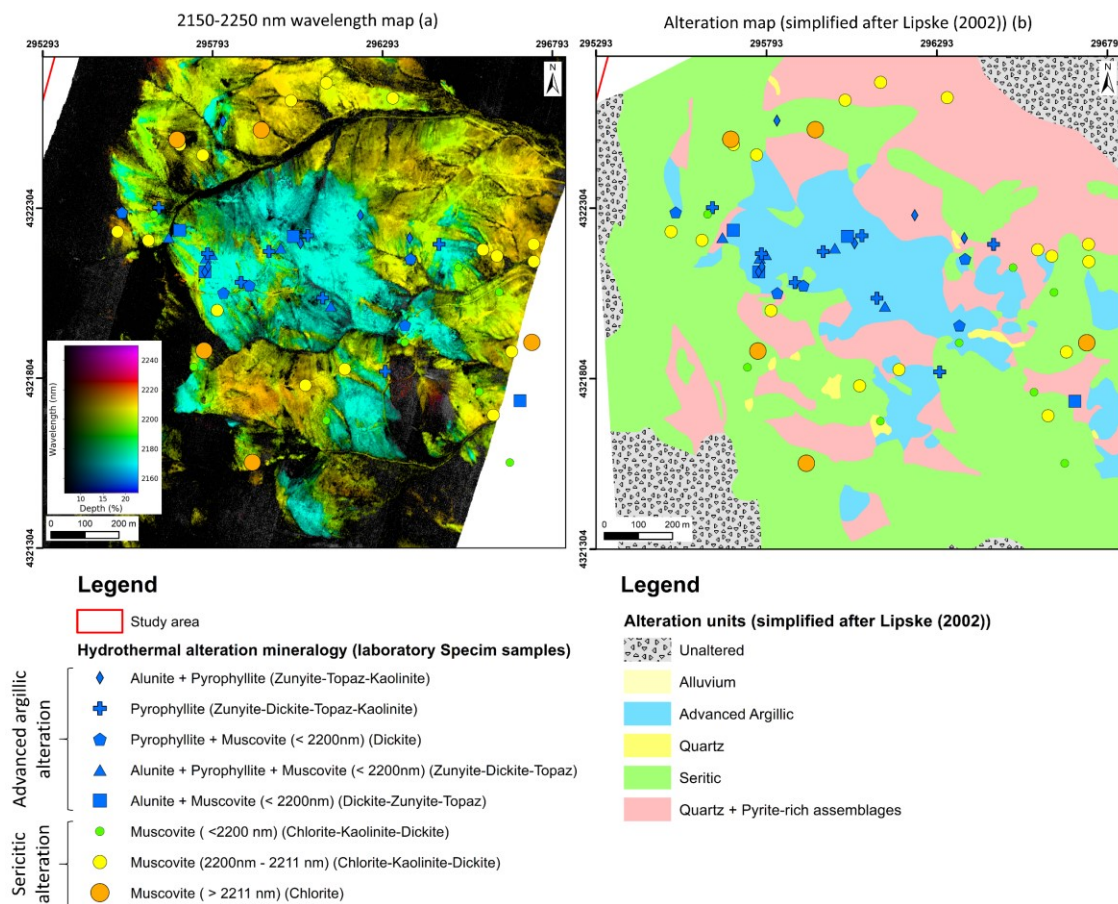


Figure 6.1: Comparison of the hydrothermal alteration assemblage identified from the laboratory Specim data set with the simplified alteration map developed by Lipske (2002). In subfigure (a), the 2150-2250 nm wavelength map was added to the background to highlight the patterns regarding the alunite ± pyrophyllite (light cyan) and muscovite ± pyrophyllite (green, yellow, and orange) zones.

Like the discussion by Simmons et al. (2005) which was previously mentioned, an outward zoning alteration pattern through the airborne ProSpecTIR wavelength maps was identified and characterised. An inner zone characterised by an alunite ± pyrophyllite occurrence in contact with a surrounding muscovite-dominant assemblage. This pattern was verified by Lipske (2002) and Fagbohun (2015). In fig. 6.2, the airborne wavelength map and mineral assemblages identified by this research were displayed over the alteration assemblages map defined by Fagbohun (2015). The envelopment of the sericitic alteration over the advanced argillic alteration was verified in both maps and corroborated by the assemblages derived from the laboratory Specim data.

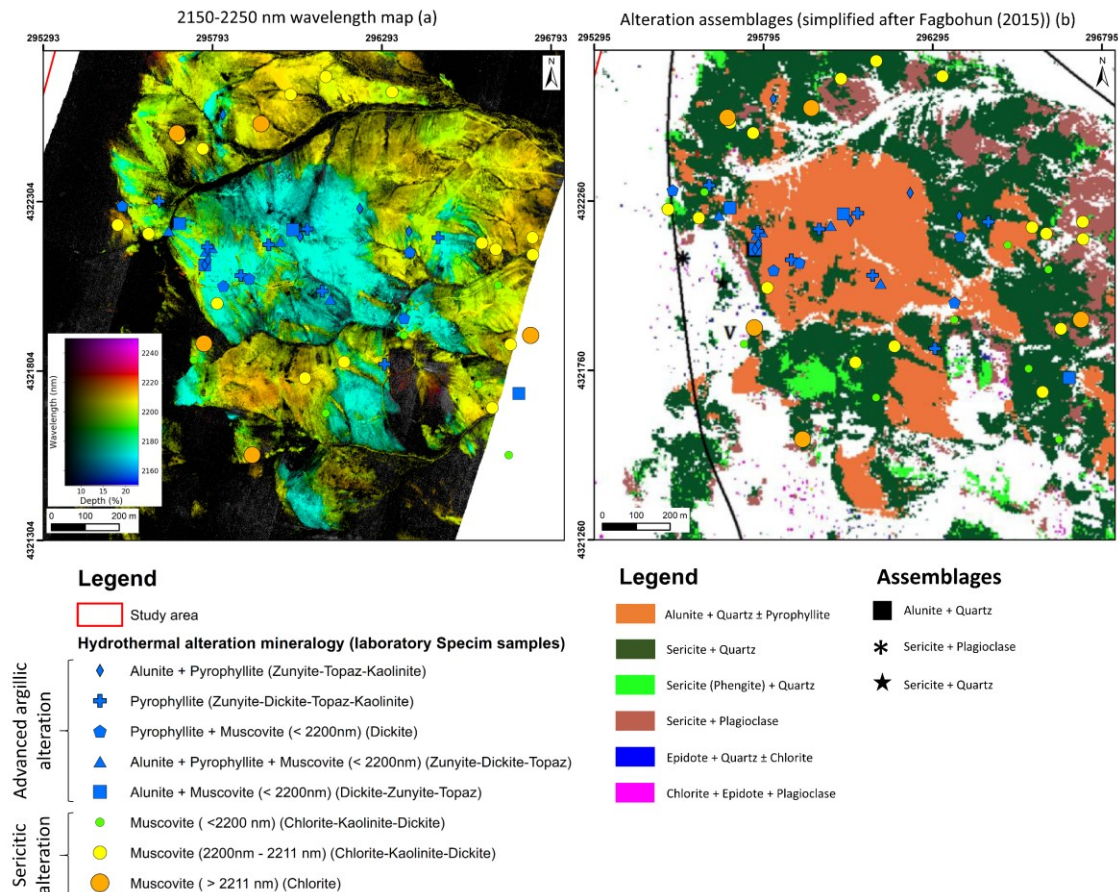


Figure 6.2: Comparison of the alteration zoning pattern identified by this research with an airborne remote sensing alteration assemblage map developed by Fagbohun (2015) by combining SEBASS data and ProSpecTIR 4 m spatial resolution data.

### 6.3. Pyrophyllite-Muscovite distribution

By combining airborne wavelength maps in different ranges and the classified images of the spectral index, areas of pyrophyllite predominance (minimum alunite) were mapped facilitating the identification of contact zones of pyrophyllite and muscovite dominant parts (Appendix X). Although the DEM suggested that pyrophyllite-rich areas were associated with high elevation in the study area (Fig. 5.17), a direct relationship between its occurrence and topography should be carefully addressed due to: 1) the conditions of pyrophyllite formation ( $250^{\circ}\text{C} < T < 300^{\circ}\text{C}$ ); 2) considering paleo geothermal gradient of the study area, a lithocap thickness of, approximately, 600-800 m would be required (Michael Sepp, unpublished work); 3) a lack of marker bed stratigraphy as a result of a tectonic setting based on east-dipping normal faults and tilting process of  $60^{\circ}$  to  $90^{\circ}$  W (Dilles & Einaudi, 1992; Dilles et al., 2000; Proffett, 1977). Nevertheless, preliminary geological cross-sections of the central study area would suggest a positive topographical feature for some areas of pyrophyllite-rich zones post-hydrothermal alteration events (Michael Sepp, unpublished work). Also, since pyrophyllite occurrence is associated with quartz-alunite assemblages (Lipske & Dilles, 2000), these zones could be more resistant to a weathering process, thus resulting in a positive topographical feature.

Therefore, unlike in other deposits where overprinting patterns were identified (El Salvador, Chile (Watanabe & Hedenquist, 2001); Oyu Tolgoi, Mongolia (Khashgerel et al., 2009)), an association of pyrophyllite and topography in Buckskin range still requires more information (detailed geological cross-section) to be better interpreted.

#### 6.4. Overprinting at the laboratory scale

Pirajno (2009) discussed that hydrothermal alteration styles could be divided into pervasive, selectively pervasive, and non-pervasive. Pervasive alteration is characterised by a partial or total obliteration of the original rock texture, with a replacement of most of the rock-forming minerals. Selectively pervasive alteration is defined by a replacement of certain original minerals. Lastly, non-pervasive alteration is described as the replacement of only a small part of the rock volume.

To this classification, the veinlet-controlled style could also be added. Although the emplacement of hydrothermal alteration fluids through veins or fractures could result in a pervasive or selectively pervasive alteration, this research opted to differentiate the vein-type since it could generate diagnostic alteration textures (Fig. 6.3).

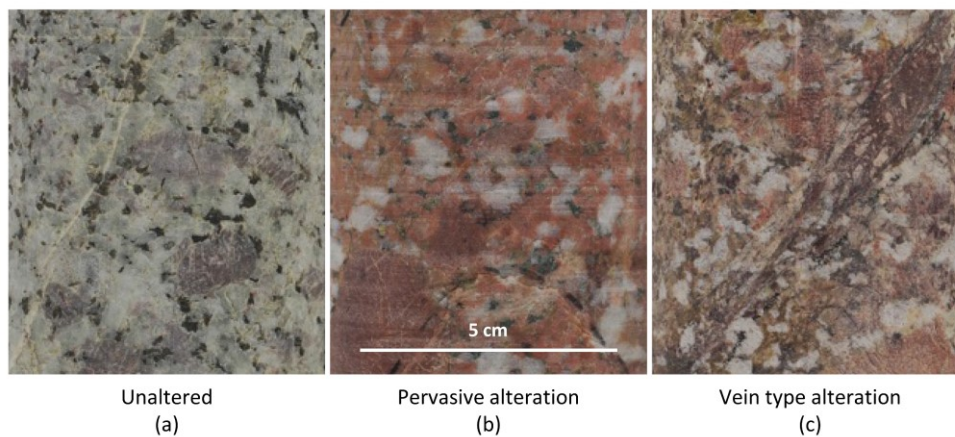


Figure 6.3: Representation of an unaltered rock (a), pervasively altered rock (b) and, a vein-type altered rock (Meller & Kohl, 2014).

Taylor (2009), from a mineral deposit context, defined the overprinting or replacement pattern as the textural information which can be used to understand the temporal relationship between two or a group of minerals. As discussed in chapter 2, the study area is characterised by an intense hydrothermal alteration process with primary textures being obliterated by advanced argillic and sericitic alteration (Lipske & Dilles, 2000). Therefore, identifying pervasive or selectively pervasive alteration textures in samples where pyrophyllite and muscovite were both presents was the first step to characterise overprint patterns. The second step was the identification of the shift in the wavelength position of the Al-OH absorption feature of muscovite.

The wavelength maps and classified images of the samples indicated that the co-occurrence of pyrophyllite and muscovite happened in samples which were pyrophyllite-rich or muscovite-rich. In addition to the use of a spectral index, the 0-50% depth stretch in the wavelength maps was a crucial aspect in recognizing the occurrence of both minerals, as presented in section 5.2. For this reason, only 0-50% depth stretch wavelength maps were selected for this discussion.

In the wavelength maps and spectral indices images, pyrophyllite and muscovite occurred as discrete zones, where one of the minerals was dominant in the sample. In sample R875327 (Fig. 6.4.1a-b), two interpretations were possible: pervasive alteration of pyrophyllite-rich assemblage obliterating the muscovite-rich assemblage; or a selectively pervasive alteration of muscovite-rich assemblage replacing part of the pyrophyllite-rich zones (top central part, fig 6.4.1a-b). Samples R875367 (Fig. 6.4.2a-b) and R875524 (Fig. 6.4.3a-b) could be characterised by a pervasive texture where muscovite-rich assemblage obliterated most of the pyrophyllite-rich assemblage. As observed, in these two samples, muscovite-rich zones are enveloping most of the pyrophyllite-rich zones.

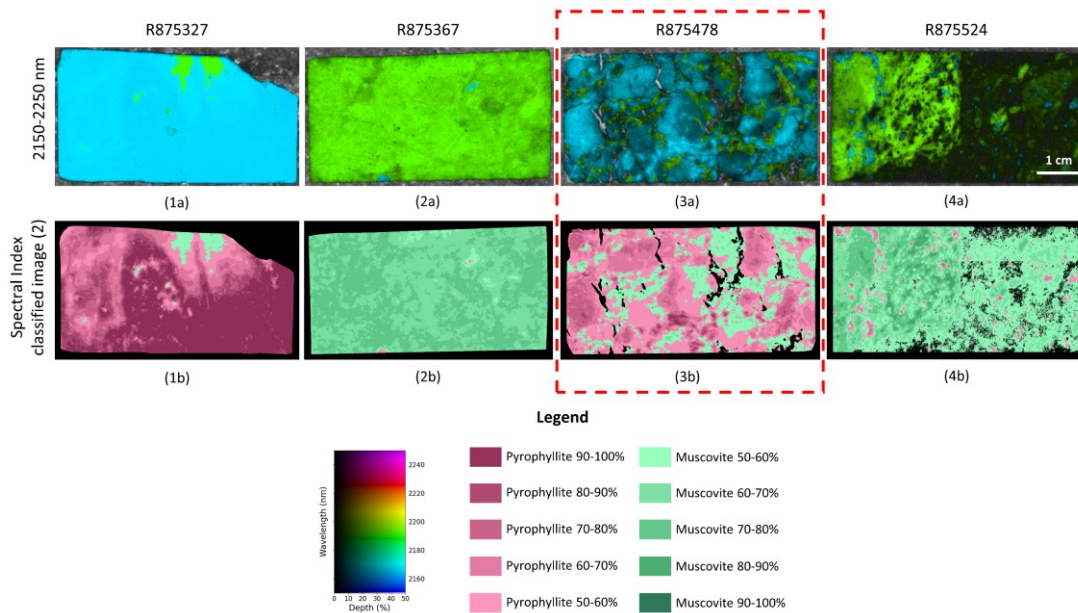


Figure 6.4: 2150-2250 nm wavelength maps (0-50% depth stretch) and classified images of the spectral index (2) of four samples with pyrophyllite and muscovite co-occurrence.

The only exception for the discrete occurrence was observed in the sample R875478 in which muscovite occurrence was pervasively disseminated in the sample, following a preferred direction in between the pyrophyllite-rich zones (Fig. 6.4-6.5). In fig. 6.5, a schematic representation of the textural pattern in sample R875478 was generated to highlight the interpretation of muscovite being disseminated in the sample. This sample could be characterised by a combination of veinlet-controlled and pervasive alteration of a muscovite-rich assemblage over a pyrophyllite-rich assemblage. The iron oxide occurrences (unclassified/black pixels, fig 6.5b) also reinforce the interpretation of a veinlet-controlled texture as they appeared to follow a preferred direction as well.

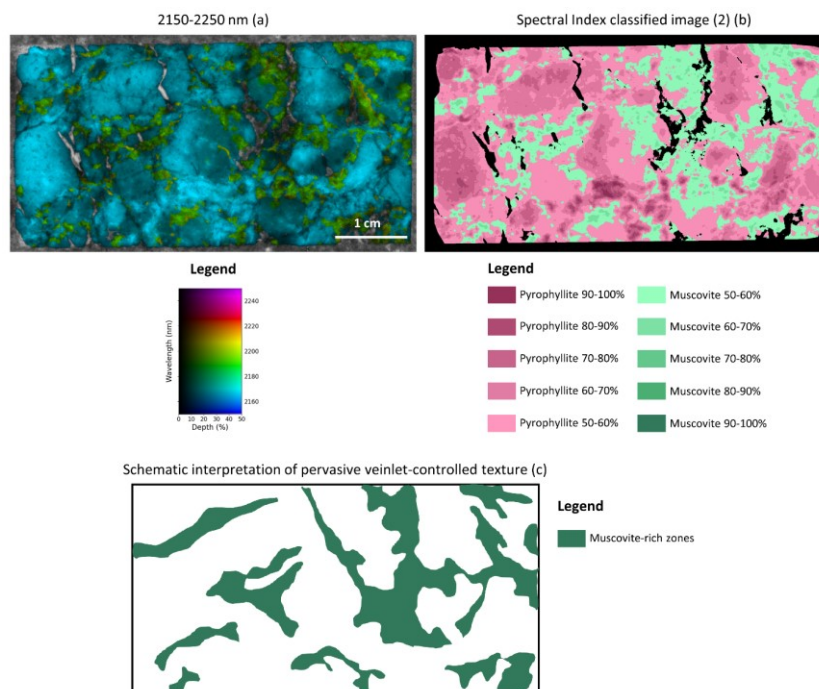


Figure 6.5: 2150-2250 nm wavelength map (a), the classified image of the spectral index (2) (b) and a schematic representation of veinlet-controlled and pervasive alteration of this sample. Interpretation based on both wavelength map and classified image.

As previously discussed, most of the samples were interpreted as muscovite-rich assemblages overprinting pyrophyllite-rich assemblages due to the textural relationship of both minerals. Still, only sample R87478 presented clear overprinting patterns of muscovite over pyrophyllite. Thus, the identification of the shift in the wavelength position of the Al-OH absorption feature of muscovite was defined as the second step to the characterisation of overprinting patterns.

As described in the results section, in all samples where pyrophyllite and muscovite co-occurred and had a common boundary, this shift was detected near the boundaries of both minerals. To facilitate the visualization of this shift, a new classified image was created over the transition classes (Pyrophyllite 60-50% to Muscovite 50-60%) of the classified images of the spectral index (2). As observed in fig. 6.6, the wavelength position of the absorption feature varied from 2189 nm in pyrophyllite-rich zones (as the second deepest absorption feature, since the first was at 2167 nm) (yellow zones, fig. 6.6.1-3c) to an absorption feature at 2189-2195 nm close to the boundaries between pyrophyllite and muscovite-rich zones (near the dashed red line, figure 6.6). In some samples, close to these boundaries, there was a flattening of the 2189-2195 nm absorption feature, although this was not captured by the classified pixels. In muscovite-rich zones where the Al-OH absorption feature of muscovite was the deepest absorption feature, the wavelength position shifted to 2195 nm (blue zones, fig. 6.6.1-3c).

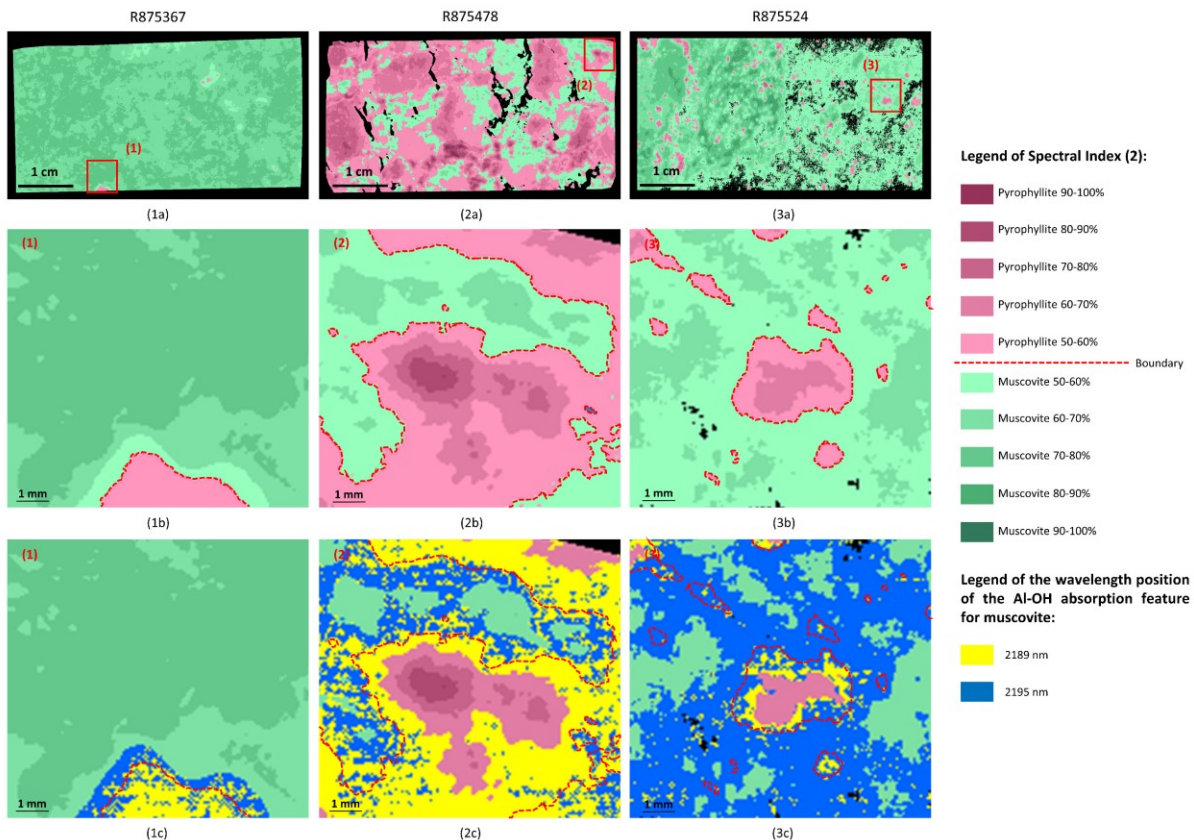


Figure 6.6: Representation of the shift of the wavelength position of the Al-OH absorption feature of muscovite in boundaries between pyrophyllite-rich and muscovite-rich zones. In most cases, pyrophyllite-rich zones have the second deepest absorption feature at 2189 nm. Muscovite-rich zones have the deepest absorption feature at 2195 nm varying to 2189 nm when closer to the boundary.

The shift of the wavelength position of the Al-OH absorption feature of muscovite was also indicated through a spectral curve of three different zones: muscovite-rich, boundaries between the two zones and pyrophyllite-rich (Fig. 6.7). This shift was also verified in ASD analysis developed by Sepp et al. (2019) however, in a wider range, from 2190 to 2200 nm. This difference was probably associated with a different spatial resolution of the ASD (contact probe spot size: 10 mm (Malvern Panalytical, 2019)) in comparison

to the laboratory Specim instrument (pixel size: 26  $\mu\text{m}$ ). Even though the ASD instrument presents a higher spectral resolution and spectral sampling than the Specim instrument, the shift only occurred along the boundaries of the two minerals, a discrete occurrence. Thus, the higher spatial resolution of the Specim instrument would allow this identification.

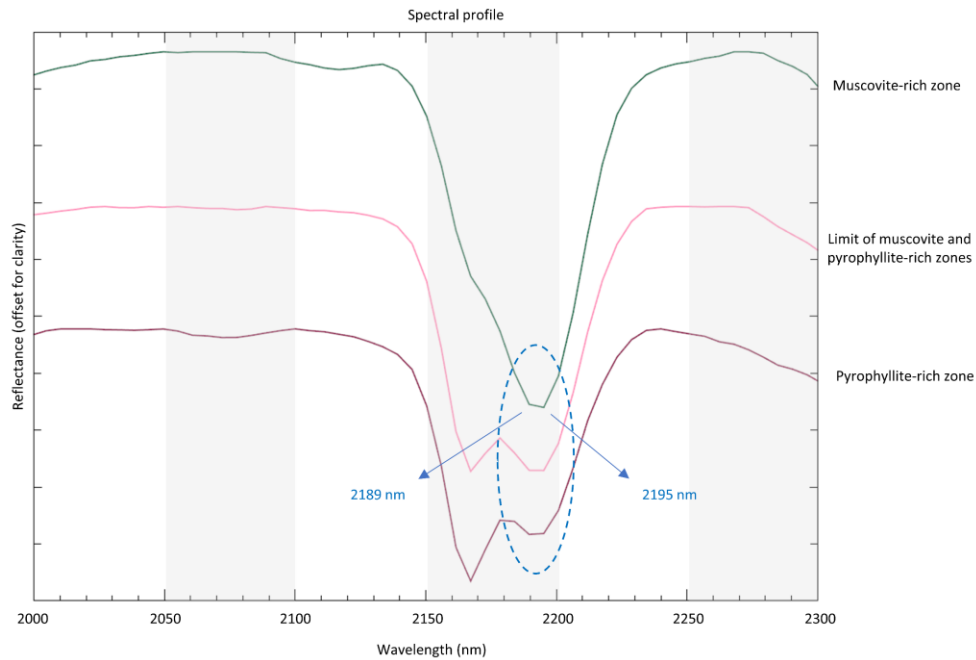


Figure 6.7: Spectral profile to indicate the shift of the wavelength position of the Al-OH absorption feature of muscovite through different zones of a sample.

The initial consideration of the shift of the wavelength position of the Al-OH absorption feature for muscovite was a mixed pixel of pyrophyllite and muscovite, especially in the boundary zones. However, the synthetic linear mixture created for the spectral index showed that a mixture of the two minerals would result in a shift of the wavelength position of the Al-OH absorption feature for both pyrophyllite and muscovite (Appendix XI). Since in fig. 6.7, no shift was observed on the pyrophyllite feature at 2167 nm, the mixed pixel explanation is not very likely.

Therefore, with this initial consideration discarded, the shift in the wavelength position of the Al-OH absorption feature of muscovite could be the result of the intergrowth of pyrophyllite and muscovite, independently of the temporal relationship of both minerals. As discussed by Sepp et al. (2019), a crystal lattice modification was generated by the interlayer with pyrophyllite and muscovite sheets. Thus, either pyrophyllite overprinting muscovite or muscovite overprinting pyrophyllite, the interlayer of both minerals would still exist, generate a crystal lattice distortion and, therefore, a shift in the wavelength position of the Al-OH absorption feature of muscovite.

The intergrowth was observed in backscattered electron (BSE) images of samples which presented the wavelength shift (figure 6.8). The next step was the definition of the temporal relationship of this intergrowth, therefore characterising the overprinting texture. As observed in the four samples showed in fig. 6.8, the crystals of pyrophyllite were covered by sheets of muscovite (red circle). By analysing how the crystals were displayed, especially at the border of each crystal, this interpretation was drawn. The texture was characterised from larger sheets of muscovite over pyrophyllite (Fig. 6.8.R875367b; Fig. 6.8.R875478) to very subtle overprint of a muscovite crystal over a pyrophyllite sheet (Fig.6.8.R875327b; Fig. 6.8.R875524b). In the case of sample R875327 (Fig.6.8.R875327a-b), in which the texture interpreted from the wavelength maps and spectral index were not conclusive, the backscattered electron (BSE) images allowed the confirmation of muscovite overprinting pyrophyllite.

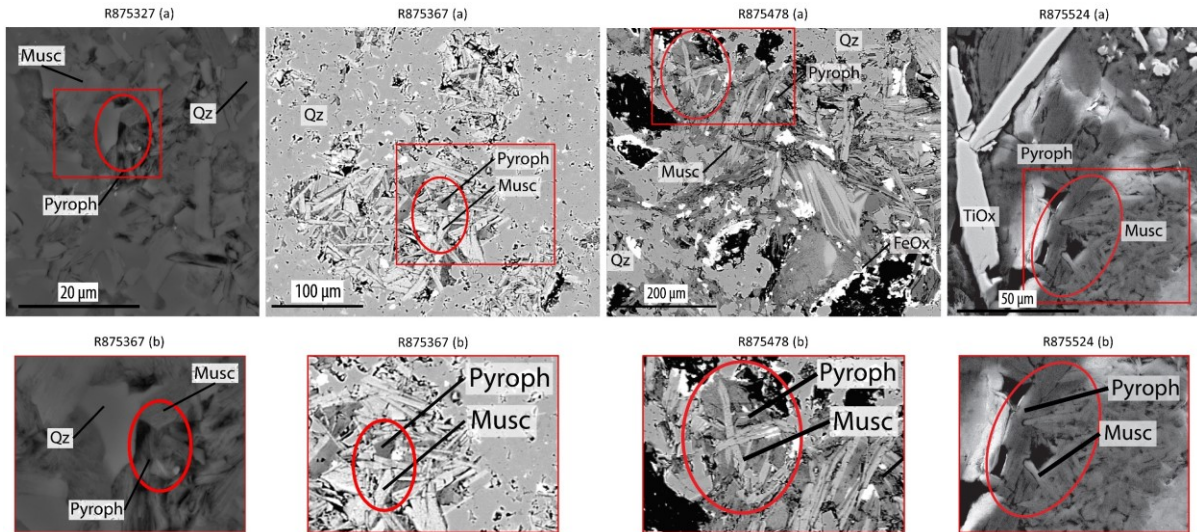


Figure 6.8: Backscattered electron images indicating the intergrowth of pyrophyllite and muscovite sheets in samples where the shift of the wavelength position of the Al-OH absorption feature of muscovite was detected (modified after Sepp et al., 2019). The overprint of muscovite sheets (light grey) over pyrophyllite sheets (dark grey) was detected in all four samples.

To corroborate the interpretation of overprinting patterns, microprobe analysis developed by Sepp et al. (2019) provided evidence of an intergrowth of muscovite and pyrophyllite due to the spots (Fig. 6.9) existing between the bulk of the two minerals (grey polygons in each panel, fig. 6.9.a-c). Each figure illustrated the stoichiometric proportion of the cations and anions per atomic formula units (pafu). To characterise the muscovite composition properly, it was important to consider all possible cations substitutions, hence the figures with K+Na+Ca (Fig. 6.9a), Fe+Mg (Fig. 6.9b) and, Al (Fig. 6.9c) (Michael Sepp, personal communication). As discussed by Sepp et al. (2019), although there is a solid solution series between muscovite and phengite (potassic micas with a replacement of Al by Mg (or Fe) and Al-OH absorption feature longer at around 2220 nm) (Fig. 6.9.a-b), the same was not expected between muscovite and pyrophyllite. Therefore, the few spots between the bulk of the two minerals would characterise an intergrowth not visible in some backscattered images due to its resolution. These few spots in between the bulks also suggested that the replacement of pyrophyllite by muscovite was through reprecipitation mechanism (dissolution) (Michael Sepp, personal communication).

As observed in fig. 6.9, the bulk for pyrophyllite had a more restricted composition variation in comparison to muscovite since pyrophyllite does not have a common cation substitution. This could explain the fact that the intergrowth of pyrophyllite and muscovite does not generate a shift in the Al-OH absorption feature of pyrophyllite, only in the Al-OH muscovite absorption feature. Also, in fig. 6.9c, it was verified that most of the muscovite that replaced pyrophyllite was low on Fe+Mg, which would corroborate the occurrence of pyrophyllite with short-wavelength range muscovite (< 2200 nm).

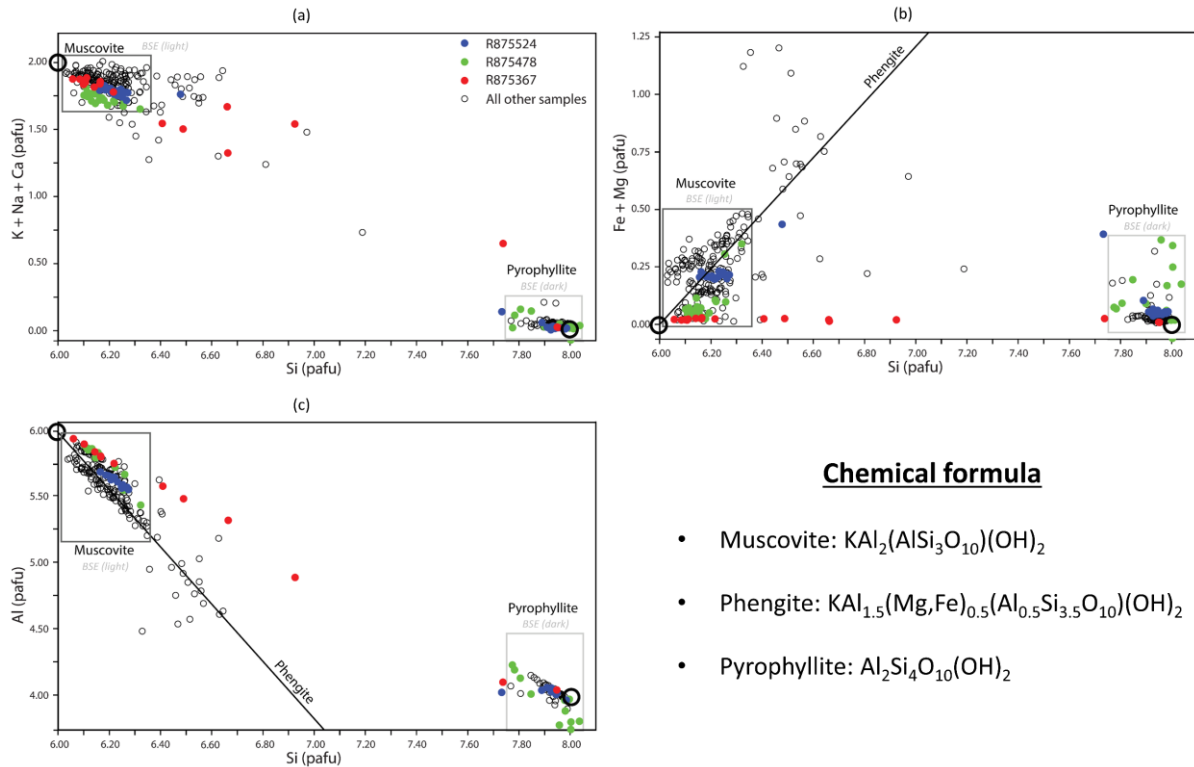


Figure 6.9: Microprobe analysis graphic corroborating the intergrowth of muscovite and pyrophyllite not visible in the backscattered image scale. Spots located in between the bulk of the two minerals would indicate the intergrowth (modified after Sepp et al., 2019). Subfigure (a), (b) and (c) indicating possible cations substitution which could occur in muscovite composition. The values for x and y-axis are doubled in comparison with the chemical formula because the stoichiometric proportion was calculated on a basis typical for phyllosilicates (Michael Sepp, personal communication).

### 6.5. Overprinting at the airborne scale

Since one of the objectives of this research was to understand to what extent the overprinting patterns can be observed different scales, the following step of this discussion is related to the hyperspectral airborne data. As discussed in the previous paragraphs, the recognition of overprinting patterns was based on subtle variations of 5-6 nm in the wavelength position of the Al-OH absorption feature and intergrowth of muscovite and pyrophyllite sheets at a micrometre scale. Considering that the ProSpecTIR is a 1m spatial resolution data with a spectral sampling of 10-12 nm, the direct association of overprinting patterns would not be feasible. Nevertheless, the combination of the 2150-2250 nm wavelength map, the classified image of the spectral index, the contact zones defined in section 5.1 and the samples with overprinting patterns led to the identification of a pattern that could be related to the overprinting occurrence. To understand these contact zones, they were displayed over the geologic map of the central region of the study area and quartz-dominant feeder structures (Michael Sepp, unpublished work) (Fig. 6.10). The gradual transition was interpreted as contact zones between concordant lithologies (columnar section, Appendix XII), from the same volcanic sequence (NE gradual contact, fig. 6.10) or different volcanic sequences (SW gradual contact, fig. 6.10).

The association of overprinting patterns in Specim samples with areas with abrupt or intercalary contact zones was observed (also verified in the spectral index classified image). In fig. 6.10, samples with overprinting patterns were identified in the margins of the feeders, as mapped by Sepp et al. (2019), highlighting the importance of these contact zones.

The abrupt zones were interpreted as the result of isolated quartz-dominant feeders with its extension limited by faults and boundaries with concordant lithologies (Artesia Lake Volcanics units). Although the SW gradual contact zone did present isolated quartz-dominant feeders, there was no faults or dikes to generate an abrupt zone. Hence, this area was classified as a gradual contact zone.

The intercalary zones were interpreted as areas with high occurrence of disseminated silica bodies with its extension also limited by faults. This high occurrence could be explained by the increase in the intensity of alteration towards the contact with Fulstone Spring Volcanics units (Lipske & Dilles, 2000). Granite porphyry and andesite dikes, located in both abrupt and intercalary zones, crosscut the Artesia Lake Volcanics, consequently, cross-cutting the advanced argillic and sericitic alteration. However, due to its late emplacement, there was no association with the overprinting patterns. Therefore, the intercalary and abrupt zones would indicate the emplacement of quartz-dominant feeder structures. As discussed by Sepp et al. (2019), these structures were channels that originated from the intense acid leaching and then filled by near-neutral pH fluids.

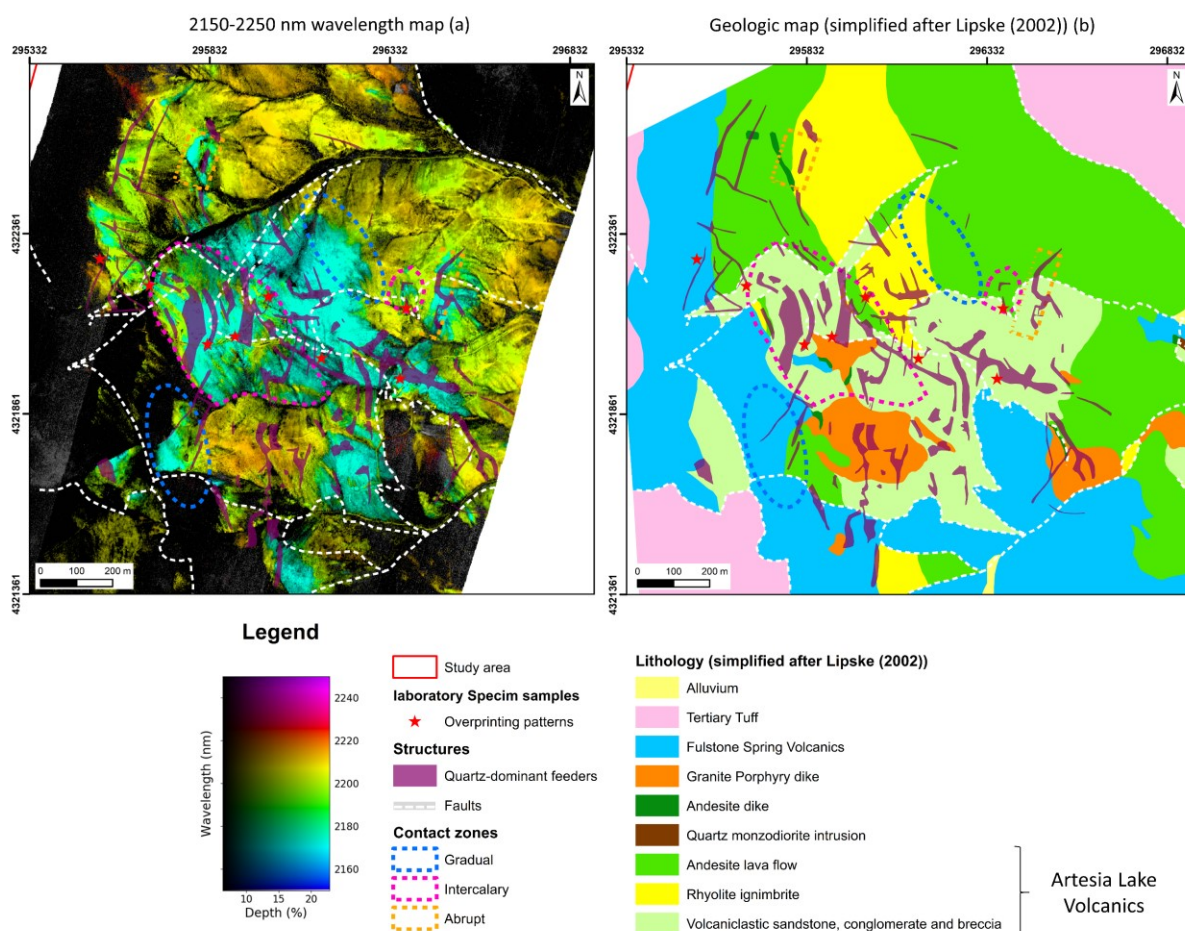


Figure 6.10: Combination of the 2150-2250 nm wavelength map, the contact zones defined in section 5.1 and the samples with overprinting patterns. Quartz-dominant feeder structures from alteration map of Michael Sepp (unpublished work) and geologic map modified after (Lipske, 2002).

In conclusion, pervasive and veinlet-controlled textures (minor occurrences) were characterised and a shift in the wavelength position of the Al-OH absorption feature of muscovite from 2189 to 2195 nm was detected. Although the shift was not a direct indication of overprinting, an intergrowth of pyrophyllite and muscovite sheets was suggested. The temporal relationship of the two minerals was then addressed: first through the interpretation of the alteration texture; second, through the backscattered electron images and microprobe analysis data, confirming the overprint of muscovite over pyrophyllite. Thus, suggesting that a

low pH fluid responsible for an intense acid leaching was followed by near-neutral pH fluid transporting  $K^+$  and, possible trace metals.

The association of a late-stage near-neutral pH fluid and Au introduction to the lithocap has been previously documented in other deposits. In the magmatic-hydrothermal acid-sulphate system at Summitville, CO (USA), Bethke et al. (2005) used stable-isotope and fluid inclusion analysis to conclude that the shallow regions of the system evolved from a low-pH and high-sulfidation system to a nearly neutral pH and low-sulfidation environment. By that, the authors identified that the acid-sulphate alteration preceded the main stage Cu-Au-Ag mineralisation. At the El Indio deposit (Chile), Jannas et al. (1990), verified that the Au emplacement was associated with a tennantite-dominant mineral assemblage indicating an increase in pH over time.

In the case of the Yerington district, the absence of Au in the Buckskin range could be addressed from two perspectives. The first was that the source intrusions did not contain Au, thus no Au to be transported. The second perspective was related to the erosion of 600-800 m of advanced argillic alteration (lithocap) and the Au, hosted in this upper region of the alteration, has probably been eroded with it (Michael Sepp, personal communication). Despite the absence of Au in this area of the Buckskin range, this research has demonstrated the importance of characterising and mapping overprinting patterns at different scales to assist the reconstruction of fluid composition and fluid emplacement. Therefore, contributing to an improved understanding of a high sulfidation epithermal system and a better definition of target areas for mineral exploration studies.

## 7. CONCLUSIONS AND RECOMMENDATIONS

### 7.1. Conclusions

This research combined proximal and remote sensing data to characterise the pyrophyllite-muscovite association in the Buckskin range, Yerington district, Nevada (USA).

By combining different ranges of wavelength maps, the hydrothermal alteration mineralogy was mapped at both scales. In the airborne ProSpecTIR data, this allowed the identification of an outward zoning alteration pattern from an inner zone of alunite  $\pm$  pyrophyllite in contact with a muscovite-dominant zone of varied wavelength position (2187-2225 nm) of the Al-OH absorption feature. In the laboratory Specim data, additional and narrower wavelength maps with a 0-50% depth stretch assisted in the characterisation of the hydrothermal alteration mineralogy such as alunite, pyrophyllite, muscovite, dickite, kaolinite, chlorite, topaz and zunyite.

To address the spatial distribution of the pyrophyllite-muscovite association and, consequently, the textural relationship of the two minerals (in the case of the laboratory Specim data), a spectral index was created. For the airborne ProSpecTIR data, the index indicated pyrophyllite and muscovite-rich zones and, combined with the wavelength maps, suggested areas of pyrophyllite dominance over alunite, to distinguish both. Besides, contact zones between alunite  $\pm$  pyrophyllite and muscovite were defined, and abrupt/intercalary contact zones were in accordance with quartz-dominant feeder structures mapped in the study area. For the laboratory Specim data, the spectral index, combined with wavelength maps of a 0-50% depth stretch (not only automatic depth stretch), assisted in the characterisation of the textural relationship between pyrophyllite and muscovite. This step was crucial to highlight the relative proportion of the two minerals and, in samples where they co-occurred, identify the shift in the wavelength position of the Al-OH absorption feature of muscovite, especially in areas where both minerals occurred in about equal amounts. This shift of the Al-OH muscovite absorption feature was interpreted as a crystal lattice distortion because of the intergrowth of pyrophyllite and muscovite. Although not conclusive, the temporal relationship of pyrophyllite-muscovite was inferred from the pervasive and veinlet-controlled texture in the laboratory Specim data. Nevertheless, microprobe analysis and the backscattered electron images confirmed the intergrowth and, assisted in the characterisation of the overprint of muscovite over pyrophyllite. The samples where the overprinting pattern was identified were located along the margins of the quartz-dominant feeder structures.

The association of the spatial distribution with the textural relationship of the pyrophyllite-muscovite association allowed the reconstruction of the fluid chemistry and fluid pathway linked to this scenario. First, a low pH high-temperature magmatic-hydrothermally derived fluid characterised by the presence of alunite  $\pm$  pyrophyllite, responsible for an intense acid leaching and, consequently, the generation of permeable zones in the lithocap. Then, these permeable zones worked as channels (feeders) for the emplacement of a late-stage fluids of near-neutral pH and lower salinity, characterised by the occurrence of muscovite  $\pm$  zunyite. Therefore, the characterisation of the pyrophyllite-muscovite association, from its spatial distribution through the airborne data to the textural relationship in the laboratory data, suggested a high sulfidation epithermal context for the Buckskin range, following the current understanding of this system.

This research demonstrated that proximal sensing has great potential in identifying textural patterns associated with the intergrowth of a mineral association. Despite the limitation in defining the temporal relationship of the association, the intergrowth of two minerals which were linked to different fluid emplacements could suggest the occurrence of overprinting patterns. Furthermore, patterns derived from the airborne data (wavelength maps + spectral index) suggested potential areas of fluid pathways. In

conclusion, high spatial resolution hyperspectral SWIR data could be used to minimise target areas for sample collection in a mineral exploration campaign.

## **7.2. Recommendations**

The author suggests the follow-up actions to increase the level of understanding of the current epithermal system and the use of high spatial resolution hyperspectral SWIR data:

- A broader sample collection along the margins of the quartz-dominant feeder structures should be executed to verify if the overprinting patterns occur randomly along these margins or if the size and orientation of the feeders play a role in the occurrence of these textures.
- The methodology described in this study regarding the overprinting patterns should be tested in different high sulfidation epithermal systems to understand how these patterns are verified in similar contexts.
- The methodology should also be replicated in mineral deposits which presented a reverse overprint of pyrophyllite replacing muscovite. Although, it is expected that the shift in the wavelength position of the Al-OH absorption feature of muscovite would still occur despite the temporal relationship of the intergrowth.



# LIST OF REFERENCES

- Baissa, R., Labbassi, K., Launeau, P., Gaudin, A., & Ouajhain, B. (2011). Using HySpex SWIR-320m hyperspectral data for the identification and mapping of minerals in hand specimens of carbonate rocks from the Ankloute Formation (Agadir Basin, Western Morocco). *Journal of African Earth Sciences*, 61, 1–9. <https://doi.org/10.1016/j.jafrearsci.2011.04.003>
- Bakker, W. H., & van Ruitenbeek, F. J. A. (2019). *Processing Instructions for SPECIM - Hyperspectral Imagery VNIR & SWIR*. Enschede, Netherlands.
- Bakker, W. H., van Ruitenbeek, F. J. A., & van der Werff, H. M. A. (2011). Hyperspectral image mapping by automatic color coding of absorption features. In *7th EARSEL Workshop of the Special Interest Group in Imaging Spectroscopy*. (pp. 56–57). Edinburgh, U.K.
- Bedini, E., van der Meer, F., & van Ruitenbeek, F. J. A. (2009). Use of HyMap imaging spectrometer data to map mineralogy in the Rodalquilar caldera, southeast Spain. *International Journal of Remote Sensing*, 30(2), 327–348. <https://doi.org/10.1080/01431160802282854>
- Bethke, P. M., Rye, R. O., Stoffregen, R. E., & Vikre, P. G. (2005). Evolution of the magmatic-hydrothermal acid-sulfate system at Summitville, Colorado: Integration of geological, stable-isotope, and fluid-inclusion evidence. *Chemical Geology*, 215(1-4 SPEC. ISS.), 281–315. <https://doi.org/10.1016/j.chemgeo.2004.06.041>
- Brown, A. J., Cudahy, T. J., & Walter, M. R. (2006). Hydrothermal alteration at the Panorama Formation, North Pole Dome, Pilbara Craton, Western Australia. *Precambrian Research*, 151, 211–223. <https://doi.org/10.1016/j.precamres.2006.08.014>
- Clark, R. N., King, T. V. V., Klejwa, M., Swayze, G. A., & Vergo, N. (1990). High spectral resolution reflectance spectroscopy of minerals. *Journal of Geophysical Research*, 95(B8). <https://doi.org/10.1029/jb095ib08p12653>
- Cooke, D. R., White, N. C., Zhang, L., Chang, Z., & Chen, H. (2017). Lithocaps – characteristics, origins and significance for porphyry and epithermal exploration. In *Mineral Resources to Discover - 14 th SGA Biennial Meeting* (pp. 291–294).
- Cudahy, T. J., Wilson, J., Hewson, R., Linton, P., Harris, P., Sears, M., ... Hackwell, J. A. (2001). Mapping porphyry-skarn alteration at Yerington, Nevada, using airborne hyperspectral VNIR-SWIR-TIR imaging data. In *IGARSS 2001. Scanning the Present and Resolving the Future. IEEE 2001 International Geoscience and Remote Sensing Symposium* (Vol. 2, pp. 631–633). <https://doi.org/10.1109/IGARSS.2001.976573>
- Dalm, M., Buxton, M. W. N., & van Ruitenbeek, F. J. A. (2017). Discriminating ore and waste in a porphyry copper deposit using short-wavelength infrared (SWIR) hyperspectral imagery. *Minerals Engineering*, 105, 10–18. <https://doi.org/10.1016/j.mineng.2016.12.013>
- Dilles, J. H., & Einaudi, M. T. (1992). Wall-Rock Alteration and Hydrothermal Flow Paths about the Ann-Mason Porphyry Copper Deposit, Nevada - A 6-km Vertical Reconstruction. *Economic Geology*, 87, 1963–2001. <https://doi.org/10.2113/gsecongeo.87.8.1963>
- Dilles, J. H., Einaudi, M. T., Proffett Jr., J. M., & Barton, M. D. (2000). Overview of the Yerington Porphyry Copper District: Magmatic to Nonmagmatic Sources of Hydrothermal Fluids, Their Flow Paths, Alteration Affects on Rocks, and Cu-Mo-Fe-Au Ores. In *Part I. Contrasting Styles of Intrusion-Associated Hydrothermal Systems: Part II. Geology & Gold Deposits of the Getchell Region* (Society of, Vol. 32, pp. 55–66).
- Esri. (2019). ArcGIS - World Imagery. Retrieved October 24, 2019, from <http://www.arcgis.com/home/webmap/viewer.html?useExisting=1&layers=10df2279f9684e4a9f6a7f08febac2a9>

- Fagbohun, B. J. (2015). *Combining dominant spectral features in airborne SWIR and TIR imagery for mineralogical mapping*. Master's Thesis. University of Twente.
- Gustafson, L. B., & Hunt, J. P. (1975). The Porphyry Copper Deposit at El Salvador, Chile. *Economic Geology*, 70(5), 857–912.
- Hecker, C. A., Rost, E., van der Werff, H. M. A., & Bakker, W. H. (2019a). *Pre-processing SWIR SPECIM images: A beginners guide to de-stripping techniques*. Enschede, Netherlands.
- Hecker, C., van Ruitenbeek, F. J. A., Bakker, W. H., Fagbohun, B. J., Riley, D., van der Werff, H. M. A., & van der Meer, F. D. (2019b). Mapping the wavelength position of mineral features in hyperspectral thermal infrared data. *International Journal of Applied Earth Observation and Geoinformation*, 79, 133–140. <https://doi.org/10.1016/j.jag.2019.02.013>
- Hecker, C., van Ruitenbeek, F. J. A., van der Werff, H. M. A., Bakker, W. H., Hewson, R. D., & Van Der Meer, F. D. (2019c). Spectral absorption feature analysis for finding ore: A tutorial on using the method in geological remote sensing. *IEEE Geoscience and Remote Sensing Magazine*, 7(2), 51–71. <https://doi.org/10.1109/MGRS.2019.2899193>
- Jannas, R. R., Beane, R. E., Ahler, B. A., & Brosnahan, D. R. (1990). Gold and copper mineralization at the El Indio deposit, Chile. *Journal of Geochemical Exploration*, 36(1–3), 233–266. [https://doi.org/10.1016/0375-6742\(90\)90057-H](https://doi.org/10.1016/0375-6742(90)90057-H)
- Khashgerel, B. E., Rye, R. O., Kavalieris, I., & Hayashi, K. I. (2009). The Sericitic to Advanced Argillic Transition: Stable Isotope and Mineralogical Characteristics from the Hugo Dummett Porphyry Cu-Au Deposit, Oyu Tolgoi District, Mongolia. *Economic Geology*, 104(8), 1087–1110.
- Kokaly, R. F., Clark, R. N., Swayze, G. A., Livo, K. E., Hoefen, T. M., Pearson, N. C., ... Klein, A. J. (2017). *USGS Spectral Library Version 7. Data Series*. Reston, VA. <https://doi.org/10.3133/ds1035>
- Lipske, J. L. (2002). *Advanced Argillic and Sericitic Alteration in the Subvolcanic Environment of the Yerington Porphyry Copper System, Buckskin Range, Nevada (Master's Thesis)*. Oregon State University.
- Lipske, J. L., & Dilles, J. H. (2000). Advanced Argillic and Sericitic Alteration in the Subvolcanic Environment of the Yerington Porphyry Copper System, Buckskin Range, Nevada. In J. H. Dilles, M. D. Barton, D. A. Johnson, J. M. Proffett, M. T. Einaudi, & E. J. Crafford (Eds.), *Part I. Contrasting Styles of Intrusion-Associated Hydrothermal Systems: Part II. Geology & Gold Deposits of the Getchell Region* (Vol. 32, pp. 91–99). Society of Economic Geologists. <https://doi.org/10.5382/GB.32>
- Malvern Panalytical. (2019). *ASD FIELDSPEC® 4 The industry-leading portable device for field spectroscopy*. Worcestershire, UK.
- Mathieu, M., Roy, R., Launeau, P., Cathelineau, M., & Quirt, D. (2017). Alteration mapping on drill cores using a HySpex SWIR-320m hyperspectral camera: Application to the exploration of an unconformity-related uranium deposit (Saskatchewan, Canada). *Journal of Geochemical Exploration*, 172, 71–88. <https://doi.org/10.1016/j.gexplo.2016.09.008>
- McQueen, K. G. (2005). Ore deposit types and their primary expressions. In S. M. Cornelius & I. D. M. Robertson (Eds.), *Regolith Expression of Australian Ore Systems: A Compilation of Exploration Case Histories with Conceptual Dispersion, Process and Exploration Models* (pp. 1–14). Australia.
- Meller, C., & Kohl, T. (2014). The significance of hydrothermal alteration zones for the mechanical behavior of a geothermal reservoir. *Geothermal Energy*, 2(12), 1–21.
- Oniemayin, I. B., Theophilus, T. I., Chidozie, E. P., Ayobami, B., Gideon, B., & Kofoworola, D. (2016). Spectral Responses and Classification of Earth's Features on Satellite Imagery. In *3rd International Conference on African Development Issues (CU-ICADI)* (pp. 365–367).
- Pirajno, F. (2009). Hydrothermal Processes and Wall Rock Alteration. In *Hydrothermal processes and mineral systems* (1st ed., pp. 73–165). Springer Netherlands. <https://doi.org/10.1007/978-1-4020-8613-7>
- Pontual, S., Merry, N., & Gamson, P. (1997). *G-MEX: Spectral Analysis Guide for Mineral Exploration. Vol.1:*

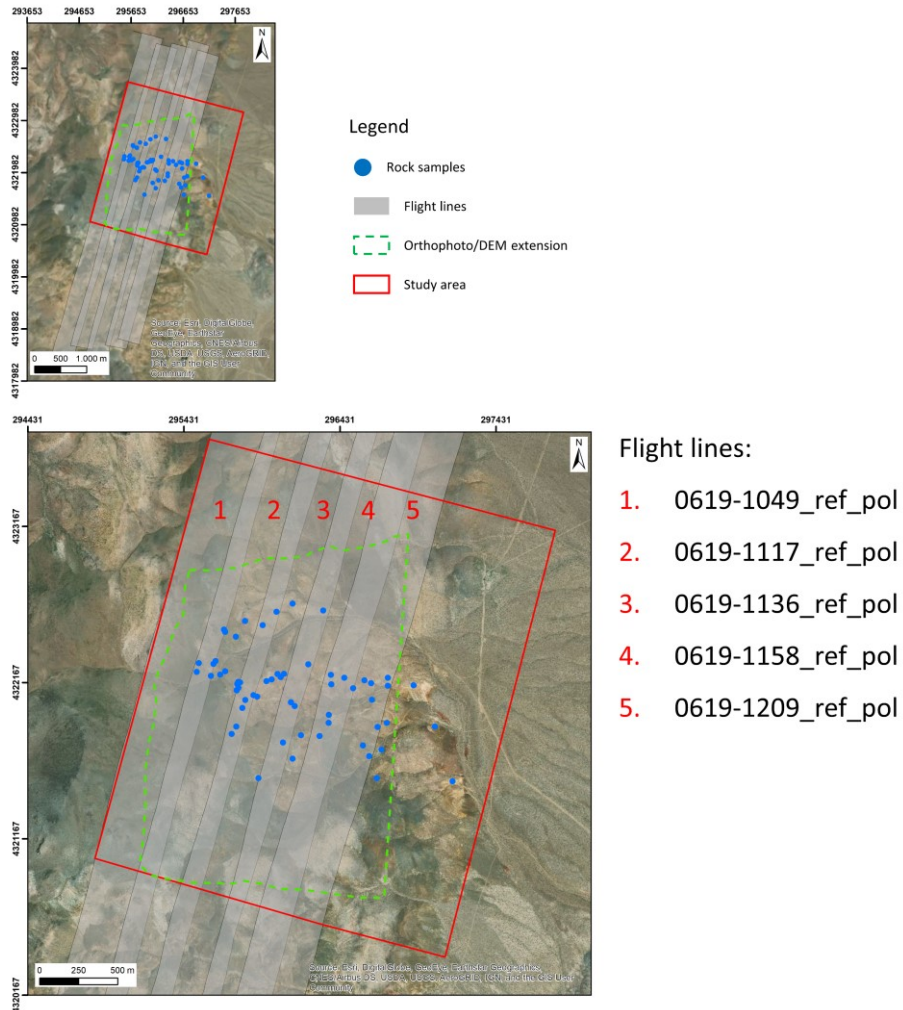
*Spectral Interpretation Field Manual*. Victoria, Australia: AusSpec International Pty. Ltd.

- Proffett, J. M. (1977). Cenozoic geology of the Yerington district, Nevada, and implications for the nature and origin of Basin and Range faulting. *GSA Bulletin*, 88(2), 247–266.
- Proffett, J. M. J., & Dilles, J. H. (1984). Geologic map of the Yerington district, Nevada. Nevada: Nevada Bureau Mines Geologic Map 77, scale 1:24000.
- Rottier, B., Kouzmanov, K., Casanova, V., Wälle, M., & Fontboté, L. (2018). Cyclic Dilution of Magmatic Metal-Rich Hypersaline Fluids by Magmatic Low-Salinity Fluid: A Major Process Generating the Giant Epithermal Polymetallic Deposit of Cerro de Pasco, Peru. *Economic Geology*, 113(4), 825–856. <https://doi.org/10.5382/econgeo.2018.4573>
- Seedorff, E., Dilles, J. H., Proffett Jr., J. M., Einaudi, M. T., Zurcher, L., Stavast, W. J. A., ... Barton, M. D. (2005). Porphyry Deposits: Characteristics and Origin of Hypogene Features. In J. W. Hedenquist, J. F. H. Thompson, R. J. Goldfarb, & J. P. Richards (Eds.), *One Hundredth Anniversary Volume* (pp. 251–298). Society of Economic Geologists. <https://doi.org/10.5382/AV100.10>
- Sepp, M. (2020). *Documentation to accompany central Buckskein range DEM / Orthophoto generated from Drone Survey*.
- Sepp, M., Lipske, J., & Dilles, J. H. (2019). Significance of pyrophyllite-muscovite intergrowths in advanced argillic alteration of porphyry-epithermal systems : Evidence from the Yerington district , Nevada. In *Society of Economic Geologists Conference* (pp. 1–5). Santiago.
- Sillitoe, R. H. (1995). *Exploration of porphyry copper lithocaps* (Series 9). AUSIMM.
- Sillitoe, R. H. (2010). Porphyry copper systems. *Economic Geology*, 105, 3–41. <https://doi.org/10.2113/gsecongeo.105.1.3>
- Sillitoe, R. H., & Hedenquist, J. W. (2003). Linkages between Volcanotectonic Settings , Ore-Fluid Compositions , and Epithermal Precious Metal Deposits. In S. F. Simmons & I. Graham (Eds.), *Volcanic, Geothermal, and Ore-Forming Fluids: Rulers and Witnesses of Processes within the Earth* (Special Pu, Vol. 10, pp. 315–343). Boulder, USA: Society of Economic Geologists, Inc. <https://doi.org/10.315-343>
- Simmons, S. F., White, N. C., & John, D. A. (2005). Geological Characteristics of Epithermal Precious and Base Metal Deposits. In J. W. Hedenquist, J. F. H. Thompson, R. J. Goldfarb, & J. P. Richards (Eds.), *One Hundredth Anniversary Volume* (pp. 485–522). Society of Economic Geologists. <https://doi.org/10.5382/AV100.16>
- Specim. (2015). *SisuCHEMA: Chemical Imaging Analyzer*. Oulu, Finland. Retrieved from [https://www.specim.fi/downloads/SisuCHEMA\\_2\\_2015.pdf](https://www.specim.fi/downloads/SisuCHEMA_2_2015.pdf)
- SpecTIR. (2008). *SpecTIR Project Report - 1281 - Aerospace Joint Collect*.
- Swayze, G. A., Clark, R. N., Goetz, A. F. H., Livo, K. E., Breit, G. N., Kruse, F. A., ... Ashley, R. P. (2014). Mapping Advanced Argillic Alteration at Cuprite, Nevada, Using Imaging Spectroscopy. *Economic Geology*, 109, 1179–1221.
- Taylor, R. (2009). *Ore Textures: Recognition and Interpretation* (1st ed.). Springer-Verlag Berlin Heidelberg. <https://doi.org/10.1017/CBO9781107415324.004>
- van der Meer, F. D. (2018). Near-infrared laboratory spectroscopy of mineral chemistry: A review. *International Journal of Applied Earth Observation and Geoinformation*, 65, 71–78. <https://doi.org/10.1016/j.jag.2017.10.004>
- van der Meer, F. D., van der Werff, H. M. A., van Ruitenbeek, F. J. A., Hecker, C. A., Bakker, W. H., Noomen, M. F., ... Woldai, T. (2012). Multi- and hyperspectral geologic remote sensing: A review. *International Journal of Applied Earth Observation and Geoinformation*, 14, 112–128. <https://doi.org/10.1016/j.jag.2011.08.002>

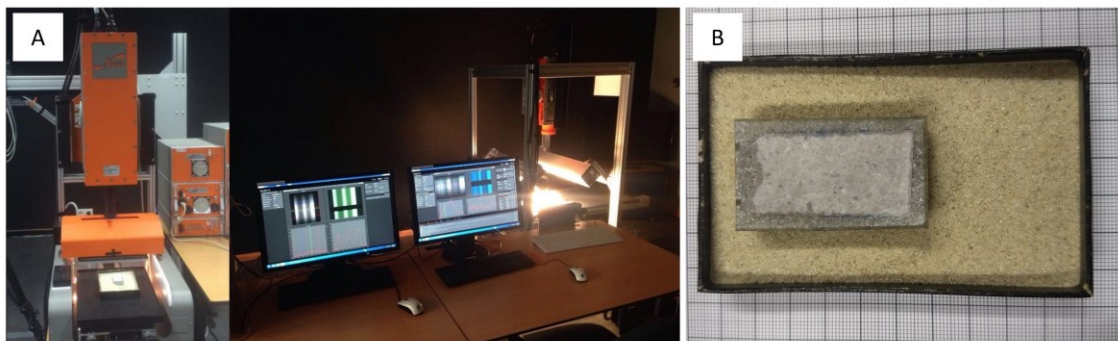
- van Ruitenbeek, F. J. A., Bakker, W. H., van Der Werff, H. M. A., Zegers, T. E., Oosthoek, J. H. P., Omer, Z. A., ... van Der Meer, F. D. (2014). Mapping the wavelength position of deepest absorption features to explore mineral diversity in hyperspectral images. *Planetary and Space Science*, *101*, 108–117. <https://doi.org/10.1016/j.pss.2014.06.009>
- van Ruitenbeek, F. J. A., Cudahy, T., Hale, M., & van der Meer, F. D. (2005). Tracing fluid pathways in fossil hydrothermal systems with near-infrared spectroscopy. *Geology*, *33*(7), 597–600. <https://doi.org/10.1130/G21375.1>
- van Ruitenbeek, F. J. A., Debba, P., van der Meer, F. D., Cudahy, T., van der Meijde, M., & Hale, M. (2006). Mapping white micas and their absorption wavelengths using hyperspectral band ratios. *Remote Sensing of Environment*, *102*, 211–222. <https://doi.org/10.1016/j.rse.2006.02.012>
- van Ruitenbeek, F. J. A., van der Werff, H. M. A., Bakker, W. H., Hewson, R. D., Hecker, C. A., & van der Meer, F. D. (2019). Infrared spectral imaging of rock mineralogy and microstructure: powerpoint. In *Nederlands Aardwetenschappelijk Congres 2019* (pp. 1–22). Utrecht, Netherlands.
- van Ruitenbeek, F. J. A., van der Werff, H. M. A., Bakker, W. H., van der Meer, F. D., & Hein, K. A. A. (2019). Measuring rock microstructure in hyperspectral mineral maps. *Remote Sensing of Environment*, *220*, 94–109. <https://doi.org/10.1016/j.rse.2018.10.030>
- Watanabe, Y., & Hedenquist, J. (2001). Mineralogic and Stable Isotope Zonation at the Surface over the El Salvador Porphyry Copper Deposit, Chile. *Economic Geology*, *96*, 1775–1797.
- Williams-Jones, A. E., & Heinrich, C. A. (2005). 100th Anniversary Special Paper: Vapor Transport of Metals and the Formation of Magmatic-Hydrothermal Ore Deposits. *Economic Geology*, *100*(7), 1287–1312. <https://doi.org/10.2113/gsecongeo.100.7.1287>
- Zaini, N., van der Meer, F., & van der Werff, H. (2014). Determination of carbonate rock chemistry using laboratory-based hyperspectral imagery. *Remote Sensing*, *6*, 4149–4172. <https://doi.org/10.3390/rs6054149>

# APPENDIX

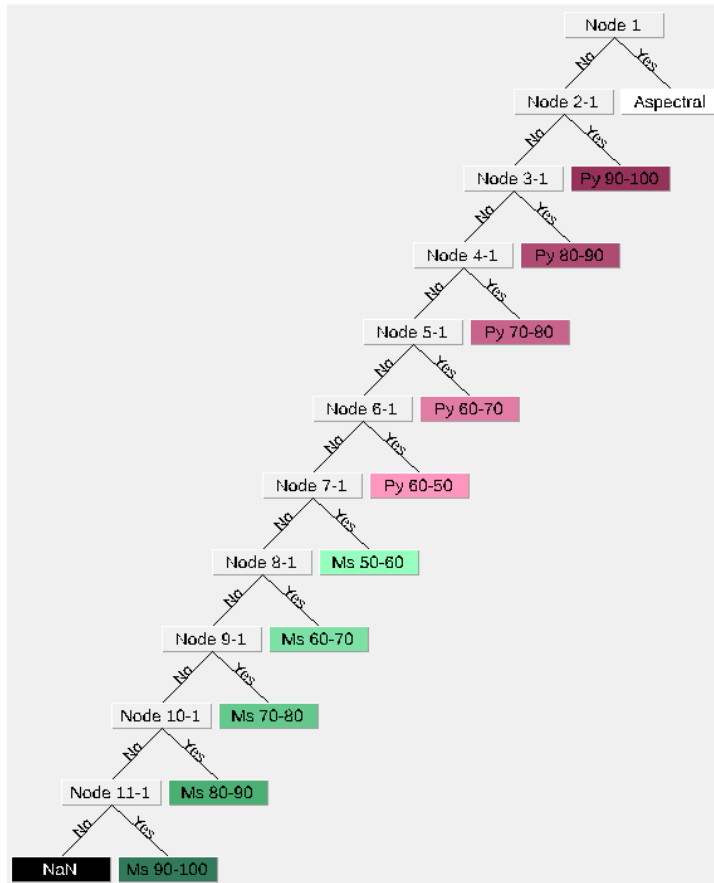
APPENDIX I: Distribution of the flight lines and rock samples collected for laboratory analysis (Base map from Esri (2019)).



APPENDIX II: A: SisuCHEMA SWIR setup at the GeoScience Lab of Faculty ITC, University of Twente (van Ruitenbeek et al., 2019). B: Rock slab thin section placed on a sandbox for measurement (Sample from the data set of this research).



APPENDIX III: Decision tree defined for the spectral indices:



ProSpecTIR spectral index

```

begin node
name = "Node 1"
type = Decision
location = 1,1
expression = "B1 EQ 0.0000"
end node
  
```

```

begin node
name = "Aspectral"
type = Result
location = 2,2
parent name = "Node 1"
parent decision = Yes
class value = 1
class rgb = 0,0,0
end node
  
```

```

begin node
name = "Node 2-1"
type = Decision
location = 2,1
parent name = "Node 1"
parent decision = No
expression = "(B1 GT 0.6000) AND (B1 LE 0.7417)"
end node
  
```

```

begin node
name = "Py 90-100"
type = Result
location = 3,2
parent name = "Node 2-1"
parent decision = Yes
class value = 3
class rgb = 150,50,90
end node
  
```

```

begin node
name = "Node 3-1"
type = Decision
location = 3,1
parent name = "Node 2-1"
parent decision = No
expression = "(B1 GT 0.7417) AND (B1 LE 0.7777)"
end node
  
```

```

begin node
name = "Py 80-90"
type = Result
location = 4,2
parent name = "Node 3-1"
parent decision = Yes
class value = 4
class rgb = 175,75,115
end node
  
```

```

begin node
name = "Node 4-1"
type = Decision
location = 4,1
parent name = "Node 3-1"
parent decision = No
expression = "(B1 GT 0.7777) AND (B1 LE 0.8161)"
end node
  
```

```

begin node
name = "Py 70-80"
type = Result
location = 5,2
parent name = "Node 4-1"
parent decision = Yes
class value = 5
class rgb = 200,100,140
end node
  
```

```

begin node
name = "Node 5-1"
type = Decision
location = 5,1
parent name = "Node 4-1"
parent decision = No
expression = "(B1 GT 0.8161) AND (B1 LE 0.8572)"
end node
  
```

```

begin node
name = "Py 60-70"
type = Result
location = 6,2
parent name = "Node 5-1"
parent decision = Yes
class value = 6
class rgb = 225,125,165
end node
  
```

```

begin node
name = "Node 6-1"
type = Decision
location = 6,1
parent name = "Node 5-1"
parent decision = No
expression = "(B1 GT 0.8572) AND (B1 LE 0.9012)"
end node
  
```

```

begin node
name = "Py 60-50"
type = Result
location = 7,2
parent name = "Node 6-1"
parent decision = Yes
class value = 7
class rgb = 255,150,190
end node
  
```

```

begin node
name = "Node 7-1"
type = Decision
location = 7,1
parent name = "Node 6-1"
parent decision = No
expression = "(B1 GT 0.9012) AND (B1 LE 0.9483)"
end node
  
```

```

begin node
name = "Ms 50-60"
type = Result
location = 8,2
parent name = "Node 7-1"
parent decision = Yes
class value = 8
class rgb = 150,255,190
end node
  
```

```

begin node
name = "Node 8-1"
type = Decision
location = 8,1
parent name = "Node 7-1"
parent decision = No
expression = "(B1 GT 0.9483) AND (B1 LE 0.9980)"
end node
  
```

```

begin node
name = "Ms 60-70"
type = Result
location = 9,2
parent name = "Node 8-1"
parent decision = No
expression = "(B1 GT 0.9980) AND (B1 LE 1.0513)"
end node
  
```

```

begin node
name = "Node 9-1"
type = Decision
location = 9,1
parent name = "Node 8-1"
parent decision = Yes
class value = 9
class rgb = 125,225,165
end node
  
```

```

begin node
name = "Ms 70-80"
type = Result
location = 10,2
parent name = "Node 9-1"
parent decision = Yes
class value = 10
class rgb = 100,200,140
end node
  
```

```

begin node
name = "Node 10-1"
type = Decision
location = 10,1
parent name = "Node 9-1"
parent decision = No
expression = "(B1 GT 1.0513) AND (B1 LE 1.1091)"
end node
  
```

```

begin node
name = "Ms 80-90"
type = Result
location = 11,2
parent name = "Node 10-1"
parent decision = Yes
class value = 11
class rgb = 75,175,115
end node
  
```

```

begin node
name = "Node 11-1"
type = Decision
location = 11,1
parent name = "Node 10-1"
parent decision = No
expression = "(B1 GT 1.1091) AND (B1 LE 1.4000)"
end node
  
```

```

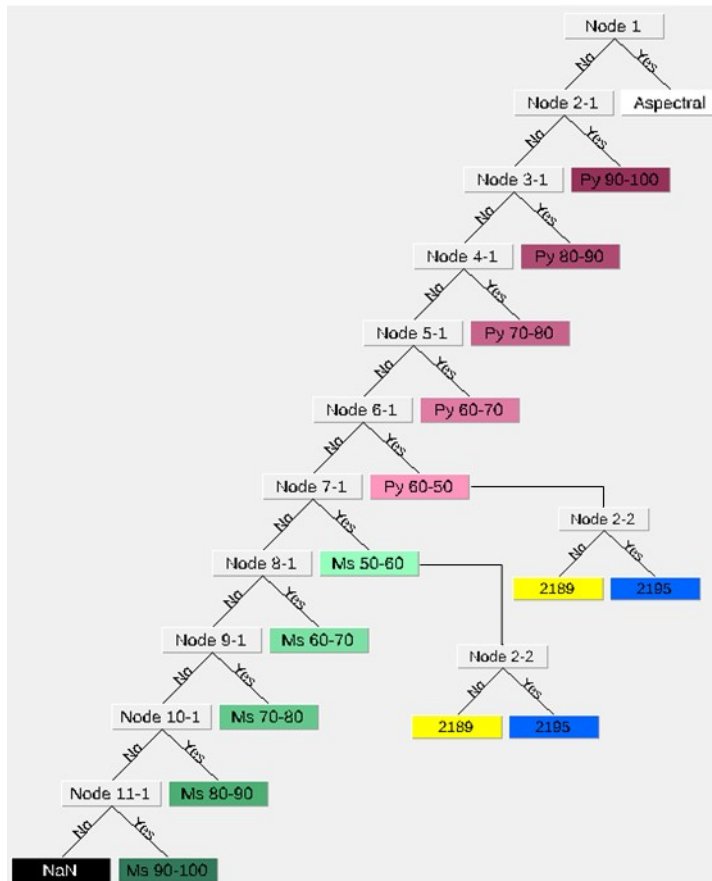
begin node
name = "Ms 90-100"
type = Result
location = 12,2
parent name = "Node 11-1"
parent decision = Yes
class value = 12
class rgb = 50,120,90
end node
  
```

```

begin node
name = "NaN"
type = Result
location = 12,1
parent name = "Node 11-1"
parent decision = No
class value = 2
class rgb = 255,255,255
end node
  
```



APPENDIX III: Decision tree defined for the band ratio of the shift of the wavelength position of the Al-OH absorption feature of muscovite. The text refers only to the decision tree of wavelength shift.



```
begin node
name = "Node 1"
type = Decision
location = 1,1
expression = "(B1 GT 0.8500)
AND (B1 LE 1.1000)"
end node
```

```
begin node
name = "Node 2-2"
type = Decision
location = 2,2
parent name = "Node 1"
parent decision = Yes
expression = "B2 GT 1.0000000"
end node
```

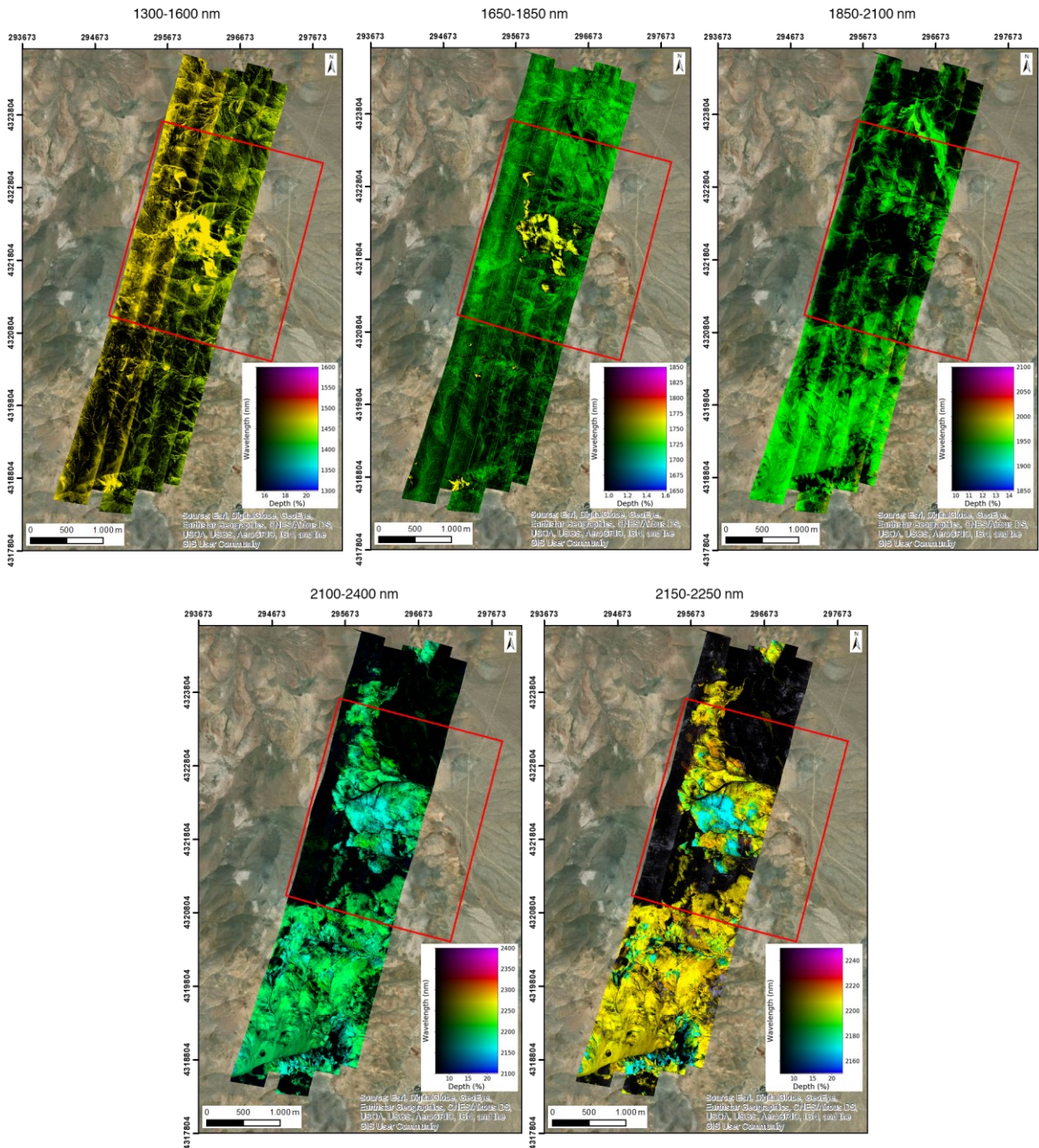
```
begin node
name = "2195"
type = Result
location = 3,4
parent name = "Node 2-2"
parent decision = Yes
class value = 3
class rgb = 0,100,255
end node
```

```
begin node
name = "2189"
type = Result
location = 3,3
parent name = "Node 2-2"
parent decision = No
class value = 4
class rgb = 255,255,0
end node
```

```
begin node
name = "Class 2"
type = Result
location = 2,1
parent name = "Node 1"
parent decision = No
class value = 2
class rgb = 0,0,0
end node
```

APPENDIX IV: Full extension of the wavelength maps of the ProSpecTIR data. Study area delimited by the red polygon. (Base map from Esri (2019)).

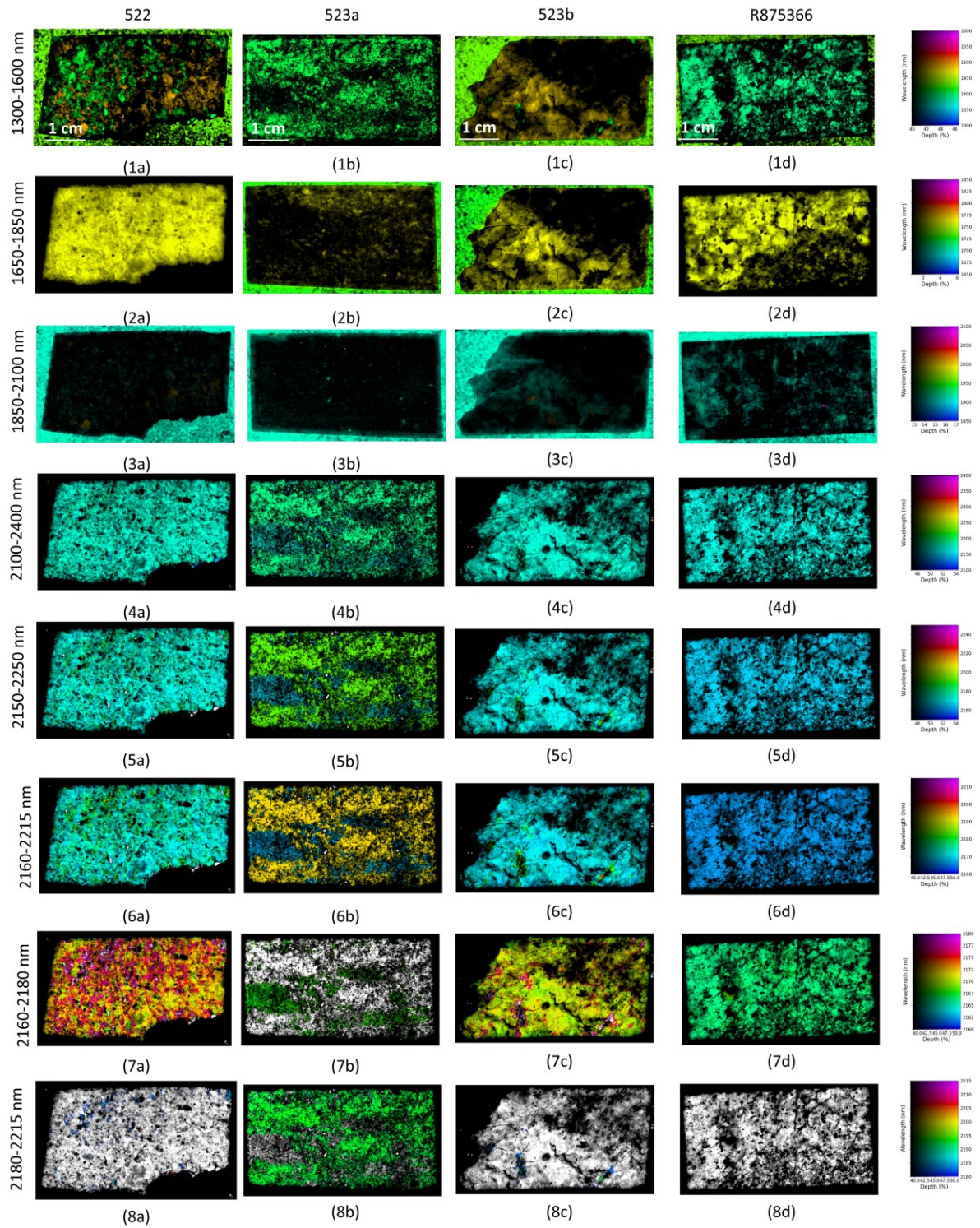
ProSpecTIR wavelength maps – Flight lines full extension (study area in red)



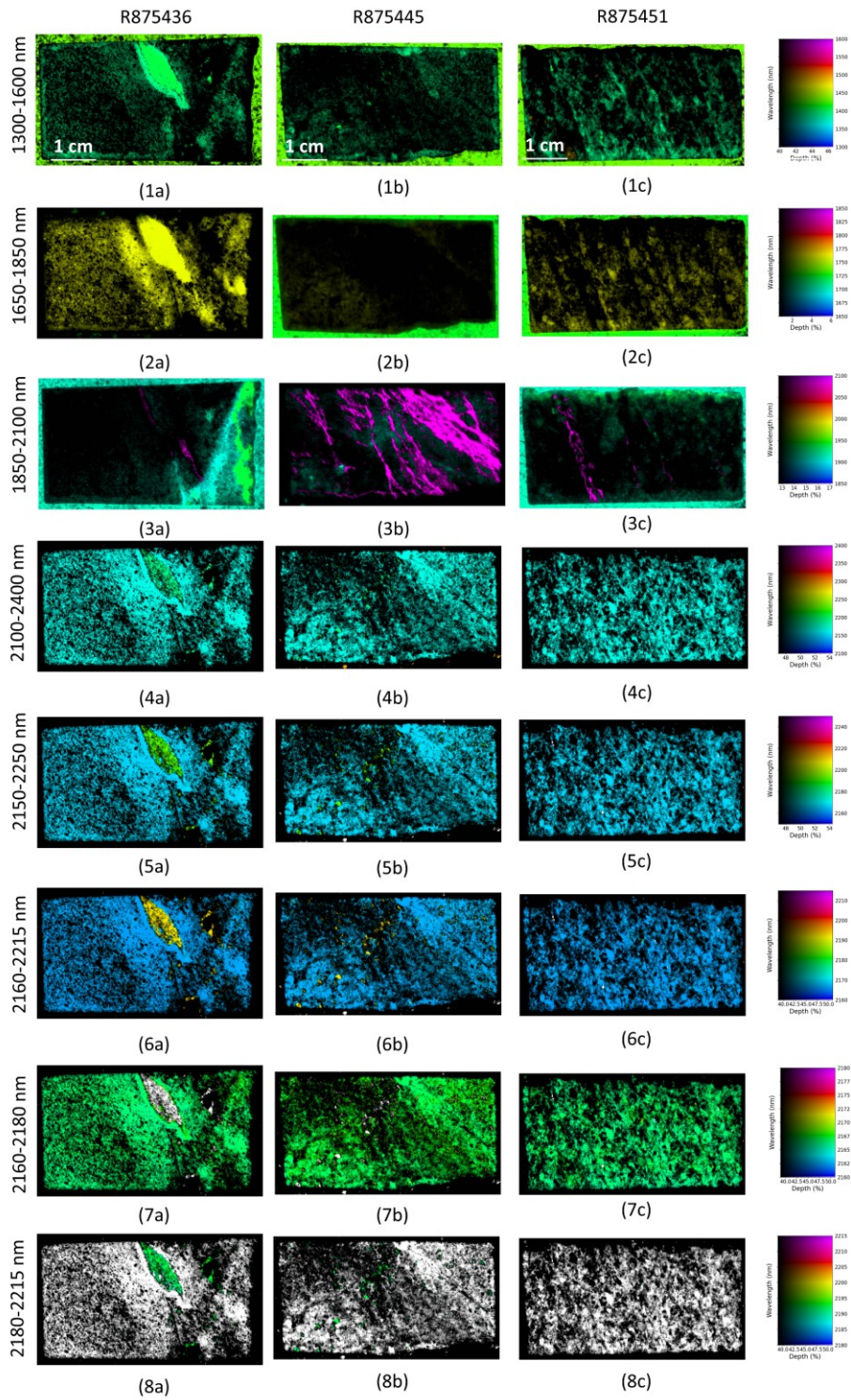
APPENDIX V: Information of the samples used for the Specim analysis as for additional analytical methods.

ID	Y	X	Z	SWIR mineralogy	Wavelength position (nm) of the main absorption feature				Pyrophyllite and Muscovite co-occurrence	Pyrophyllite and Muscovite overprinting patterns
					Muscovite	Pyrophyllite	Alunite	Zunyite		
213	39.02761	-119.36	1882.581	Ms ± Chl	2206 - 2211	-	-	-	-	-
214	39.02774	-119.36	1887.632	Ms ± Chl	2211	-	-	-	-	-
242	39.02885	-119.356	1807.387	Ms ± Kaolinite	-	-	-	-	-	-
295	39.02325	-119.359	1858.462	Ms ± Chl	2200-2206	-	-	-	-	-
315	39.02236	-119.349	1719.974	Ms ± Kao	2206 - 2211	-	-	-	-	-
325	39.02066	-119.349	1714.364	Ms ± Chl	2206	-	-	-	-	-
326	39.02128	-119.35	1732.719	Ms ± Chl	2195	-	-	-	-	-
384	39.02393	-119.349	1723.996	Ms	-	-	-	-	-	-
522	39.02463	-119.359	1890.784	Alu ± Ms ± Zun ± Kao - Pyro	2189-2195	2167	2167-2178	2133	YES	-
523a	39.02472	-119.359	1889.583	Ms ± Pyro ± Alu ± Zun	2195	2167	2167	2139	YES	-
523b	39.02472	-119.359	1889.583	Alu ± Ms ± Dickite - Pyro	2195	2167	2167-2178	-	YES	-
664a	39.02426	-119.359	1892.226	Dickite ± Ms ± Zun	2195	-	-	2133	-	-
664b	39.02426	-119.359	1892.226	Alu ± Ms ± Zun	-	-	2167-2172	2133	-	-
664c	39.02426	-119.359	1892.226	Alu ± Pyro ± Zun	-	2167	2167	2133	-	-
665	39.0244	-119.359	1900.878	Alu ± Pyro ± Kao ± Zun	-	2167	2167-2172	2133	-	-
666	39.02474	-119.359	1888.862	Pyro ± Zun ± Dickite	2206	2167	-	2133	-	-
669	39.02132	-119.356	1820.339	Ms	2206-2211	-	-	-	-	-
685	39.02217	-119.359	1837.71	Chl ± Ms	2211	-	-	-	-	-
740	39.02262	-119.348	1707.302	Ms	2211	-	-	-	-	-
753	39.01924	-119.357	1805.049	Chl ± Ms	2217	-	-	-	-	-
801	39.02476	-119.348	1698.392	Ms	2206	-	-	-	-	-
806	39.02735	-119.359	1845.935	Chl ± Kao	2206	-	-	-	-	-
808	39.02508	-119.356	1867.633	Alu ± Zun ± Tpz	-	-	2167-2172	2133	-	-
R875315	39.02827	-119.359	1847.973	Alu	-	-	2167-2172	-	-	-
R875327	39.02372	-119.359	1876.964	Pyro ± Ms	2189-2195	2167	-	-	YES	YES
R875366	39.02514	-119.36	1839.854	Pyro ± Ms ± Alu ± Dickite	2189-2195	2167	2167-2172	-	YES	YES
R875367	39.02578	-119.362	1883.487	Ms ± Pyro	2189-2195	2167	-	-	YES	YES
R875371	39.02527	-119.362	1880.414	Ms	2206	-	-	-	-	-
R875376	39.02506	-119.361	1860.871	Ms ± Chl	2200	-	-	-	-	-
R875382	39.02593	-119.361	1849.422	Pyro ± Dickite	-	2167	-	-	-	-
R875383	39.02575	-119.361	1854.047	Ms	2195	-	-	-	-	-
R875388	39.02806	-119.357	1820.853	Ms	2211	-	-	-	-	-
R875389	39.02935	-119.355	1800.81	Ms	2200	-	-	-	-	-
R875390	39.02899	-119.353	1764.933	Ms ± Chl	2195-2200	-	-	-	-	-
R875398	39.02535	-119.36	1842.928	Alu ± Ms ± Dickite	2189-2206	-	2167	-	-	-
R875411	39.02106	-119.348	1701.444	Alu ± Ms ± Tpz	2189-2195	-	2167-2172	-	-	-
R875413	39.02247	-119.344	1655.306	Ms	2195-2200	-	-	-	-	-
R875417	39.02481	-119.346	1708.786	Ms	2195-2200	-	-	-	-	-
R875420	39.02522	-119.348	1720.453	Ms ± Dickite	2206	-	-	-	-	-
R875424	39.02484	-119.357	1882.063	Pyro ± Kaolinite	-	2167	-	-	-	-
R875426	39.02401	-119.358	1876.237	Pyro ± Dickite ± Tpz	-	2167	-	-	-	-
R875431	39.02529	-119.356	1868.678	Pyro ± Tpz	-	2167	-	-	-	-
R875434	39.02526	-119.356	1875.278	Ms ± Alu ± Tpz	2189-2195	-	2172	-	-	-
R875436	39.02494	-119.357	1878.902	Pyro ± Alu ± Ms	2195	2167	2167	-	YES	YES
R875445	39.02393	-119.358	1865.772	Pyro ± Ms	2195	2167	-	-	YES	YES
R875451	39.02344	-119.355	1804.426	Alu ± Pyro ± Ms ± Zun	2189-2195	2167	2167	2133	YES	YES
R875452	39.02365	-119.355	1814.187	Pyro ± Tpz	-	2167	-	-	-	-
R875463	39.02253	-119.352	1771.937	Ms ± Tpz	2195	-	-	-	-	-
R875477	39.0253	-119.352	1782.265	Pyro ± Alu	-	2167	2167	-	-	-
R875478	39.02475	-119.352	1758.594	Pyro ± Ms ± Dickite	2195	2167	-	-	YES	YES
R875483	39.02515	-119.351	1777.203	Pyro - Zun	-	2167	-	2133	-	-
R875491	39.02455	-119.351	1744.592	Ms	2183 - 2195	-	-	-	-	-
R875493	39.02488	-119.349	1724.04	Ms	2206	-	-	-	-	-
R875495	39.02504	-119.35	1733.242	Ms	2206	-	-	-	-	-
R875498	39.02587	-119.354	1828.391	Alu	-	-	2167	-	-	-
R875524	39.02299	-119.352	1759.589	Ms ± Pyro	2195	-	2167	-	YES	YES
R875539	39.02178	-119.354	1805.818	Ms	2200-2206	-	-	-	-	-
R875542	39.02175	-119.353	1780.901	Pyro ± Dickite	-	2167	-	-	-	-
R875544	39.02174	-119.359	1835.107	Ms	2195	-	-	-	-	-
R875560	39.02041	-119.355	1779.286	Ms ± Tpz	2195	-	-	-	-	-
R875577	39.01934	-119.343	1661.323	Kaolinite	-	-	-	-	-	-
R875579	39.01942	-119.349	1716.888	Ms	2189 - 2195	-	-	-	-	-

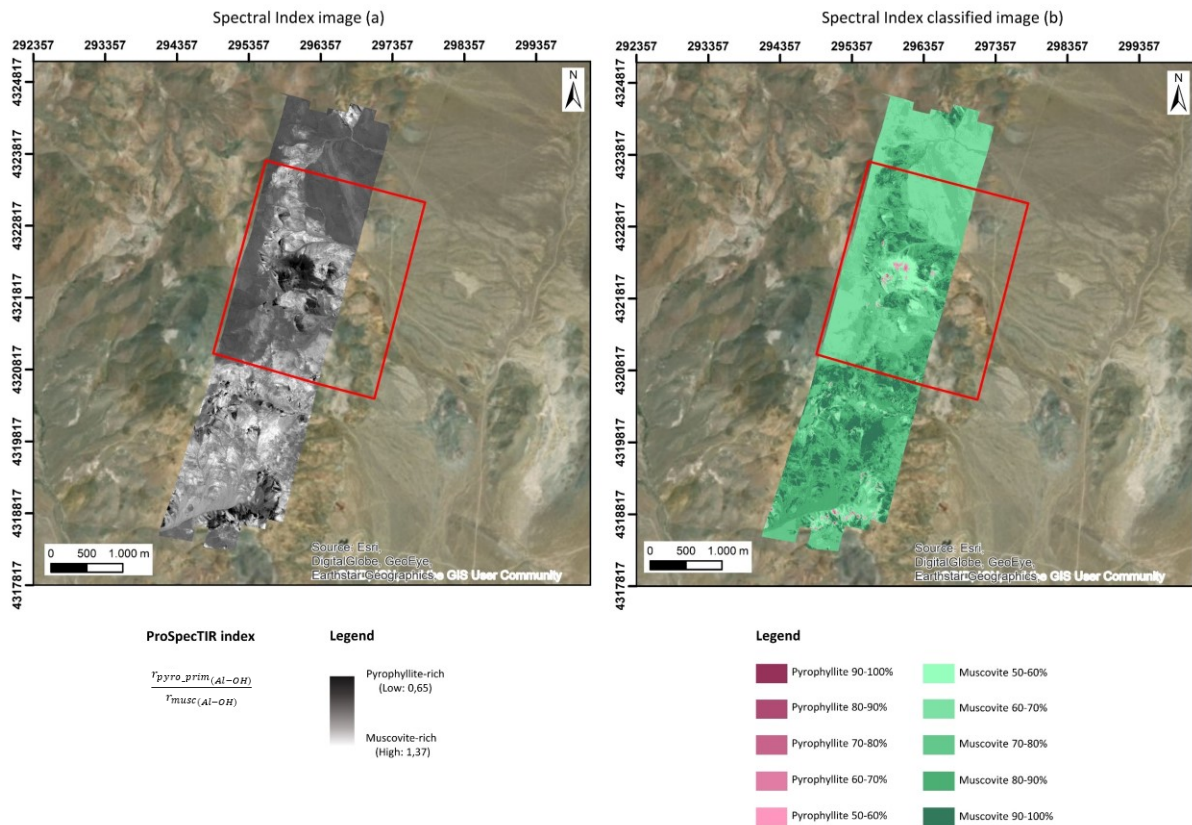
APPENDIX VI: Samples with pyrophyllite and muscovite co-occurrence.



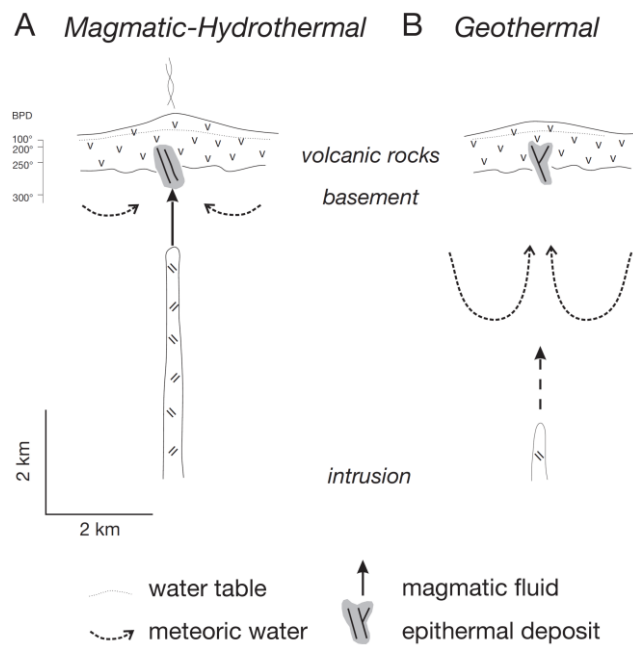
APPENDIX VI: Samples with pyrophyllite and muscovite co-occurrence.



APPENDIX VII: Full extension of the spectral index and classified image of the ProSpecTIR data. Study area delimited by the red polygon. (Base map from Esri (2019)).

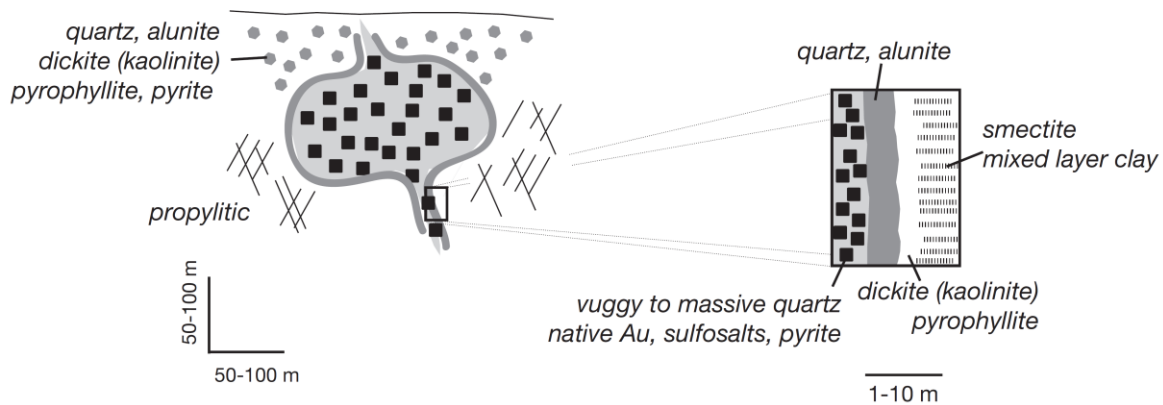


APPENDIX VIII: A simplified model of high-temperature hydrothermal systems presenting the relationship of epithermal environments. Compared to epithermal environments formed in geothermal systems (B), epithermal environments formed in the magmatic-hydrothermal system (A) presents minimum water-rock interaction because of the relatively short path that magmatic fluids follow from the intrusion to the epithermal environment. Hydrothermal fluids and water-rock interaction are key factors for the generation of epithermal deposits. Both factors control the pH, oxidation and sulfidation of the hydrothermal fluids (Simmons et al., 2005).



APPENDIX IX: Outward zonation alteration pattern resultant of an acidic fluid neutralised by hydrolytic alteration of aluminosilicates minerals (Simmons et al., 2005). The image on the left represented mineralogic zonation around epithermal orebodies. The internal zone composed of vuggy to massive quartz + native Au + sulfosalts + pyrite with a halo of advanced argillic alteration (quartz, alunite, dickite, pyrophyllite) of the shallow parts of this system and propylitic alteration on the deeper parts of this system. The image on the right presented in greater detail how the alteration zonation pattern occurred nearby the orebody.

### Quartz + Alunite ± Pyrophyllite ± Dickite ± Kaolinite



APPENDIX X: Comparison of the patterns observed in the classified image of the airborne spectral index and the alteration assemblages map developed by Fagbohun (2015).

